The Dissertation Committee for Robert Alan May Certifies that this is the approved version of the following dissertation:

Ellipsometric and Nanogravimetric Porosimetry Studies of Nanostructured, Mesoporous Electrodes

Committee:

Keith J. Stevenson, Supervisor

Richard M. Crooks

Paul F. Barbara

Chih-Kang "Ken" Shih

Keith P. Johnston

Ellipsometric and Nanogravimetric Porosimetry Studies of Nanostructured, Mesoporous Electrodes

by

Robert Alan May, B.A.

Dissertation

Presented to the Faculty of the Graduate School of
The University of Texas at Austin
in Partial Fulfillment
of the Requirements
for the Degree of

Doctor of Philosophy

The University of Texas at Austin
December, 2009

Dedication

To my parents, grandmother, Anna, and Lilia

Acknowledgements

I am blessed to have been surrounded by wonderful, supportive people my entire life. My parents have always gone out of their way to give me the tools necessary to succeed and have been directly involved in all of my endeavors. This involvement has allowed me to focus directly on success without having to worry about the 'little things' that can be so distracting. Lessons of hard work and tenacity have and will continue to serve me well, any success I have is directly tied to them. I am also indebted to my grandmother who, from the beginning, made me feel like I could be great at anything. Anna deserves special mention for putting up with an often over bearing older brother and for her visits to Austin that I always look forward to. I am very proud of her and her accomplishments during this time period as well. I can not have an acknowledgments section without thanking Lilia for all of the joy she has brought me these past few years. Lilia has been an inspiration to me, overcoming so many obstacles while remaining positive and doing truly exciting research. Outside of my family I also want to thank my high school football coach Mark Waggoner for teaching me important lessons of perseverance and determination as well as teaching me how to lead. My undergraduate research advisor Dr. Bert Chandler has been a good friend and is directly responsible for introducing me to the world of chemistry research and sending me down this career path which I have found extremely rewarding.

My graduate school experience has been incredible; I have grown as both a person and a scientist. This would not have been possible without the environment set up by my advisor Dr. Keith Stevenson. He has given me the freedom and resources to explore new ideas and the advice to make them work. The other members of the lab have been a joy to work with as well and I want to thank them for their discussions and contributions. My research has also been aided by our collaborations with outside groups. Specifically I would like to thank Dr. Mehul Patel and Dr. Keith Johnston for providing me with the wonderful mesoporous TiO_2 samples that formed the basis for our development of ellipsometric porosimetry. Building on this work we have also collaborated with David Flaherty and Dr. Buddie Mullins who have provided us with the RBD materials on QCM crystals reported on in chapter 4. Working with them has been a joy and our insightful discussions have helped to improve both our science and my own thoughtfulness as a researcher. I am also thankful for my good friends Craig Cone and Dan Sheppard both their friendship and helpful discussions. Additionally, I want to thank the entire UT Grad Rugby team for all the good times and friendships.

Ellipsometric and Nanogravimetric Porosimetry Studies of Nanostructured, Mesoporous Electrodes

Publication No._____________

Robert Alan May, Ph.D.
The University of Texas at Austin, 2009

Supervisor: Keith J. Stevenson

Nanostructured, porous materials offer great promise for application in areas such as energy storage, photovoltaics, and catalysis. These materials are often difficult to characterize because they are structurally and compositionally inhomogeneous, and disordered with features to small to be resolved by scanning probe techniques such as atomic force microscopy (AFM) and scanning electron microscopy (SEM). These shortcomings require that new techniques be developed that can be applied to real world systems to elucidate how the interplay of material composition and structure alters their performance. Towards this end, the development of a hybrid quartz crystal microbalance/ ellipsometric porosimetry (QCM/EP) technique is being pursued to facilitate the determination of a number of material

parameters such as porosity, pore size distribution, and surface area. Additionally, the use of adsorbate probe molecules of varying polarity gives further information about adsorbate-surface interactions and surface chemistry characteristics. Simultaneous acquisition of both mass-based and refractive index based adsorption isotherms fosters mechanistic understanding about the behavior of adsorbates confined in mesopores while at the same time reducing the uncertainty in the analysis of the optical parameters acquired via ellipsometry.

To highlight the power of this approach, studies of TiO_2 and TiC, electrode materials as model systems will be presented that have helped us validate measurement and modeling protocols for extracting physical properties.

TABLE OF CONTENTS

CHAPTER 5 **171**

LIST OF TABLES

LIST OF FIGURES

CHAPTER 1

Enhanced Understanding of Complex Materials Via the Development of Hybrid Analytical Techniques

1.1 MOTIVATION

Templating nanostructure into materials has been shown to improve performance for applications such as energy storage[1], photovoltaics[2], and catalysis[3]. The enhanced properties of these materials arise from interplay between composition and structure. In order to facilitate understanding of this complex parameter space we are developing hybrid characterization techniques such as quartz crystal microbalance/ ellipsometric porosimetry (QCM/EP). This technique has the sensitivity to measure isotherms on thin films, allowing for the determination of material parameters such as porosity, pore size distribution, and surface area. Additionally, simultaneous acquisition of both mass-based and refractive index based adsorption isotherms fosters mechanistic understanding about the behavior of adsorbates confined in mesopores, while at the same time reducing the uncertainty in the analysis of the optical parameters acquired via ellipsometry.

Ellipsometry was developed by Drude in 1887[4], the use of the quartz crystal for gravimetry was pioneered by Sauerbrey[5] in 1959. Adsorption phenomenon have a long history of intense study, Brunauer, Emmet, and Teller worked out their now famous isotherm model in 1938.[6] Ellipsometry was applied to determining adsorption isotherms as early as 1964[7]. All this is to say that individually or in combination the techniques discussed hereafter are not new, yet there is much to be gained from further study. The revolution brought about by our ability to understand and control features at the nanoscale makes understanding and expanding the synergies of these techniques vital. This need arises from both fundamental and practical considerations. Despite over 100 years of research the behavior of adsorbates on a surface or confined in a pore is ill understood. Even with more accurate theoretical treatments enabled by density functional theory (DFT) well ordered experimental systems sensitive on the desired scale are lacking. This deficit creates a host of problems for the accurate extraction of information from isotherms, limiting their usefulness as analytical techniques. This shortcoming is unfortunate because porosimetry is ideal for characterizing subtle nanoscale features across the centimeter and larger length scales required of working devices. For example many cathode materials for Li-Ion batteries are enhanced by templating nanostructures.[8] These are often characterized by scanning electron microscopy (SEM) or atomic force microscopy (AFM) with maximum spot sizes on the order of microns. The strengths and weaknesses of several popular analytical techniques for characterizing porous materials are summarized in Table 1.1 (adapted from Sanchez et al.[9]). This table makes it clear that new techniques, such as EP, are needed to probe across real device lengths while maintaining the sensitivity to analyze the new properties that arise from nanomaterials.

Table 1.1 Summary of Porous Material Characterization Techniques

	Thin Film Compatible	Thickness	Pore Volume	PSD	Surface Area	Multilayer Resolution
BET (N_2)	✗	✗	✓	✓	✓	✗
AFM	✓	-	✗	-	✗	✗
TEM	✓	✓	✗	-	✗	✓
SEM	✓	-	✗	-	✗	✓
EP	✓	✓	✓	✓	✓	✓

The aim of this work is to combine complimentary analytical techniques into something greater than the sum of its parts, increasing the density of information gained from a single experiment. The power, and necessity, of increasing the information density is embodied in spectroscopic ellipsometry. In this technique the change in the shape of elliptically polarized light following interaction with a sample is measured to determine two independent parameters Ψ and Δ, typically across a range of wavelengths. The number of measured parameters is increased from one (i.e traditional intensity measurements) to two so that a single experiment determines the film thickness as well as both the real, n, and imaginary, k, components of the complex refractive index. This clearly shows the power of increasing the information density. The paradox of ellipsometry is that while it increases the information gleaned from an experiment it also benefits greatly from the addition of even more information. Only in specific cases can Ψ and Δ be converted directly into the optical constants, typically extracting these parameters relies on the application of an optical model with parameters determined by an iterative fitting procedure. The reason that model fitting is necessary is that there are more unknowns than measured values. Therefore, the accuracy of ellipsometry results is enhanced through the addition of complimentary data. For example in chapter 2 the optical constants of different metal oxides are determined by fitting optical models to the ellipsometry parameters Ψ and Δ in addition to transmission measurements. The addition of intensity data was integral to obtaining unique solutions for *n*, *k*, and thickness. The next step in increasing information density is taken in Chapter 3 with the development of ellipsometric porosimetry (EP). In EP adsorption isotherms are generated by combining ellipsometry measurements with variations in the ambient environment. In Chapter 4 EP is then hybridized with a quartz crystal microbalance (QCM) which allows us to compare changes in the optical properties of a porous sample relative to the mass uptake as measured by QCM. Then the ellipsometry technique is further augmented through measurements of additional polarization states to determine values of the 4 x 4 Mueller matrix. This data is then used to determine the three distinct principal refractive indices of biaxial mesoporous TiO_2 and how each responds to the adsorption of toluene.

1.2 OVERVIEW OF HYBRID TECHNIQUES FOR STUDYING POROUS ELECTRODES

The combination of QCM and EP into QCM/EP highlights the usefulness of hybrid methodologies because the combined technique provides information not available separately. Porous electrodes often undergo many changes in their optical constants due to changes in redox state, mechanical breakdown due to stress, and changes in density. These changes provide a window into the processes affecting the material but they can also interfere with aspects of either measurement. For example changes in stress can lead to a frequency shift in the QCM while light absorption throughout the spectral range (arising from changes in the redox state) can make determining the volume adsorbed difficult. However, comparison of QCM and EP results allows us to correct for these situations. There are other examples of complimentary techniques which, when applied to porous electrodes have greatly enhanced our understanding of the behavior of these complex systems.

Scanning probe techniques such as atomic force microscopy (AFM) provide unprecedented resolution of sample surfaces, enabling the study of micro/nano crystalline electrodes. Materials at this size scale often contain a mixture of domains whose ratio can be tailored for maximum performance, provided those domains can be characterized. For example Stevenson and McEvoy[10] combined conductive probe atomic force microscopy (CP-AFM) with Raman spectroscopy to isolate two distinct domains composing thin film MoO_3. CP-AFM simultaneously determines the topography and electrical conductivity of a sample. Approximately, ¾ of the sample displayed insulating behavior while the other ¼ was very conductive. The insulating regions were correlated with microcrystalline regions, α-MoO_3, while the conductive regions were associated with nanocrystalline domains, β-MoO_3, both domains are clearly resolved in the topography component. These same regions were then probed with Raman spectroscopy, 1μm spot size, to confirm the structure of the identified regions. Each of the regions displayed a unique Raman signature with the non conductive region being consistent with layered orthorhombic α-MoO_3 while the conductive region was consistent with monoclinic β-MoO_3. The layered structure of α-MoO_3 results in much better ionic conductivity compared to β-MoO_3 so that, for a battery application, the superior electronic conductivity of β-MoO_3 must be balanced against the better ionic conductivity of α-MoO_3. This difference in ionic conductivity was quantified in the same study using high resolution spectroelectrochemical imaging which combines cyclic voltammetry with microscope imaging to quantify color changes occurring in MoO_3 during Li^+ intercalation.

Optical interrogation of electrochemically modulated electrodes is an effective means of understanding the systems because the color changes are related to changes in the redox state which is directly tied to the Li^+ ion behavior. Imaging through a 40x microscope objective combined with a red (630 ± 30 nm) bandpass filter McEvoy and Stevenson[11] quantified Li^+ intercalation in mixed phase MoO_3, simultaneously determining the ionic conductivity of α-MoO_3 and β-MoO_3. This technique was then extended to utilize the superior sensitivity of diffraction.[12] In this experiment WO_3 or $Mo_{0.6}W_{0.4}O_3$, were cast into parallel rows which produced a one dimensional diffraction grating. Individual spots on the grating could be located on the microscope and diffraction from the localized area imaged using a Bertrand lens to focus the diffraction pattern on a CCD. The change in the diffraction efficiencies (DE) of WO_3 and $Mo_{0.6}W_{0.4}O_3$, gratings were measured during electrochemical modulation of Li^+ intercalation using both cyclic voltammetry and chronoamperometry. DE is sensitive to changes in both the real, n, and imaginary, k, components of the refractive index meaning that the sensitivity to Li^+ intercalation is a function of two parameters that may oppose one another. The contribution of *n* and *k* to DE was evaluated based on *in situ* spectroscopic ellipsometry (SE) measurements of WO_3 and $Mo_{0.6}W_{0.4}O_3$ thin films undergoing similar electrochemical modulation. Overall DE was determined to be much more sensitive to changes in *n*; however, the *k* component became significant at longer wavelengths, attenuating the sensitivity.

Quartz crystal microbalance/heat conduction calorimetry (QCM/HCC) simultaneously measures the mass of an adsorbate and the heat of adsorption.[13-16] Smith et al. have used this technique to study a variety of systems with applications as wide as catalysis[16] and polymer drying[14]. The basic premise is that a QCM, used to determine the mass adsorbed, is placed in thermal contact with a thermopile. As heat flows from the thermopile to a large heatsink placed on the other side a voltage is induced which can then be read to quantify the heat flow. This instrument, now sold by Masscal Scientific Instruments, is capable of measuring mass changes on the order of ± 2ng and changes in heat flow of ± 0.5 μW.

1.3 SUMMARY OF CHAPTERS

Chapter 2 is focused on the analysis of metal oxide thin films, primarily mixed molybdenum−tungsten oxides of varying stoichiometry ($Mo_xW_{1-x}O_3$, $0 < x < 1$) prepared by cathodic electrodeposition from aqueous peroxo-polymolybdotungstate solutions on indium tin oxide (ITO) coated glass substrates. WO_3 films of varying grain size, controlled by pulsed deposition, and surfactant templated TiO_2 were also analyzed to determine the effects of composition and grain size on optical properties. All samples were modeled primarily with a Tauc−Lorentz dispersion model to extract the real and imaginary components of the complex refractive index. The optical band gaps were also estimated from Tauc plots. For $Mo_xW_{1-x}O_3$ the refractive index increased (2.07−2.20 at 800 nm) while the optical band gap decreased (3.38−2.95 eV) in a linear fashion with increasing Mo fraction. These trends correlate chiefly with Mo-doping-induced changes in film structure and grain size as supported by X-ray diffraction measurements and similar dependence of the optical band gap on grain size is found for WO_3 and TiO_2.

Au and Pt nanoparticle distributions within hierarchically ordered mesoporous TiO_2 are explored in chapter 3 using a combination of techniques including ellipsometric porosimetry (EP) and X-ray photoelectron spectroscopy (XPS). EP studies were used to examine adsorbate−TiO_2 interactions and the influence of adsorbate polarity upon adsorption isotherms for mesoporous TiO_2 films with and without Pt and Au nanoparticles. In particular, methods are described for modeling EP data to estimate the surface area and porosity of mesoporous TiO_2 films and for estimating the pore size distribution (PSD) directly from the ellipsometry parameters Ψ and Δ when fitting parameters alone are unable to extract reliable optical constants from the ellipsometry data. This approach reveals that mesoporous TiO_2 films of ~ 200 nm thickness and ~10 nm pore diameter can be loaded with 1.7 nm diameter Pt and 3.9 nm diameter Au nanoparticles up to 26 and 21 wt %, respectively. The BET surface area of a representative mesoporous TiO_2

sample using toluene as the adsorbate was found to be 44 m^2/g with a mean pore diameter of 8.8 nm. EP and XPS depth profiling experiments indicate that 1.7 nm diameter Pt nanoparticles are well dispersed through the mesoporous TiO_2, while 3.9 nm diameter Au nanoparticles are concentrated at the top of the film, blocking a significant portion of the available pore volume. UV irradiation of the films indicates that adsorbate−TiO_2 interactions and surface wetting effects can play a critical role in the resulting isotherm and in evaluation of PSD.

The ellipsometric porosimetry technique is further developed in Chapter 4 by integration with a quartz crystal microbalance. This system is first used to study high surface area, porous titanium carbide films synthesized at room temperature via reactive ballistic deposition (RBD). Angle-dependent RBD allows for the controlled tuning of TiC nanostructure and porosity where changing the deposition angle from near normal incidence (13°) to more glancing angles (50 – 85°) changes the film morphology from relatively non-porous, dense TiC to a continuous, reticulated TiC and finally to discrete, mesoporous, nanocolumnar TiC. The influence of the deposition angle on TiC optical constants, porosity, specific surface area and the pore size distribution is determined with quartz crystal microbalance/ellipsometric porosimetry (QCM/EP). The anisotropic properties of similarly deposited TiO_2 are then explored using generalized ellipsometry. This type of ellipsometry measures additional polarization states allowing us to determine the values of the three principle refractive indices. The refractive index of the fast axis is found to increase rapidly in response to toluene adsorption leading to a decrease in anisotropy.

Chapter 5 takes a look at the future of QCM/EP both in terms of improving the apparatus and developing new mesoporous materials for study. The design of a new porosimetry cell is discussed to improve the accuracy and precision of QCM/EP. This cell also integrates a rotating stage which will allow us to determine the full azimuthal orientation dependence of biaxial samples. The added potential of integration with calorimetry is discussed as well as the incorporation of electrochemistry. RBD deposited vanadium oxide is proposed as the next material to be studied along with the possibility of creating mesoporous noble metal films using electrochemical dealloying. Finally, the need for highly ordered arrays of mesopores with adjustable size is discussed for the purposes of confirming ellipsometry models and effective medium approximations. Some work has been done in this area by annodization of Ti and Al thin films; those preliminary results are described.

1.4 REFERENCES

(1) Wang, Y.; Takahashi, K.; Lee, K.; Cao, G. *Advanced Functional Materials* **2006**, *16*, 1133-1144.

(2) Thimsen, E.; Rastgar, N.; Biswas, P. *Journal of Physical Chemistry C* **2008**, *112*, 4134-4140.

(3) Thomas, J. M.; Hernandez-Garrido, J. C.; Raja, R.; Bell, R. G. *Physical Chemistry Chemical Physics* **2009**, *11*, 2799-2825.

(4) Schubert, M. *Annalen der Physik (Weinheim, Germany)* **2006**, *15*, 480-497.

(5) Sauerbrey, G. *Zeitschrift fuer Physik* **1959**, *155*, 206-22.

(6) Brunauer, S.; Emmett, P. H.; Teller, E. *Journal of the American Chemical Society* **1938**, *60*, 309-19.

(7) Claussen, B. H. *Journal of the Electrochemical Society* **1964**, *111*, 646-52.

(8) Bazito, F. F. C.; Torresi, R. M. *Journal of the Brazilian Chemical Society* **2006**, *17*, 627-642.

(9) Sanchez, C.; Boissiere, C.; Grosso, D.; Laberty, C.; Nicole, L. *Chemistry of Materials* **2008**, *20*, 682-737.

(10) McEvoy, T. M.; Stevenson, K. J. *Langmuir* **2005**, *21*, 3521-3528.

(11) McEvoy, T. M.; Stevenson, K. J. *Langmuir* **2005**, *21*, 3529-3538.

(12) Kondrachova, L. V.; May, R. A.; Cone, C. W.; Vanden Bout, D. A.; Stevenson, K. J. *Langmuir* **2009**, *25*, 2508-2518.

(13) Smith, A. L. *Polymer Preprints (American Chemical Society, Division of Polymer Chemistry)* **2004**, *45*, 199-200.

(14) Smith, A. L.; Mulligan, R. B.; Shirazi, H. M. *Journal of Polymer Science, Part B: Polymer Physics* **2004**, *42*, 3893-3906.

(15) Smith, A. L.; Shirazi, H. M. *Thermochimica Acta* **2005**, *432*, 202-211.

(16) Smith, A. L.; Shirazi, H. M.; Smith, F. C. *Catalysis Letters* **2005**, *104*, 199-204.

CHAPTER 2

Spectroscopic Ellipsometry of Metal Oxides*

2.1 INTRODUCTION

Redox-active transition metal oxides such as MoO_3 and WO_3, and TiO_2 have received significant attention due to their broad application as rechargeable batteries[1], non-emissive displays[2], photovoltaics[3], and gas sensors.[4] These materials are promising since their electronic and optical properties can be reversibly modulated via oxidation and reduction reactions triggered by an applied potential, light, or by the presence of a chemical species. Moving past unary based transition metal oxides, binary metal oxides are emerging as exciting alternatives due to the added prospect of uniquely tailoring structural, optical, and electronic properties to improve the materials performance when utilized in the aforementioned applications. For example, Monk and coworkers[5,6] have shown that the electrochromic properties of MoO_3 can be adjusted by incorporating Co, Cr, Fe, Ni, and Zn. Correlations between optical absorption bands and proton transport were established suggesting that both optical and ion transport properties could be tuned by doping the metal oxide host with a secondary metal oxide. Mixed molybdenum-tungsten oxide films of varying stoichiometry ($Mo_xW_{1-x}O_3$, $0 < x < 1$) can be prepared by electrodeposition and demonstrate improvement in

---

[*] Portions of this chapter were published in May, R. A.; Kondrachova, L.; Hahn, B. P.; Stevenson, K. J., *Journal of Physical Chemistry C* **2007,** 111, (49), 18251-18257.

structural stability during electrochemical cycling along with enhancement of electrochromic and lithium ion insertion properties relative to single component WO_3 and MoO_3.[7]

While the optical properties of $Mo_xW_{1-x}O_3$ materials prepared by thermal evaporation[8], sputtering[9], sol-gel[10], and chemical vapor deposition[11] have been described previously, the majority of investigations have prepared materials that vary over a limited compositional range. As such, the compositional dependence of the optical properties and the type of electronic transitions involved has not been clearly reported for materials ranging over the full compositional phase space. This makes it difficult to discern trends in structure-property relationships of binary metal oxides.

We have investigated the effect of Mo content on the optical properties of electrodeposited molybdenum-tungsten oxide films ($Mo_xW_{1-x}O_3$, $0 < x < 1$) prepared from aqueous peroxo-polymolybdotungstate solutions. Combined spectroscopic ellipsometry and transmission measurements have been interpreted with a Tauc-Lorentz dispersion model to estimate optical constants. This model combines the Tauc band edge with a Lorentz broadening function to yield good agreement between the measured ellipsometry and transmission data. Analysis of the data reveals that the real component of the refractive index increases and optical band gap decreases linearly with increasing Mo fraction. These trends are shown to strongly correlate with changes in structure and grain size induced by variation of Mo content. The dependence of the optical band gap on grain size is also verified in two distinct unary systems. The first uses pulsed deposition to vary the grain size of WO_3 while the second varies the porosity (and thus the grain size) of sol gel derived TiO_2 using a surfactant template.

2.2 EXPERIMENTAL

2.2.1 Deposition of $Mo_xW_{1-x}O_3$

$Mo_xW_{1-x}O_3$ films were deposited from 60 mM peroxo-polymolybdotungstate solutions onto conductive ITO-coated glass substrates (Delta Technologies, Ltd., 15Ω/□).[7] Potentiostatic depositions were performed without stirring at a fixed potential of -0.35V vs. Ag/AgCl to a total charge density of ~0.13 C/cm^2. The films were desiccated and heated in air at a rate of 60 ^{o}C/h to a final temperature of 250 ^{o}C and held for 2 h. The resulting films are compositionally homogenous[7] and stable over several days when stored in a desiccator.

2.2.2 Pulsed Deposition of WO_3

WO_3 films of varying grain size were deposited from 50 mM peroxo-polytungstate solution onto ITO using a pulsed electrodeposition technique[12]. All depositions were carried out for a total time of 20 minutes by applying a square waveform going from open circuit potential to -1V vs. Ag/AgCl. Pulse widths of 5ms, 50ms, 100ms, and 300ms were used to vary the grain size of the films. The film surface was imaged using a Veeco Instruments Bioscope Nanoscope IV atomic force microscope (AFM) in tapping mode. The resulting AFM images were analyzed using ImageJ[13] analysis software to estimate the grain size of the films.

2.2.3 Preparation of Mesoporous TiO_2

ITO/glass slides (Resistance: 15-25 ohm, ITO layer thickness: 60–100 nm) were purchased from Delta Technologies were coated with a TiO_2 buffer layer from a solution prepared from 0.03 g of $Ti(O\square i\text{-}C_3H_7)_4$ and 10 cm^3 of 2-propanol via dip-coating with a withdrawal speed of approximately 6.0 cm/min, followed by heat treatment at 200 ^{o}C for 5 min in air. Mesoporous titania films were prepared on these samples by self-assembly of the P123 block copolymer surfactant in sol-gel solution.[14,15] 1.05 g of $Ti(O\cdot i\text{-}C_3H_7)_4$ was hydrolyzed using 0.74 g of HCl under stirring for 10 min at room temperature. The hydrolyzed sol was mixed with 0.2 g of P123 surfactant dissolved in 3.0 g of ethanol under stirring for 15 min at room temperature. The resulting solution was spin-coated on the substrates at a rate of 8000 rpm for 1 min, followed by aging for 2 days at either –5 ^{o}C or 25 ^{o}C under a controlled humidity of 45–55%. The samples were finally calcined using a tube furnace at 400 ^{o}C for 4 h in air with a heating rate of 1.0 ^{o}C/min to remove the block copolymer template and enhance the inorganic framework between Ti and O atoms.

2.2.4 Characterization Techniques

The atomic concentration of Mo and W was determined using energy dispersive spectroscopy (EDS) at the Lα lines of Mo (2.293 keV) and W

(8.396 keV) with a Leo 1530 scanning electron microscope (SEM) operating at 20 keV. X-ray diffraction (XRD) analysis was performed using a Bruker-Nonius D8 Advance Theta-2Theta powder diffractometer with a Cu Kα line source λ=1.5406Å. Data was acquired between 20° and 50° at a rate of 10°/min. Data acquisition was performed every 0.1°, and each sample was scan averaged for ~8 h.

Spectroscopic ellipsometry (SE) was used to determine the thickness and optical properties of $Mo_xW_{1-x}O_3$ films as well as WO_3 films prepared by pulsed deposition, and sol gel templated TiO_2. The technique does not directly measure optical constants, instead it measures two parameters, Ψ and Δ, representing the relative change in magnitude and phase between two perpendicular light waves. This is described by the equation $\rho = r_p / r_s = \tan(\Psi) e^{i(\Delta)}$ [16], where r_p and r_s are, respectively, the Fresnel reflection coefficients for p and s polarized light. These values can be transformed into the wavelength dependent real (n) and imaginary (k) refractive indices using optical models. For systems that absorb light (k>0), the addition of transmission measurements (%T) aids in the determination of a unique model.[16] SE and transmission measurements were taken from 200-1000 nm at angles of 60°, 65°, and 70° using a J.A. Woolam M-2000 variable angle spectroscopic ellipsometer (VASE). Matte finish Scotch tape was applied to the back of the transparent substrates to minimize backside reflectance. Using the Levenburg-Marquardt algorithm model parameters were minimized to a mean square error (MSE) of less than 10. Resulting thicknesses were verified by AFM and typically agreed within a few percent. The ITO substrate was modeled utilizing a substrate layer of Corning 1737 glass and a two part graded layer to model the thickness dependent optical constants of ITO. ITO is difficult to model and must be described by multiple layers containing several oscillators that can vary widely with thermal history and thickness. Others have modeled ITO on glass using a graded model with multiple Lorentzian oscillators[17], however, the long tails of the Lorentzian approximations overestimated the absorbance. To address this problem, a modified version of the Lorentzian oscillator known as the Tauc-Lorentz oscillator (T-L)[18] was employed. The model is presented here as defined by equations 1 and 2 given below in terms of the real and imaginary dielectric function. These are directly related to n and k by $\varepsilon_2=2nk$ and $\varepsilon_1=n^2-k^2$. For this analysis the T-L oscillator has two distinct advantages: it forces k (absorbance) to zero below the band gap and better describes k above the band gap by utilizing the band edge description developed by Tauc.[19] Jellison and Modine[18] derived this model by first describing the imaginary dielectric function multiplying the equation for a single Lorentzian transition by the Tauc description of the band gap, eq. 1. This necessitated four fit parameters: the peak transition energy E_0, the amplitude A, a broadening term C, and the band gap, E_g.

$$\varepsilon_{2TL}(E) = 2nk = \left[\frac{AE_0C(E-E_g)^2}{(E^2-E_0^2)^2+C^2E^2}\cdot\frac{1}{E}\right], E > E_g \qquad (1)$$

$$\varepsilon_{2TL}(E) = 0, E < E_g$$

To then describe the real portion of the refractive index, eq. 1 is transformed into eq. 2 using the Kramers-Kronig (K-K) relationship which relates the real and imaginary components of the refractive index.

$$\varepsilon_1(E) = n^2 - k^2 = \varepsilon_1(\infty) + \frac{2}{\pi} P \int_{E_g}^{\infty} \frac{\xi \varepsilon_2(\xi)}{\xi^2 - E^2} d\xi \qquad (2)$$

As a consequence of the K-K transformation a fifth fit parameter $\varepsilon_1(\infty)$ is added to account for effects of adsorbance at higher frequencies. Note also that P in eq. 2 stands for the Cauchy principal value. In addition to the T-L oscillator, a Gaussian oscillator was included to account for experimentally observed absorbance just below the band gap. This oscillator has three fit parameters; the peak transition energy E_0, the amplitude A, and a broadening term C. The Gaussian oscillator was chosen over the Lorentzian oscillator because it has narrower tails; thus, minimizing the problem of the oscillator tails overestimating absorbance. Free carrier absorption at low energies was described using the Drude model, which is effectively a Lorentzian oscillator centered at 0 eV which consists of only amplitude and broadening fit parameters.[16] After determining the optical constants of ITO, the $Mo_xW_{1-x}O_3$ layer was constructed on top of the ITO layer with a Tauc-Lorentz oscillator to describe the band edge and a Gaussian oscillator to account for band tailing. Anisotropy was not observed, though it has been reported in MoO_3 films.[20,21] Anisotropy was not expected here due to the lack of extended long range order[7] and the breaking of the optical symmetry by the ITO layer.[22]

2.3 RESULTS AND DISCUSSION

2.3.1 X-ray diffraction of $Mo_xW_{1-x}O_3$

Electrodeposited $Mo_xW_{1-x}O_3$ thin films supported on ITO and sintered in air at 250 ºC for a period of 2 hr are strongly adherent, continuous, and fairly smooth.[7] Previous work has indicated that sintering at 250 ºC is optimal for enhancing electrochromic and lithium ion insertion properties.[23] Therefore, in an effort to make comparisons between electrochemical and optical investigations, we examine electrodeposited $Mo_xW_{1-x}O_3$ as well as pure MoO_3 and WO_3 films supported on ITO prepared and sintered under similar conditions. Figure 2.1 shows X-ray diffraction (XRD) patterns for the evolution in structure of $Mo_xW_{1-x}O_3$ films as a function of Mo content. Structurally, the pure MoO_3 films consist of an orthorhombic α phase, while pure WO_3 consists of nanocrystalline domains in a triclinic/monoclinic arrangement.[7] No significant XRD peaks are observed above 30^o indicating that the films do not have extended long range order.[7] As the Mo fraction in $Mo_xW_{1-x}O_3$ increases, the symmetry of the crystal structure transforms from triclinic to monoclinic to orthorhombic.[7] Due to the limited number of peaks, absolute structure assignment is difficult because small changes in the diffraction pattern can lead to a wide variety of structural assignments.[24-29]

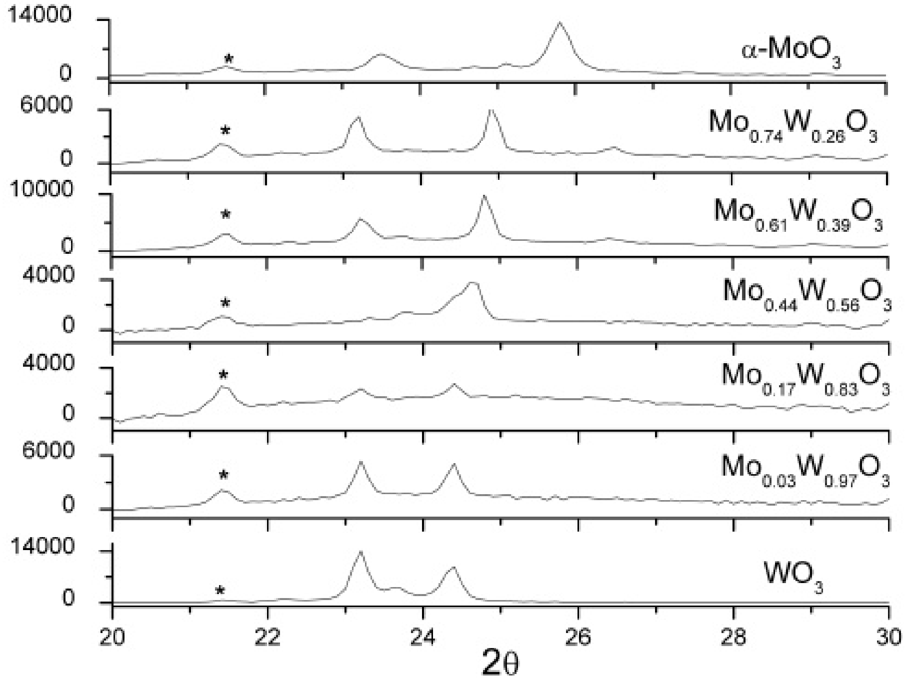

Figure 2.1. Representative X-ray diffraction patterns of WO_3, α-MoO_3, and $Mo_xW_{1-x}O_3$ films prepared by electrodeposition on ITO at –0.35 V followed by sintering at 250 °C. Diffraction patterns are identified in terms of the Mo fraction, *x*. * denotes ITO peaks.

Despite ambiguities in the assignment of crystal structures the evolution of films structure with composition is clearly seen in the XRD patterns (Figure 2.1). Three distinct structural regions are observed in this series of films. For $x < \sim 0.2$ the structure is similar to that of WO_3 while for $x > \sim 0.6$ a more orthorhombic structure is observed.[28] The slightly shifted peak present at 24.8° and the small peak seen at 26.5° distinguish the XRD spectrum for $x > \sim 0.6$ from that observed for $x < \sim 0.2$. Between these two regions the film at $x = 0.44$ appears to be a mixture of the two monoclinic/orthorhombic structural polymorphs.

Comparing the diffraction patterns of WO_3 to $Mo_{0.03}W_{0.97}O_3$ and $Mo_{0.17}W_{0.83}O_3$ the statement that these two mixed film compositions have the same structure as WO_3 appears tenuous as the peak at 23.6° is not observed. However, we normalized the diffraction peaks to the ITO peak at 30.5° and observed an order of magnitude decrease in intensity between WO3 and $Mo_{0.03}W_{0.97}O_3$. Thus the peak at 23.6° has likely been lost beneath the noise floor. The drop in intensity is described by eq. 3 which is formulated for diffraction from an ideally imperfect crystal.[30]

$$\frac{E\omega}{I_0} = \frac{N''^2 e^4 \lambda^3}{2m^2 c^4} * F^2 * \frac{1+\cos^2(2\theta)}{\sin(2\theta)} \qquad (3)$$

E is the integrated radiation to the counter, ω is the angular velocity, I_o is the incident intensity, N” is the number of atoms per unit volume, F is the structure factor, and all other variables are traditional parameters. The two primary variables affecting the diffracted intensity are N” and F. The fact that the real refractive index of $Mo_xW_{1-x}O_3$ does not deviate from linearity indicates that the densities of the mixed films remain nearly constant thus also indicating that N" does not change. Therefore, observed differences in XRD intensities can be attributed to changes in the structure factor, F. The structure factor accounts for the variation in how different atoms scatter X-rays at various positions in the crystal lattice and it is very reasonable that it would change with composition.[30]

In a review of mixed $Mo_xW_{1-x}O_3$ structures synthesized at low temperatures and prepared by a comparable *chimie douce* process[25] several isostructural composition regions are documented. The ranges noted are very similar to what we have observed even though the structural assignments are not the same, a fact we attribute to differences in initial composition and the influence of our ITO substrate. For Mo fractions, $x < 0.2$, Figlarz[25] assigned a hexagonal structure, while for $0.2 < x < 0.6$ an orthorhombic structure is assigned owing to distortions arising from increased Mo content.[25] For $0.6 < x < 1$ an ReO_3 like structure is given.[25] These results indicate that composition has a set effect on structure, even if the initial preparation conditions of the film influence phase transformations to different resultant structures after sintering.

The grain size of the $Mo_xW_{1-x}O_3$ films can be estimated based on the broadening of the XRD diffraction peaks according to the Scherrer equation,

$$t = \frac{0.9\lambda}{B\cos(\theta_B)} \tag{4}$$

where t is the grain size, λ is the incident wavelength, B is the angular width along the 2θ axis (in radians), and θ_B is the angle of the diffraction peak.[31] A large broad feature, arising chiefly from amorphous broadening, was found to interfere with the Scherrer analysis and so peak broadening was estimated from a multiple Gaussian fit, $R^2>0.98$ for all films, from 22°-32° on the 2θ axis. When using Scherrer analysis non-uniform film strain is a concern because it also induces peak broadening,[31] and our films were previously shown to be under strain.[7] Nevertheless, there is no evidence that film strain varies significantly with composition, so differences in peak broadening between the films can be attributed to differences in grain size. The grain size of the films is found to increase with Mo content (Table 2) similar to the trend observed by Taurino and coworkers[10] using TEM measurements. The observed changes in broadening between each successive composition are subtle (~0.01°) but the instrument's angular resolution far exceeds this. The underlying ITO layer provides an internal standard. The standard deviation of the grain size derived from the most intense ITO peak of all films tested is less than half a nanometer. This deviation is much less than the 1-4 nm change in grain size observed for each step in Mo content indicating that the trend in grain size measured by Scherrer analysis is real. Due to the length of time required to acquire a diffraction pattern and the number of samples involved XRD was not performed on multiple samples of the same composition so no standard deviation has been reported.

2.3.2 Ellipsometry Models

2.3.2.1 Model of Indium Tin Oxide

Prior to describing trends in VASE determined optical constants for $Mo_xW_{1-x}O_3$ and TiO_2 films, it is important to detail the modeling of the optical response of the ITO substrate. Representative Ψ, Δ, and %T experimental data and model fits determined at three angles for ITO are presented in Figure 2.2. The agreement between experiment and model at all angles is excellent, with fits to the transmission data deviating by no more than 2%. There is slight misfit at the sharp ellipsometric features; which is expected due to non-ideal conditions such as wavelength spreading, angular broadening, non-uniform film thickness, etc.[16] The optical constants of the two layers used to model the grading of the ITO are presented in Figure 2.2 d. The upper layer has a much larger Drude edge, seen as the large k value in the near IR, than the lower layer, consistent with other observations[17] of enhanced conductivity in the upper portion of ITO. Following annealing at 250^o C, it was found that the Drude edge was enhanced for ITO underneath the film relative to that outside of the film. The enhancement is consistent with that reported for ITO films sintered in a reducing atmosphere due to a higher carrier concentration arising from oxygen deficiencies.[32] Therefore, it is necessary to include the Drude edge as an added fit parameter when determining the optical constants of oxides which have been sintered.

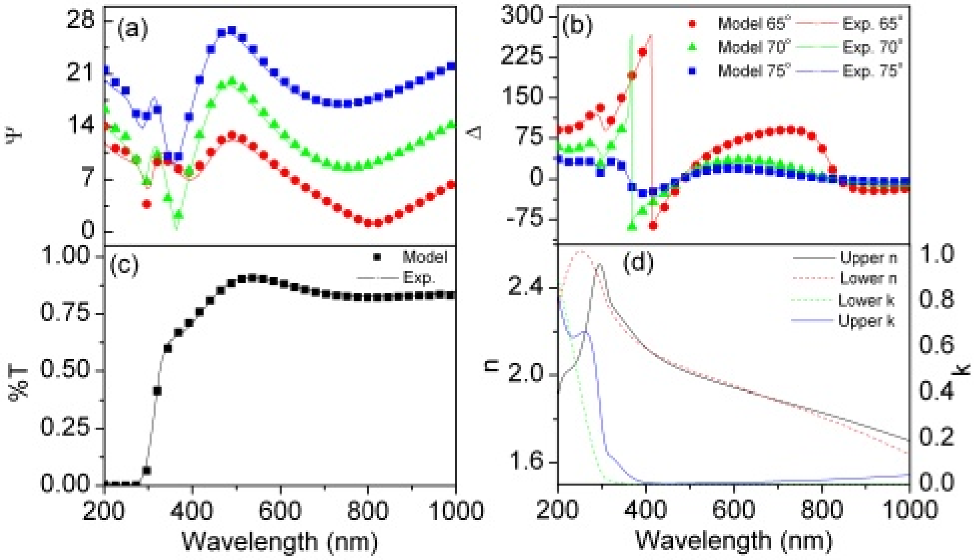

Figure 2.2 Plots of (a)Ψ, (b) Δ, and (c) %T versus wavelength for ITO heat treated at 250°C for 2h. Ψ and Δ are determined at 60°, 65°, and 70°. Lines represent the experimental data while symbols are the model fit. d) Estimated optical constants for real component, *n*, and imaginary component, *k*, of the refractive index for ITO using a graded two-layer model.

2.3.2.2 Model of $Mo_xW_{1-x}O_3$

Ψ, Δ, and %T spectra and model fits for representative $Mo_xW_{1-x}O_3$ film supported on ITO are presented in Figure 2.3. Fit parameters are provided in Table 2.1. As with the ITO model fits, the agreement between model and experiment is excellent except for occasional small systematic offset of the transmission fit in the nonabsorbing region. This offset is observed across the range of films tested and attributed to scattering from the film surface. The ellipsometric parameters, Ψ and Δ, are not altered by this minor scattering. They are derived from the ratio of two perpendicular light waves and do not report on absolute intensity as in a transmission or reflectance measurement. Note also that the drop in transmittance after ~600 nm is due to an interference fringe, thus k=0 in this region. As expected, the position of the interference fringe varied with thickness for films of the same composition.

Table 2.1. Model fit parameters from VASE analysis described by eq. 1 and 2 in text of $Mo_xW_{1-x}O_3$ films as a function of Mo fraction, *x*.

	X=0 WO_3	**x=0.03**	**x=0.17**	**x=0.44**	**x=0.61**	**X=0.74**	**x=1 α–MoO_3**
Thickness (nm)	114.2±0.2	88.9±0.1	156.6±0.1	118.6±0.2	113.7±0.1	86.4±0.1	80.1±0.1
$\varepsilon_1(\infty)$	1.56	2.24	2.03	1.99	2.01	1.79	1.88
T-L A	302.4	218.61	342.49	419.47	233.93	261.60	209.68
T-L E	3.67	3.84	3.56	3.38	3.82	3.72	4.45
T-L C	2.16	1.81	1.53	1.45	2.38	2.30	2.25
T-L E_g	3.37	3.38	3.42	3.38	3.31	3.26	3.42
Gaussian A	0.45	0.22	0.49	0.68	0.61	0.69	0.27
Gaussian E	3.41	3.45	3.49	3.40	3.45	3.37	3.61
Gaussian B	0.53	0.45	0.58	0.58	0.72	0.88	0.77

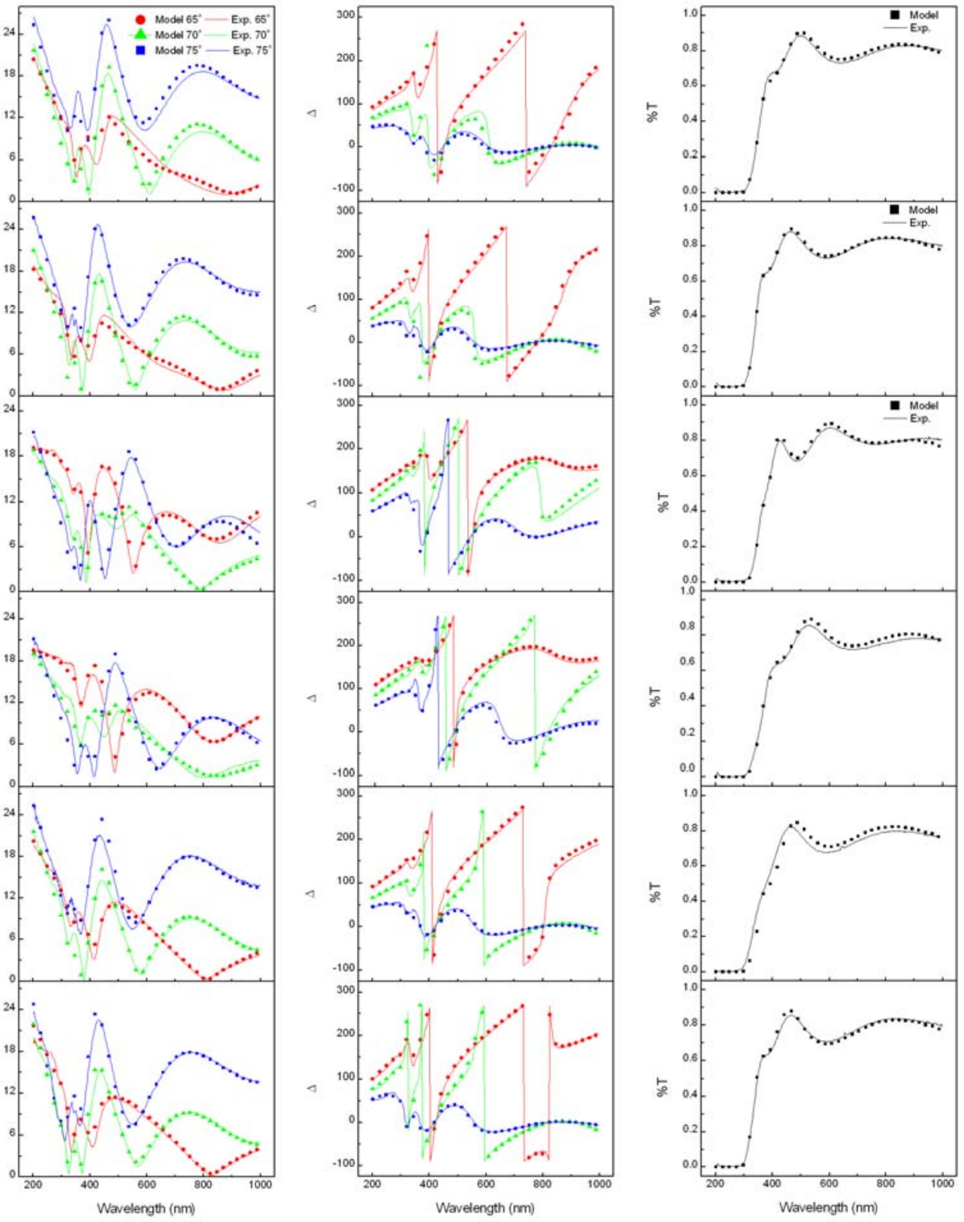

Figure 2.3. Plots of (a) Ψ, (b) Δ, and (c) %T versus wavelength for $Mo_{0.61}W_{0.39}O_3$ heat treated at 250°C for 2h. Ψ and Δ were determined at 60°, 65°, and 70°. Lines represent the experimental data while symbols are the model fit. d) Estimated optical constants for real component, *n*, and imaginary component, *k*, of the refractive index for $Mo_{0.61}W_{0.39}O_3$.

2.3.2.3 Ellipsometric Model of TiO_2

The real (*n*) and imaginary (*k*) portions of the complex refractive index were determined using spectroscopic ellipsometry. SE measurements were taken from 200 to 800 nm at angles of 60^o, 65^o, and 70^o using a J.A. Woolam M-2000 variable angle spectroscopic ellipsometer. These were combined with p-polarized transmission measurements from 300 to 800 nm taken on the same instrument. Model parameters were fit simultaneously to the variable angle spectroscopic ellipsometry and transmission measurements using the Levenburg-Marquardt algorithm. Initially the optical constants of ITO/glass were determined using a graded microstructure as described previously in the previous section. The optical constants of TiO_2-buffer layer and mesoporous titania film were determined with a T-L oscillator accounting for the band edge, a Gaussian just below the band gap, and an additional Gaussian accounting for absorption above the band gap which was greater than that predicted by the T-L oscillator (Figure 2.4). A Bruggeman effective medium approximation (BEMA) consisting of a mixture of bulk TiO_2 optical constants and void material ($n = 1$) was used to quantify the porosity in the films.[33] The bulk TiO_2 optical constants were determined from a TiO_2 thin film prepared by dip coating.

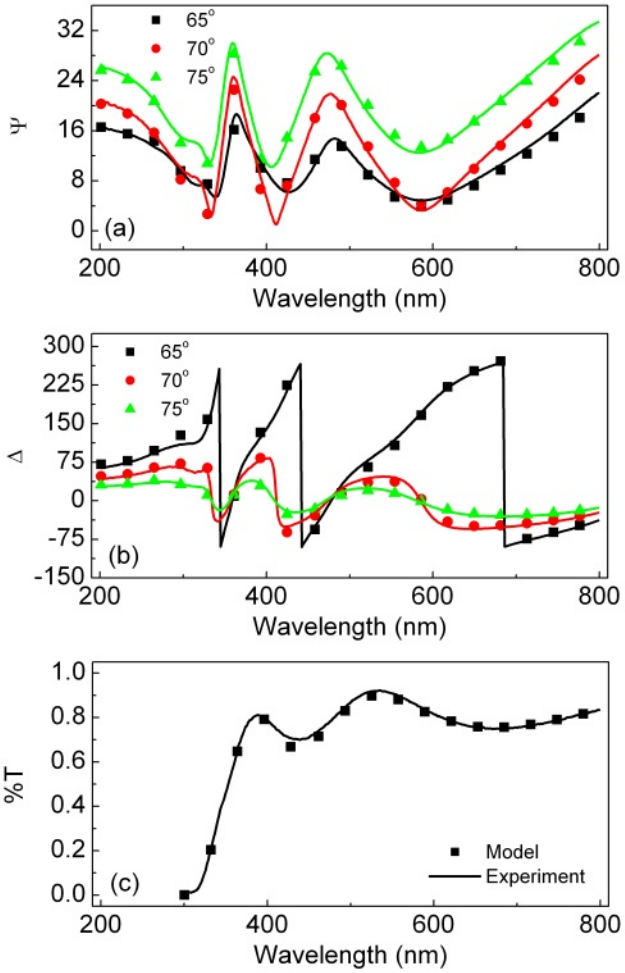

Figure 2.4. Representative (a) Ψ, (b) Δ, and (c) %T fits to ellipsometry and transmission data for mesoporous TiO_2.

2.3.3 Optical Constants of $Mo_xW_{1-x}O_3$

Derived optical constants for $Mo_xW_{1-x}O_3$ films as a function of wavelength and Mo fraction are presented in Figure 2.5. Also shown are optical constants determined for pure WO_3 and α-MoO_3. In the non-absorbing region between 500-1000 nm the real component of the refractive index, *n*, is sensitive to film density and composition.[34] In line with this the experimentally determined real part of the refractive index increased linearly with the increase in Mo content as an average of the WO_3 and MoO_3 optical constants ($R^2 = 0.99$) ranging from 2.07 to 2.20 at 800 nm (Figure 2.5 a inset). These values are comparable to previously reported literature values for $Mo_xW_{1-x}O_3$ films.[10,11,35] The lack of deviation from linearity also implies that the film densities change very little with the fraction of Mo. The imaginary component of the refractive index, *k*, is observed to fall to zero below the band gap (Figure 2.5 b) except for some tailing most likely due to the presence of oxygen defects.[36]

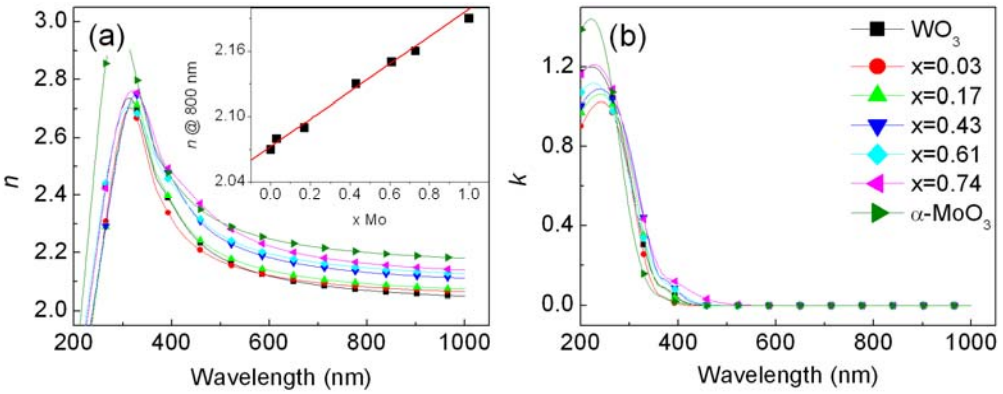

Figure 2.5. Plots of the (a) real component, *n*, and (b) imaginary component, *k*, of the refractive index versus wavelength for $Mo_xW_{1-x}O_3$ films supported on ITO with varying Mo fraction, *x*. Also shown are plots for pure WO_3 and α-MoO_3 films. (c) Plot of the real component of the refractive index, *n*, at 800 nm versus Mo fraction, *x*.

Quantifying the degree of oxygen deficiency in $Mo_xW_{1-x}O_3$ compositions is important since it can influence electronic properties. Although in this study we did not determine the amount of oxygen deficiency in these films, we believe that the amount of oxygen defects is consistent across the films for several reasons. First, the magnitude of absorption below the band gap is consistent across the tested films, indicating that the amount of oxygen defects is constant. Additionally, the films do not exhibit the blue tint characteristic of films with oxygen stoichiometry less than ~2.7[37]. Previously valence band XPS studies have shown that α-MoO_3 does not exhibit a significant defect band like the more oxygen deficient β-MoO_3[36]. From this previous work the oxygen stoichiometry was estimated to be between 2.7 and 2.8.[36] Small variations in the amount of oxygen defects and their effect on the band gap can not be entirely ruled out and will be the subject of future study. Further interpretation of the imaginary refractive index was performed by transforming k into the absorption coefficient (α) using the relationship $\alpha = 4\pi k/\lambda$ and implementing standard Tauc plots[19] to determine the optical band gap (E_g).

2.3.4. Band Gap Determination

2.3.4.1 Tauc Plots of $Mo_xW_{1-x}O_3$

For this data set the Tauc-Lorentz dispersion model's band gap fitting parameter, E_g, is an unreliable estimate of band gap because of correlation with the peak transition energy, E_0, and amplitude, A, fit parameters. More specifically the best fit E_g values fluctuated around ~3.3eV (Table 2.1), which is roughly the same as the band gaps derived using indirect Tauc plots.

However, more accurate determination of E_g using a fit procedure was impossible because several combinations of fit parameters led to equivalent optical constants and fits to experimental data. To determine the band gaps, Tauc plots of the form $(\alpha E)^{1/\eta}$ vs. eV were constructed for the high absorption region, $\alpha > 10^4$. The parameter η is related to the type of band gap transition. The η values tested were $\eta = 1/2$, $\eta = 3/2$, $\eta = 2$, and $\eta = 3$ corresponding to direct allowed, direct forbidden, indirect allowed, and indirect forbidden transitions.[38] Under each transition regime there is an expected change in the shape of the band edge, arising from the probability of the band gap transition occurring, which is reflected in the various values of η. After plotting $(\alpha E)^{1/\eta}$ vs. eV the quality of the linear fit determines which of the transition types is dominant.[39] For this analysis the difference between the fits for the different types of transitions was not significant, an ambiguity previously observed by Lasurdo et al. for nanocrystalline V_2O_5[22] and attributed to the lack of long range order within V_2O_5. Reviewing reports for $Mo_xW_{1-x}O_3$ films prepared via similar means [8,10,11,40,41] most optical band gaps have been determined using an indirect phonon assisted transition,η =2. This transition is expected for many amorphous films[19] and is considered here due to the disordered nature of our materials. Along with the mixed films, pure WO_3 and α-MoO_3 were analyzed by the same method and shown in Figure 2.6. The band gap for $Mo_xW_{1-x}O_3$ films as a function of Mo fraction decreases in a linear fashion, R^2= 0.99, (Figure 2.6 b). The pure WO_3, E_g= 3.16±0.04 eV, and α-MoO_3, E_g= 3.38±0.04 eV, films did not fit on the same linear trend for $Mo_xW_{1-x}O_3$ but are consistent with previously reported values.[2]

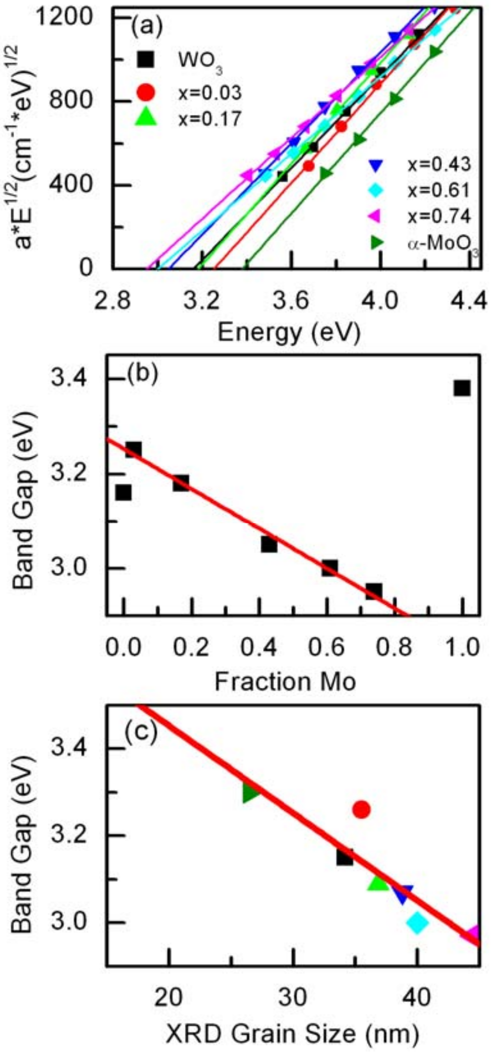

Figure 2.6. (a) Tauc plot $(\alpha E)^{1/2}$ versus eV for high absorption ($\alpha > 10^4$) region for $Mo_xW_{1-x}O_3$ films supported on ITO with varying Mo fraction. Also shown are plots for pure WO_3 and α-MoO_3. (b) Plot of optical band gap, E_g, versus Mo fraction, x. (c) Plot of optical band gap derived from (a) versus grain size determined from XRD.

However, comparison of the band gaps with the grain size derived by Scherrer analysis provides an explanation (Table 2.2). As mentioned previously, the estimated grain size for $Mo_xW_{1-x}O_3$ films increases with Mo content, a trend also observed for sol-gel derived Mo-W oxides.[10] The plot of grain size versus band gap (Figure 2.6 c) illustrates the inverse relationship between band gap and grain size. We note that the data point for the lowest fraction of Mo, x=0.04, fits the general trend but does not agree as well as the other compositions. We attribute this discrepancy to the difficulty in determining the grain size by Scherrer analysis, especially given the low intensity of the diffraction peaks observed for $Mo_xW_{1-x}O_3$ with small Mo fraction. The observed inverse relationship between grain size and band gap has been reported for several different systems including CdS[42] and V_2O_5[43] and is typically attributed to quantum size effects.[44] We were unable to find experimental values of the Bohr radius of MoO_3 or WO_3, however, TiO_2[45] and ZnO[44], have reported Bohr radii of ~3nm. Thus the grains of these films are larger than the Bohr radius and are described as being in the weak confinement regime[44]. In this regime, the energy is dominated by the Coulomb term and quantum effects arise from quantization of exciton motion.[44] It is important to note that the determination of grain size using Scherrer analysis can be somewhat imprecise and the linear relationship seen for grain size versus Mo fraction should not be over interpreted.

Table 2.2. Estimation of optical band gap, E_g, and grain size of $Mo_xW_{1-x}O_3$ films as a function of Mo fraction, *x*.

x in $Mo_xW_{1-x}O_3$	E_g (eV)	Grain size (nm)
0	3.16±0.04	34
0.03±0.01	3.25±0.07	36
0.17±0.01	3.18±-0.06	37
0.44±0.01	3.05±0.06	39
0.61±0.02	3.00±0.02	40
0.74±0.04	2.95±0.02	44
1	3.38±0.04	27

Other grain size analysis techniques such as SEM and AFM were not utilized for the $Mo_xW_{1-x}O_3$ films because the measured grain sizes are approaching their resolution limits and tend to observe aggregates rather than true grains. SEM images showing the surface morphology of similarly prepared $Mo_xW_{1-x}O_3$ films have been published previously[7]. Despite the vagaries of grain size determination, we clearly see that the band gap is highly correlated with the broadening of the XRD peaks and this broadening is indicative of an increase in grain size. This observation has not been made in other studies of mixed $Mo_xW_{1-x}O_3$ films because they have focused on differences in the optical properties of the films while ignoring changes in structure.[8,11,35] Taurino and coworkers[10] did report some structural analysis but did not include structural information or estimate grain size for amounts of Mo below 75%.

2.3.4.2 Band Gap of Pulse Deposited WO_3

To further investigate the relationship between grain size and band gap a series of WO_3 films was deposited using a pulsed electrodeposition technique[12] in effort to vary grain size. The advantage of this technique is that the grain size can be varied while keeping the deposition potential and post deposition thermal treatment constant. The band gaps were extracted as described above while the grain size was determined using AFM. Scherrer analysis could not be used in this case since the grain size was greater than 100 nm, a size large enough to not contribute to the broadening of an XRD peak[31]. Note also that these films have been deposited at the more reducing potential of -1 V vs. Ag/AgCl therefore the films are not directly comparable to WO_3 films deposited at -0.35 V. The shift to a more negative potential was necessary to increase the rate of WO_3 deposition. To quantify the change in grain size with pulse width a series of AFM images were acquired (Figure 2.7). The phase images are presented in addition to topography to better illustrate the grain boundaries. WO_3 films deposited with 5 ms pulse width exhibit grain sizes around 40 nm with a band gap of 3.42eV while WO_3 films deposited with 50 ms pulse width have grains ranging from 30 nm to 90 nm with a narrower band gap of 3.35 eV. Films deposited with the 100 ms pulse feature grain sizes ranging from 60 nm to 130 nm while those deposited with a 300 ms pulse width result in grains ranging from 80 nm to 180 nm. The indirect band gaps for these two WO_3 films are 3.20 eV and 3.21 eV, respectively. A plot of band gap versus grain size is shown in figure 2.8. The variation in grain size is interesting because very different quantum effects are expected within these size ranges. It is important to keep in mind that the band gaps are a bulk average of these individual contributions. The films deposited with 5 ms and 50 ms pulse widths exhibit the same inverse relationship between grain size and band gap as seen in the $Mo_xW_{1-x}O_3$ system. Similar effects of grain size on band gap for WO3 films have been reported by Baeck and coworkers[12].

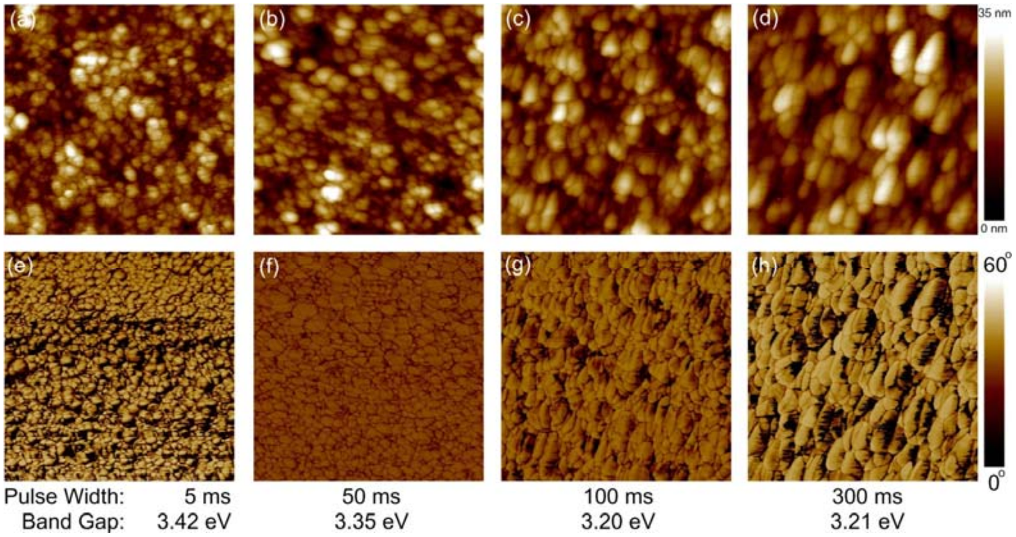

Figure 2.7. 1 x 1 μm^2 AFM phase images for WO_3 films deposited with (a) 5ms (b) 50ms (c) 100ms and (d) 300ms pulse widths. Estimated band gaps are indicated for each film.

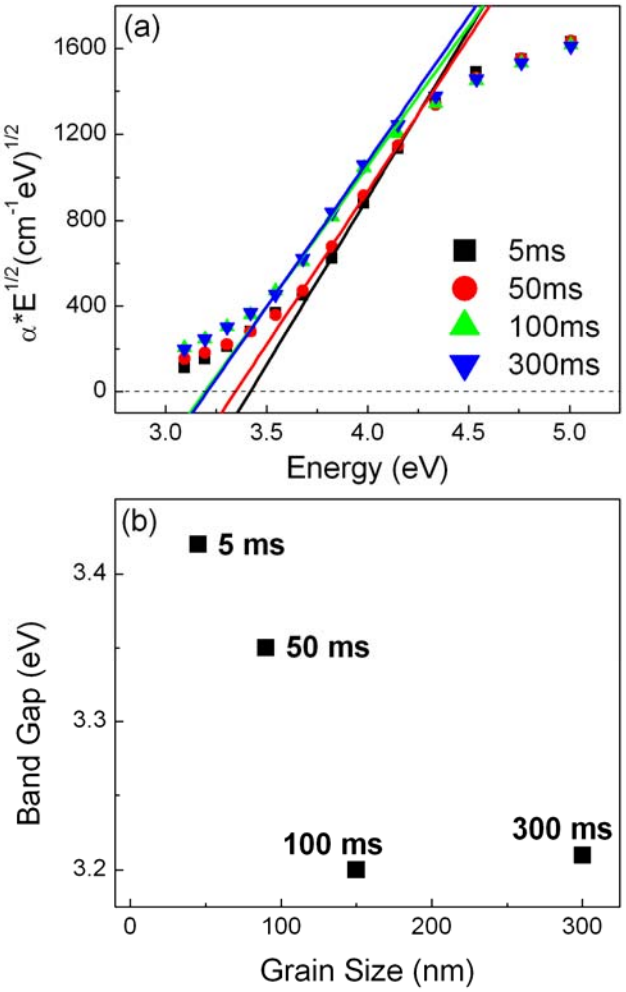

Figure 2.8. (a) Tauc plots derived from ellipsometry results for WO_3 deposited pulses of increasing length (b) the resulting band gap compared to grain size derived from AFM analysis.

The larger grain sizes, seen for films deposited with 100 ms and 300 ms pulse widths, display, as expected, even smaller band gaps. We note that the extracted band gaps from the films with the two largest grain sizes are nearly identical, indicating that quantum effects are not influential for films with large grain sizes. This leveling off of the band gap trend is important as it provides further support to the band gap shift arising from a quantum effect and not strain since we expect strain effects to persist through a larger size range.

2.3.4.3 Band Gap of Mesoporous TiO_2

The optical band gap of the mesoporous TiO_2 films was calculated using the same indirect Tauc plots used for previously discussed metal oxides. Values of *k* were determined from elliosometry and transmission measurements and then *k* was converted to the absorption coefficient, α, using the relationship $\alpha = 4\pi k/\lambda$. Then plots of and $\alpha E^{1/2}$ versus E for indirect type transitions were constructed.[19] To determine the optical band gap, the best fit line in the region of high absorption ($\alpha > 10^4$) was extrapolated back to the *x* axis (Fig. 2.9). The indirect band gap of TiO_2 is 3.22 eV while for mesoporous TiO_2 it is 3.43 eV. This increase of band gap after templating 10 nm columns is consistent with the trend observed for mixed $Mo_xW_{1-x}O_3$ and pulsed deposition deposited WO_3. Increased optical bandgap energies have also been observed on other nanostructured titania materials, such as mesoporous films or nanotube arrays,[48-50] where the higher energies were attributed to quantum size effects of TiO_2 nanocrystals with sizes of less than

10 nm.[51-53] Similarly, the mesoporous titania films in this study appear to exhibit quantum size effects which influence their optical and electronic properties.[42-44]

Our results strongly suggest that that the structure of these materials plays an important role in determining electronic properties meaning that future doping studies that attempt to correlate optical and electronic properties with composition must be mindful of changes due to structure and, not just composition.

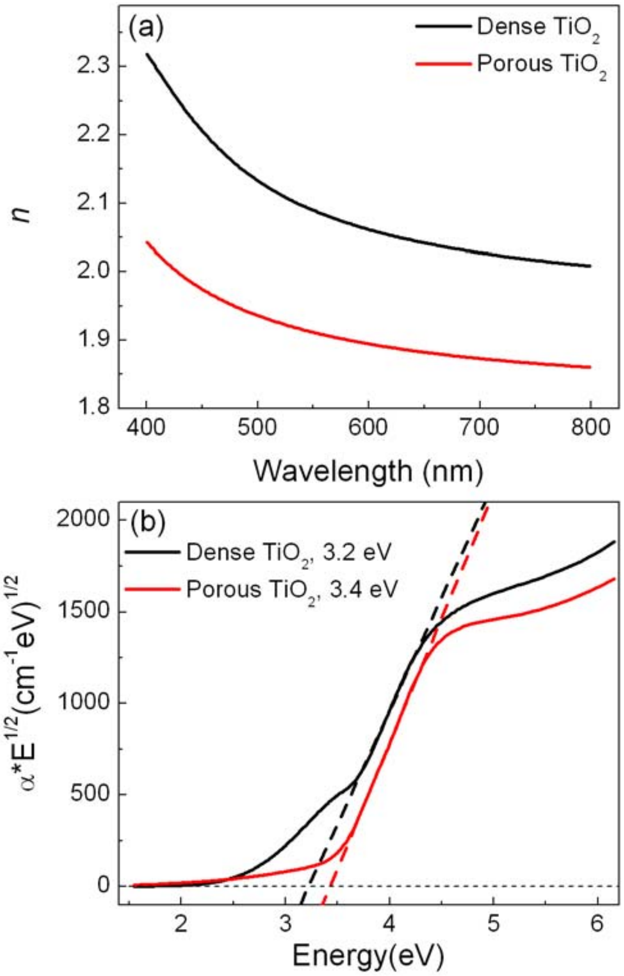

Figure 2.9. (a) Real refractive index (n) for untemplated and templated TiO_2. (b) Indirect Tauc plot used to derive the band gap of dense and porous TiO_2.

2.4 CONCLUSION

MoO_3, WO_3, and mixed $Mo_xW_{1-x}O_3$ with $0 < x < 1$ films were electrodeposited onto indium tin oxide (ITO) substrates from peroxo-polymolybdotungstate solutions. Additionally, mesoporous TiO_2 was cast on ITO using a templated sol gel technique. The optical constants of these samples were derived using spectroscopic ellipsometry and transmission measurements from 200-1000 nm (1.24-6.2eV). Good model fits for ITO and the supported metal oxide films were achieved using a combination of Tauc-Lorentz oscillators to express band edges and Gaussian oscillators to describe tailing below the band gap. The real component of the refractive index is observed to scale linearly with increasing Mo fraction in the mixed molybdenum-tungsten oxide films while analysis of the imaginary component (absorptivity) indicates a narrowing of the band gap with increasing grain size in WO_3, $Mo_xW_{1-x}O_3$, and TiO_2.

2.5 REFERENCES

(1) Julien, C. M. *Materials Science & Engineering, R: Reports* **2003**, *R40*, 47-102.

(2) Granqvist, C. G. *Handbook of Inorganic Electrochromic Materials*; Elsevier, 1995.

(3) He, T.; Yao, J. *Progress in Materials Science* **2006**, *51*, 810-879.

(4) Mukherjee, N.; Paulose, M.; Varghese, O. K.; Mor, G. K.; Grimes, C. A. *Journal of Materials Research* **2003**, *18*, 2296-2299.

(5) Monk, P. M. S.; Ali, T.; Partridge, R. D. *Solid State Ionics* **1995**, *80*, 75-85.

(6) Monk, P. M. S.; Bleazard, S.; Akhtar, S. P.; Boutevin, J. *Phys. Chem. Chem. Phys.* **2000**, *2*, 4415-4419.

(7) Kondrachova, L.; Hahn, B. P.; Vijayaraghavan, G.; Williams, R. D.; Stevenson, K. J. *Langmuir* **2006**, *22*, 10490-10498.

(8) Faughnan, B. W.; Crandall, R. S. *Appl. Phys. Lett.* **1977**, *31*, 834-836.

(9) Vomiero, A.; Della Mea, G.; Ferroni, M.; Martinelli, G.; Roncarati, G.; Guidi, V.; Comini, E.; Sberveglieri, G. *Materials Science & Engineering, B: Solid-State Materials for Advanced Technology* **2003**, *B101*, 216-221.

(10) Taurino, A.; Catalano, M.; Rella, R.; Sicilliano, P.; Wlodarski, W. *Journal of Applied Physics* **2003**, *93*, 3816-3822.

(11) Gesheva, K.; Szekeres, A.; Ivanova, T. *Solar Energy Materials & Solar Cells* **2003**, *76*, 563-576.

(12) Baeck, S. H.; Jaramillo, T.; Stucky, G. D.; McFarland, E. W. *Nano Lett. FIELD Full Journal Title:Nano Letters* **2002**, *2*, 831-834.

(13) Abramooff, M. D.; Magelhaes, P. J.; Ram, S. J. **2004**, *11*, 36-42.

(14) Alberius, P. C. A.; Frindell, K. L.; Hayward, R. C.; Kramer, E. J.; Stucky, G. D.; Chmelka, B. F. *Chem. Mater.* **2002**, *14*, 3284.

(15) Wu, C. W.; Ohsuna, T.; Kuwabara, M.; Kuroda, K. *J. Am. Chem. Soc.* **2006**, *128*.

(16) Tompkins, H. G.; McGahan, W. A. *Spectroscopic Ellipsometry and Reflectometry*; Wiley-Interscience, 1999.

(17) Synowicki, R. A. *Thin Solid Films* **1998**, *313-314*, 394-397.

(18) Jellison, G. E.; Modine, F. A. *Appl. Phys. Lett.* **1996**, *69*, 371-373.

(19) Tauc, J. In *Amorphous and Liquid Semiconductors*; Tauc, J., Ed.; Plenum Press: 1974, p 159-220.

(20) Desmet, D. J.; Ord, J. L. *J. Electrochem. Soc. : Electrochemical Science and Technology* **1983**, *130*, 280-284.

(21) Itoh, M.; Hayakawa, K.; Oishi, S. *Journal of Physics: Condensed Matter* **2001**, *13*, 6853-6864.

(22) Losurdo, M.; Barreca, D.; Bruno, G.; Tondello, E. *Thin Solid Films* **2001**, *384*, 58-64.
(23) McEvoy, T. M.; Stevenson, K. J.; Hupp, J. T.; Dang, X. *Langmuir* **2003**, *19*, 4316-4326.
(24) Dobson, M. M.; Tilley, R. J. D. *Acta Crystallographica, Section B: Structural Science* **1988**, *B44*, 474-80.
(25) Figlarz, M. *Progress in Solid State Chemistry* **1989**, *19*, 1-46.
(26) Kimizuka, N.; Akahane, T.; Matsumoto, S.; Yukino, K. *Inorganic Chemistry* **1976**, *15*, 3178-9.
(27) Roth, R. S.; Waring, J. L. *J. Res. Natl. Bur. Std., A* **1966**, *70*, 281-803.
(28) Salje, E.; Gehlig, R.; Viswanathan, K. *Journal of Solid State Chemistry* **1978**, *25*, 239-50.
(29) Woodward, P. M.; Sleight, A. W.; Vogt, T. *Journal of Physics and Chemistry of Solids* **1995**, *56*, 1305-15.
(30) Klug, H. P.; Alexander, L. E. *X-Ray Diffraction Procedures for Polycrystalline and Amorphous Materials. 2nd ed*, 1974.
(31) Cullity, B. D. *Elements of X-Ray Diffraction. 2nd Ed*, 1978.
(32) Kim, S.-S.; Choi, S.-Y.; Park, C.-G.; Jin, H.-W. *Thin Solid Films* **1999**, *347*, 155-160.
(33) Mergel, D. *397* **2001**, 216.
(34) Kakiuchida, H.; Shimodaira, N.; Sekiya, E. H.; Saito, K.; Ikushima, A. J. *Appl. Phys. Lett.* **2005**, *86*, 1-3.
(35) Khawaja, E. E.; Durrani, S. M. A.; Daous, M. A. *J. Phys.: Condens. Matter* **1997**, *9*, 9381-9392.
(36) McEvoy, T. M.; Stevenson, K. J. *Langmuir* **2005**, *21*, 3521-3528.
(37) Li, S.; Germanenko, I. N.; El-Shall, M. S. *Journal of Cluster Science* **1999**, *10*, 533-547.
(38) Pankove, J. I. *Optical Processing in Semiconductors*; Dover Publications, 1971.
(39) Wooten, F. *Optical Properties of Solids*; Academic Press, 1972.
(40) Tazawa, M.; Jin, P.; Tanemura, S. *Applied Optics* **1998**, *37*, 1858-1861.
(41) Losurdo, M.; Bruno, G. *Applied Physics Letters* **2000**, *77*, 1129-1131.
(42) Cortes, A.; Gomez, H.; Marotti, R. E.; Riveros, G.; Dalchiele, E. A. *Solar Energy Materials and Solar Cells* **2004**, *82*, 21-34.
(43) Losurdo, M.; Barreca, D.; Capezzuto, P.; Bruno, G.; Tondello, E. *Surface and Coatings Technology* **2002**, *151-152*, 2-8.
(44) Yoffe, A. D. *Advances in Physics* **1993**, *42*, 173-266.
(45) Dittrich, T.; Duzhko, V.; Koch, F.; Kytin, V.; Rappich, J. *Phys. Rev. B: Condens. Matter Mater. Phys.* **2002**, *65*, 155319/1-155319/5.
(46) Asahi, R.; Taga, Y. *J. Phys. Rev. B* **2000**, *61*, 7459.

(47) Sankapal, B. R.; Lux-Steiner, M. C.; Ennaoui, A. *Appli. Surf. Sci* **2005**, *239*, 165.

(48) Smarsly, B.; Grosso, D.; Brezesinski, T.; Pinna, N.; Boissiere, C.; Antonietti, M.; Sanchez, C. *Chem. Mater.* **2004**, *16*.

(49) Wang, N.; Lin, H.; Li, J.; Tang, X.; Chi, B. *Thin Solid Films* **2006**, *496*.

(50) Yu, J. C.; Wang, X.; Fu, X. *Chem. Mater.* **2004**, *16*.

(51) Hoffmann, M. R.; Martin, S. T.; Choi, W.; Bahnemann, D. W. *Chem. Rev.* **1995**, *95*, 69.

(52) Yu, J. C.; Zhang, L.; Yu, J. *Chem. Mater.* **2002**, *14*, 4647.

(53) Yu, J. C.; Zhang, L.; Yu, J. *Chem. Mater.* **2003**, *15*, 2280.

CHAPTER 3

Flow Based Multi-Adsorbate Ellipsometric Porosimetry for the Characterization of Mesoporous Pt-TiO_2 and Au-TiO_2 Nanocomposites[†]

3.1 INTRODUCTION

Titanium dioxide is a versatile material which has applications in catalysis[1], photovoltaics[2], and energy storage[3]. Applications utilizing TiO_2-based systems directly depend on the ability to prepare nanostructured materials with controllable features such as porosity, surface area, and composition. Several strategies have been employed to improve the performance of these systems, including tailoring of titania structure (e.g. particle size) and surface modification with metal nanoparticles.[4,5] In particular, the loading of metal nanoparticles upon and within a mesoporous titania host is driven by a desire to improve absorption in the visible light region, since TiO_2 mainly absorbs the UV component of solar radiation due to its relatively large bandgap (3.2 eV). Several routes for preparing metal-TiO_2 composites have been attempted, including liquid phase routes[6], sol–gel[7], sputtering[8], chemical vapor deposition[9], and pulsed laser deposition[10]. However, in these 'one pot' synthesis schemes the annealing conditions are restricted to those that will not cause significant agglomeration or passivation

---

[†] Portions of this chapter were published in May, R. A.; Patel, M. N.; Johnston, K. P.; Stevenson, K. J. *Langmuir* **2009,** 25, (8), 4498-4509.

of the nanoparticles. Another way to introduce nanoparticles into the material is to synthesize a hierarchically templated porous film with an ordered pore structure into which presynthesized nanoparticles can be introduced, a process driven largely by diffusion that can also be enhanced by the application of an electric field[11-15]. This approach suffers from difficulties in achieving high loadings with a homogeneous distribution of particles because of the interplay between the chemical and physical properties of the mesoporous TiO_2 and the metal nanoparticles. For example, high loadings, above 10 wt. %, of pre-synthesized FePt nanocrystals (< 4 nm), on mesoporous SiO_2 were achieved in 10 minutes, by promotion of strong metal-support interactions using weakly bound oleic acid and oleylamine capping ligands.[14] Previously, we described an approach for preparing mesoporous TiO_2 films with vertically oriented pores loaded with up to 21 wt. % Au nanoparticles.[13] These composite materials are very challenging to characterize by conventional means due to their mixed composition and small feature size. For example, films with pore sizes, ~10 nm, are typically too small to be adequately evaluated by atomic force microscopy (AFM) due to geometric distortions between probe tip and surface.[13,16] Other techniques such as scanning electron microscopy (SEM) are generally limited to profiling the top-most surface features. Additionally, for materials synthesized in limited quantities, such as those described herein, the amount is not enough for common mass/pressure transducer based adsorption porosimetry. Thus, new methodologies are needed to probe the structure, surface area, and porosity of nanostructured composite materials. Several methods have been developed for this task including optical methods such as ellipsometric porosimetry[17], and methods based on the measurement of mass change such as surface acoustic wave[18,19] or quartz crystal microbalance porosimetry[20].

We have been exploring the use of ellipsometric porosimetry (EP) as a means for assessing both general thin film properties (optical constants, film thickness) and porosity. EP has been applied in ambient and ultra high vacuum environments to a wide range of oxides[17,21-24], and has been validated against other thin film porosimetry techniques such as X-ray reflectivity (XRR) and neutron scattering.[25,26] Previously, we used ellipsometry to determine the pore volume of mesoporous TiO_2 films and to assess the loading of Au nanoparticles electrophoretically deposited within the TiO_2 film.[13] In this study, we explore the use of multiple adsorbates of varying polarities (toluene, ethanol, and water) in conjunction with UV modification of the TiO_2 surface properties to probe how adsorbate-TiO_2 interactions alter the resulting isotherms.[27] This approach is important because the choice of adsorbate can alter the parameters derived from an isotherm, and many flow based EP measurements have been performed with only water as an adsorbate[21-23,28,29], thereby, limiting the ability to understand the effects of non-ideal adsorbate-adsorbent interactions. Additionally, by comparing the results for adsorbates with different polarities and sizes, the influence of confinement effects on the adsorbate refractive index (n_{ads}) can be more fully assessed. Previously, it has been claimed that confinement of the adsorbate in mesopores can alter n_{ads} to such a degree that special analysis techniques are required to exclude n_{ads} from the analysis.[29] The assumptions required to ignore n_{ads} are limiting because the film porosity must be known and the pores must be fully accessible to the adsorbate. EP measurements of Pt-TiO_2 and Au-TiO_2 nanocomposites requires special consideration because the nanoparticles introduce complications by blocking pore volume and increasing the complexity of optical models used to extract optical constants such as n from the SE data. Thus, not knowing n_{ads} would preclude the use of EP on Pt-TiO_2 and Au-TiO_2 nanocomposites. Fortunately, the finding that n_{ads} is negligibly altered by confinement effects means that the Pt-TiO_2 and Au-TiO_2 nanocomposites can be characterized accurately by EP. Thus, for the first time, EP measurements of mesoporous TiO_2 films loaded with Au and Pt nanoparticles are reported. The EP data, in conjunction with XPS depth profiling measurements, are used to explore the relationship between particle size and the resulting distribution of metal nanoparticles throughout the mesoporous TiO_2 film.

3.2 EXPERIMENTAL

All chemicals were used as received. Titanium (IV) isopropoxide ($Ti(O{\cdot}i\text{-}C_3H_7)_4$) (97 %), hydrogen tetrachloroaurate(III) trihydrate ($HAuCl_4{\cdot}3H_2O$) (99.9%), tetraoctylammonium bromide ($(C_8H_{17})_4$-NBr) (98%), sodium borohydride ($NaBH_4$) (99%), platinum (IV) chloride (99.9%), dodecylamine (98%), perchloric acid 70% (99.999% purity), tetradecylammonium bromide (98%), and 1-dodecanethiol ($C_{12}H_{25}SH$) (98%)

were purchased from Sigma-Aldrich. Toluene (99.9%), chloroform (99.9%), hydrocholoric acid (HCl) (35.5 %), ethanol (C_2H_5OH) (Absolute 200 proof), and 2-propanol ($(CH_3)_2CHOH$) (99.9 %) were purchased from Fisher Scientific. Non-ionic triblock copolymer surfactant Pluronic P123 (poly-(ethylene oxide) poly-(propylene oxide) poly-(ethylene oxide) EO_{20}-PO_{70}-EO_{20}) was supplied by BASF. Water (H_2O) was double-distilled and deionized. Si wafers with mirror-polished (100) surface were obtained from Wafer World, Inc.

3.2.1 Preparation of Mesoporous TiO_2

Mesoporous titania films were prepared by self-assembly of block copolymer surfactants in sol-gel solution as described elsewhere.[30] Briefly, 1.05 g of $Ti(O{\cdot}i\text{-}C_3H_7)_4$ was hydrolyzed using 0.74 g of concentrated aqueous HCl under stirring for 10 min at room temperature. The hydrolyzed sol was mixed with 0.2 g of Pluronic P123 surfactant dissolved in 3.0 g of ethanol while stirring for 15 min at room temperature. The resulting solution was spin-coated on the Si substrates at a rate of ~7500 rpm for 60 seconds, followed by aging at -10 ^oC for 2 days under a controlled humidity of ~45–55%. The samples were subsequently calcined in a tube furnace at 400 ^oC for 4 h in air with a heating rate of 1.0 ^oC/min to remove the block copolymer template and fix the mesoporous structure of the film.

3.2.2 Preparation of Nanoparticles

Platinum nanoparticles stabilized by dodecylamine were synthesized using a phase-transfer method.[31] 15 mL of 60 mM platinum (IV) chloride was combined with 105 mL of toluene containing 1.5 g of tetradecylammonium bromide. The mixture was stirred for 2 h leading to platinum transfer from the aqueous phase to the organic phase. The organic phase was recovered, and 3.4 g of dodecylamine dissolved in 15 mL of toluene was added with continuous stirring. Platinum (IV) chloride was then reduced by the drop wise addition of 25 mL of 0.60 M sodium borohydride ($NaBH_4$). Upon reduction, the solution turned dark brown and was stirred for 2 hours. The Pt nanoparticles were subsequently washed and finally dispersed in toluene. The Pt nanoparticles were 1.7 ± 0.4 nm in diameter as measured by transmission electron microscopy (TEM) (Figure 3.1).

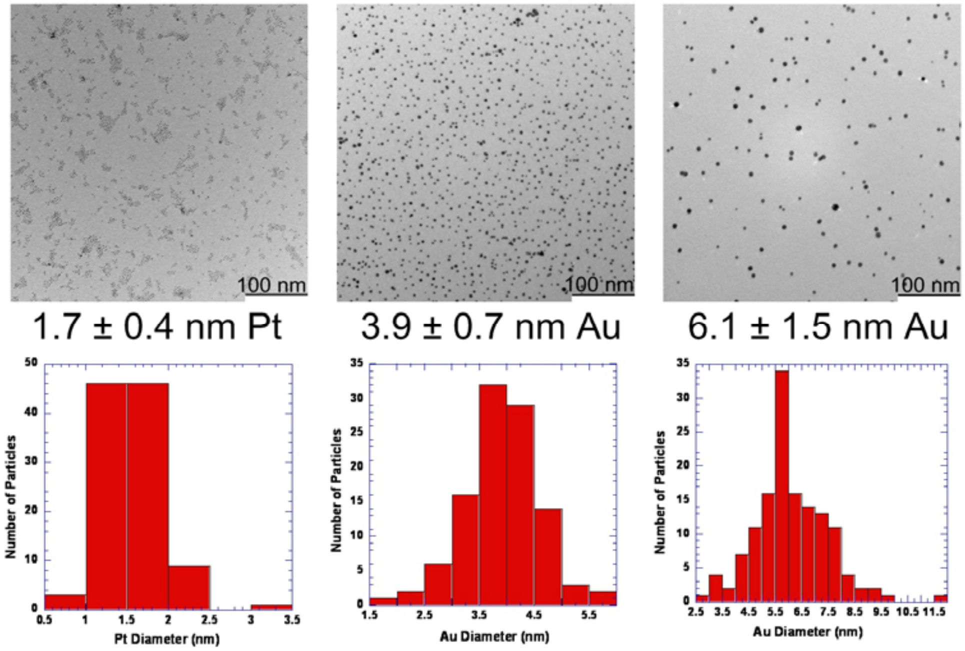

Figure 3.1. TEM images and representative histograms of Pt and Au nanocrystals.

Au nanoparticles were synthesized by a two-phase arrested precipitation technique[32,33] where 8 mL of aqueous (0.034 M) hydrogen tetrachloroaurate(III) trihydrate ($HAuCl_4 \cdot 3H_2O$) was combined with 15 mL of toluene containing 0.65 g of tetraoctylammonium bromide (TOAB). After stirring for 1 h, the organic phase, now containing the transferred Au, was collected. $AuCl_4^-$ was then reduced using 8 mL of 0.44 M $NaBH_4$, resulting in Au nanoparticles dispersed in toluene, and protected by TOAB. After 80 min, 0.120 mL of dodecanethiol was added to arrest the growth and cap the Au nanoparticles. After another hour of stirring the Au nanoparticles were washed and size selected using ethanol as an antisolvent. Finally, the Au nanoparticles were dispersed in toluene. According to TEM the Au nanoparticles capped with dodecanethiol were 3.9 ± 0.7 nm in diameter (Figure 3.1).

Larger Au nanopaticles were synthesized in a similar manner with the exception that no dodecanethiol was added. The Au nanoparticles were allowed to grow overnight with TOAB as the capping ligand. The nanoparticles were washed in dilute sulfuric acid and five times in DI water.[34] Anhydrous sodium sulfate was added to dry the nanoparticle dispersion. The resulting Au nanoparticles capped with TOAB were 6.1 ± 1.5 nm in diameter (Figure 3.1). Note that all the quoted particle diameters do not include contributions from the capping ligands which are not well resolved by TEM. These ligands add ~4 nm to the diameter of the particle; however for simplicity the particle diameters are discussed in terms of the measured TEM diameter. Mesoporous TiO_2 films were immersed in the corresponding Au or Pt nanoparticle solution for 18 hours. The solution was shaken to enhance nanoparticle loading. Following immersion the films were removed, rinsed with toluene, and heat treated at 110 °C for 2 h to remove residual toluene.

3.2.3 SEM and XPS analysis

SEM images were acquired with a LEO 1530 SEM equipped with an energy dispersive spectroscopy (EDS) system operated with a 20 keV electron beam and 60 μm aperture utilized to determine the weight percent of Pt and Au in the mesoporous TiO_2 films. X-ray photoelectron spectroscopy (XPS) was carried out on a Physical Electronics (PHI) model 5700 spectrometer employing a monochromatic Al $K\alpha_{1,2}$ source. The binding energy of the instrument was calibrated using $Au_{4f7/2}$, $Cu_{2p3/2}$ and $Ag_{3d5/2}$ to 84.0, 932.6, and 368.3 eV, respectively. Typical operating conditions were: 1×10^{-9} Torr chamber pressure; 14 kV; 250W for the Al X-ray source. Survey scans were acquired with a pass energy of 93.9 eV, while high-resolution elemental scans of Pt_{4f}, Au_{4f} and Ti_{2p} regions were collected with a pass energy of 11.75 eV at takeoff angles of 45° between the sample and analyzer. Ar ion sputtering was used for depth profiling. The ion beam energy was 2 keV and the ion beam current was 1 μA. A First Ten Angstroms model FTA200 instrument was used to determine the static contact angle of the various adsorbates.

3.2.4 Ellipsometry Analysis

Ellipsometry measurements at 65^o, 70^o, and 75^o from 200 nm to 1000 nm were acquired on a J.A. Woolam M-2000 variable angle spectroscopic ellipsometer (VASE). The acquired ellipsometric parameters Ψ and Δ are related to the ratio of the Fresnel reflection coefficients by the equation, $\rho = r_p / r_s = \tan(\Psi) e^{i(\Delta)}$[35]. Using this relationship the thickness, as well as, the real, *n*, and imaginary, *k*, components of the complex refractive index were determined. However, since Ψ and Δ can only be transformed directly in the case of a bulk substrate, an optical model was developed to interpret them. For the mesoporous TiO_2 samples a three layer model consisting of a Si substrate, a thin native SiO_2 layer, and the Cauchy equation was utilized to describe the TiO_2 film itself. The Cauchy equation assumes that the film is non absorbing, $k = 0$, and that normal dispersion of *n* is described by the equation, $n(\lambda) = A + B/\lambda^2$, where A and B are fit parameters and λ is the wavelength of light in microns. For analysis of the mesoporous TiO_2 films, the wavelength region was restricted to a non-absorbing region from 450 nm to 1000 nm. Anisotropy of the optical constants was not observed and an isotropic Cauchy model resulted in good agreement between model and experiment (Figure 3.2 a & b).

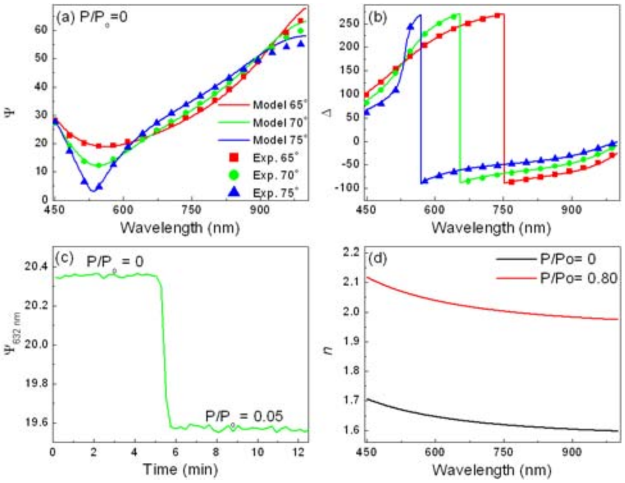

Figure 3.2. Representative Cauchy model fits to (a) Ψ and (b) Δ data collected for mesoporous TiO_2 on Si sintered at 400°C. (c) $\Psi_{632\ nm}$ at 70° monitored in real time during the introduction of $P/P_o = 0.05$ of toluene. (d) n vs wavelength for a sample at $P/P_o= 0$, compared to a sample saturated with toluene at $P/P_o= 0.80$.

3.2.5 Ellipsometric Porosimetry

EP measurements were carried out by flowing a mixture of high purity dry N_2 and a saturated N_2 stream generated by flowing through two bubblers containing the adsorbate of interst over the sample at a flow rate of 2 L^*min^{-1}. All measurements were carried out in a class 1000 clean room with a controlled temperature of 19.8 ± 0.1 ºC and a relative humidity of 48 % ± 2 %. Prior to the porosimetry runs the films were degassed for 2 hours at 110 ºC and then placed in a dry N_2 stream until the ellipsometry signal stabilized. Four different adsorbates were used; ultrapure deionized water (18 MΩ cm), ethanol (100% Pharmco USP grade), toluene (Fischer ACS grade), and n-hexane (95%, <50ppm water, Acros Organics). Flow was controlled using rotometers which were calibrated with a bubble flow meter. The standard error about the calibration curve was 3%. A Fisherbrand traceable digital hygrometer was used to verify that the gas manifold setpoints matched those measured within the test chamber during the adsorption and desorption of water. The results are given in Figure 3.3, the measured values agree with the manifold setpoint well within the ± 2 % accuracy error associated with the hygrometer.

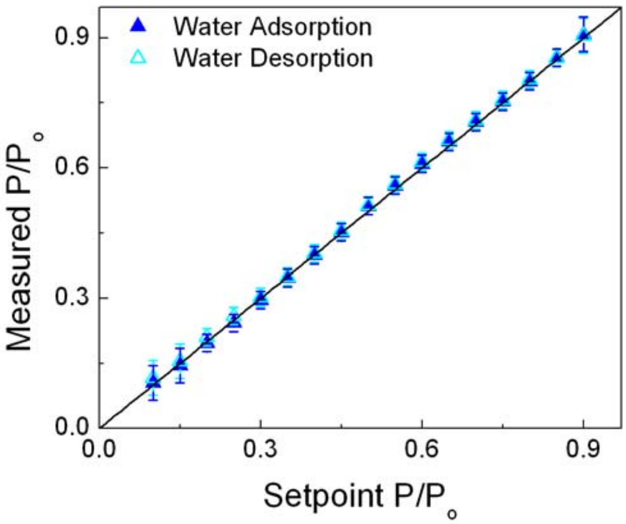

Figure 3.3. Comparison of the instrument setpoint partial pressure (P/Po) and that measured using a hygrometer for water adsorption (▲) and desorption (△). A line of y=x is shown to indicate agreement between the setpoint values and those measured with the hygrometer.

The sample was enclosed by a semicircular quartz tube, allowing for the determination of Ψ and Δ at multiple angles of reflection[24]. Acquiring data at multiple angles is important because it can enhance sensitivity and reduce parameter correlation during the fitting process. During testing the quartz tube had a minimal effect on the resulting signal with a mean absolute change of less than 1% across the wavelength range, a figure showing the effect of the tube on Ψ and Δ (Figure 3.4). Equilibrium was determined by monitoring changes in Ψ and Δ over time. In general, equilibrium was reached in under a minute (Figure 3.2 c) and a full isotherm was typically completed in 4 to 5 hours after the sample had been degassed.

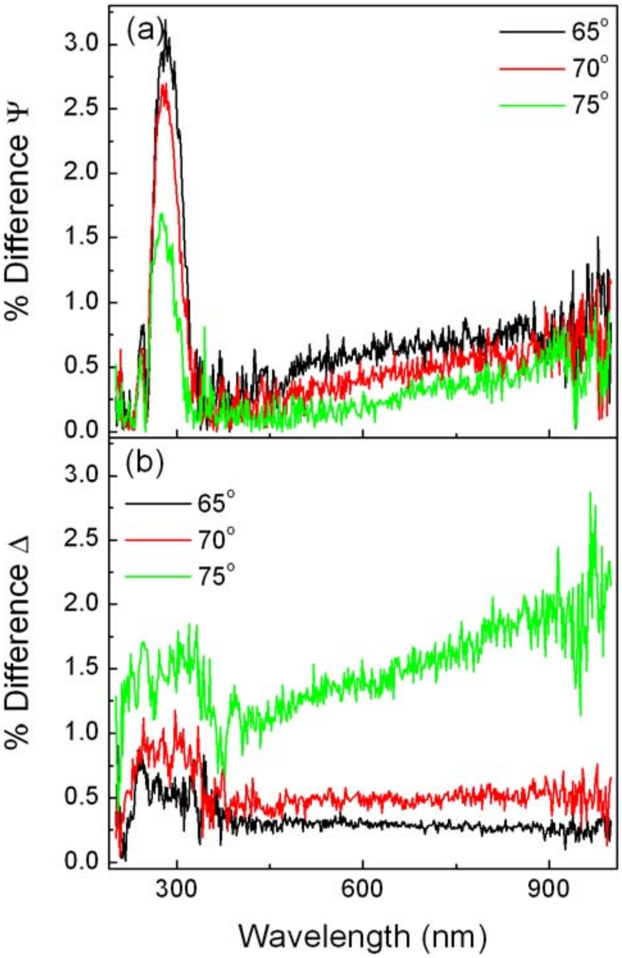

Figure 3.4. Absolute percent difference between a Si wafer covered and not covered by the quartz tube used in porosimetry experiments for (a) Ψ and (b) Δ, at 65° (black), 70° (red), and 75° (green). The average absolute difference is 0.7% and the measured oxide thickness changed from 27.9 nm to 27.7 nm.4

3.2.6 Isotherm Analysis

Analysis of the resulting isotherms was performed using methods of analysis frequently used in powder porosimetry, i.e., the Kelvin equation to determine the mesopore size distribution and the BET equation to determine the surface area. The Kelvin equation (eq.1) is derived based on the behavior of fluid in a capillary. The pore radius is estimated from the radius of the meniscus formed in this capillary and the equation is considered valid for determining pore sizes in the 2 to 50 nm range. The equation is often written without the cos(θ) term, implicitly assuming that the contact angle is 0°. However, utilization of the contact angle, derived from measurements on a similarly prepared nonporous film, has been shown to improve agreement between the Kelvin equation and confirming measurements.[36]

$$r_\kappa = \frac{-2\gamma V_m \cos(\theta)}{RT \ln\left(P/P_0\right)} \tag{1}$$

$$r = r_k + t \tag{2}$$

Equation 1 is the Kelvin equation formulated for a cylindrical pore closed on one end, where r_k is the radius of the meniscus, γ is the surface tension of the adsorbate, V_m is the liquid adsorbate molar volume, θ is the contact angle, R is the gas constant, T the temperature, and P/P_o the partial pressure of adsorbate. For the adsorption of toluene $\gamma = 0.0284\ \text{N*m}^{-1}$, $V_m = 1.06 \times 10^{-4}\ \text{m}^{3*}\text{mol}^{-1}$, $R = 8.314\ \text{J*mol}^{-1}\text{*K}^{-1}$, and T= 290 K.[37] The actual pore radius (r) also consists of the adsorbate preadsorbed on the pore wall (t), eq. 2. This value was determined from isotherms performed on untemplated TiO_2 sol gels as well as from the Halsey-Wheeler equation. To obtain the PSD, the derivative of volume adsorbed with respect to r_k was plotted versus r_k. The surface area of the films was estimated using the BET equation (eqn. 3).[38]

$$\frac{P/P_0}{v(1-P/P_0)}=\frac{1}{v_m c}+\frac{P/P_0\,(c-1)}{v_m c} \qquad 3)$$

Data for the adsorption of toluene, ethanol, and water was used to construct a BET plot from $P/P_o= 0.05$ to $P/P_o= 0.35$, except for toluene which typically deviated from linearity after $\sim P/P_o= 0.25$. Using the BET plot the volume of a monolayer of adsorbate, ν_m, and the BET constant c, which is related to the strength of adsorbate adsorbent interaction, were calculated. ν_m was then employed to calculate the surface area of the mesoporous TiO_2.

3.3 RESULTS AND DISCUSSION

3.3.1 Mesostructure of TiO_2

As cast mesoporous TiO_2 films contain an ABAB stacked hexagonally packed array of surfactant templated spheres.[30] Upon sintering, the surfactant is removed leaving behind columnar mesopores with few interconnects. These columns retain the ABAB stacking pattern, presenting a more tortuous path than would be expected from a true cylindrically shaped pore structure, potentially interfering with the distribution of nanoparticles throughout the porous network. These vertically aligned mesopores have openings of 10 ± 2 nm as determined previously by SEM[13] and illustrated by the images in Figure 3.5. The films are well ordered and, when formed on Si wafers, the films have a mean porosity of 55 ± 1 vol. %, as determined by fitting ellipsometry data for the void fraction using a Bruggeman effective medium approximation (BEMA). The mean film thickness, as derived using the Cauchy model to fit SE data for eight different samples, was 212 ± 8 nm, a measurement that was verified using atomic force microscopy (AFM). Following heating at 400 ºC the material crystallizes into anatase TiO_2 as indicated by a peak at $2\theta \approx 25°$ for X-ray diffraction (XRD) measurements, Figure 3.5.

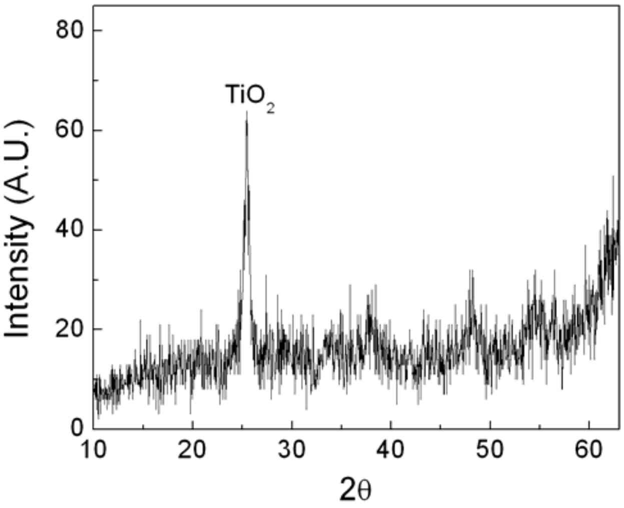

Figure 3.5. X-ray diffraction of mesoporous TiO_2, the peak at 25.4° is consistent with the formation of anatase TiO_2. The grain size derived using Scherrer analysis is ~9 nm, in agreement with other measurements of pore size.

3.3.2 Infusion of Nanoparticles

SEM images of Pt-TiO_2 and Au-TiO_2 composites indicate that the nanoparticle dispersion and distribution through the pores is size dependent. Very little Pt is visible on the surface after immersion in toluene containing 10 mM 1.7 ± 0.4 nm diameter Pt nanoparticles, even though 26 wt. % Pt was detected using EDS (Figure 3.6). In contrast, Au nanoparticles are clearly visible on the film surface after a similar experiment was performed with 10 mM of larger 3.9 ± 0.7 nm diameter Au nanoparticles (Figure 3.6 c). Larger 6.1 ± 1.5 nm diameter Au nanoparticles did not diffuse into the film in significant quantities, instead forming micron sized islands on the film surface after sintering (Figure 3.6 d). 100 μm^2 SEM images of the nanoparticles infused films are provided in Figure 3.6 e-f. EP experiments were performed to determine the pore size and pore size distribution (PSD) throughout the mesoporous TiO_2 films and to further explore how the interplay between the tortuosity of the pores and the size of nanoparticles alters their loading and distribution throughout the mesopores.

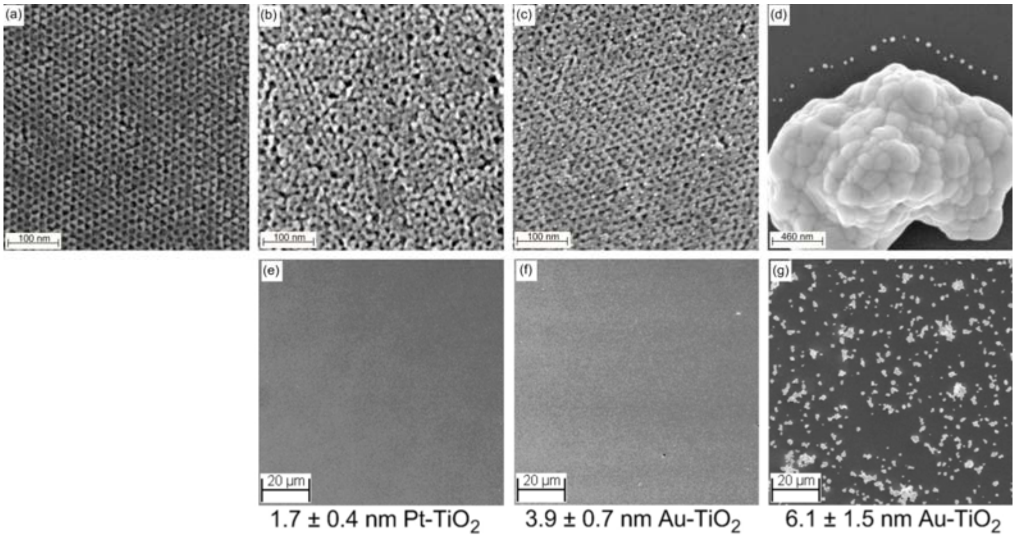

Figure 3.6. SEM images of mesoporous TiO_2 surface (a) as prepared, (b) following 1.7 ± 0.4 nm Pt nanoparticle infusion, (c) following 3.9 ± 0.7 nm Au nanoparticle infusion, and (d) surface aggregation of 6.1 ± 1.5 nm Au nanoparticles. (e-f) 100 μm x 100 μm SEM image of respective mesoporous TiO_2

3.3.3 EP of Mesoporous TiO_2

Isotherms determined for toluene, ethanol, and water adsorption on mesoporous TiO_2 are plotted for $n_{avg.}$ versus P/P_o (Figure 3.7). Isotherms measured on the same films were reproducible over the time period of months and did not change between runs. As an example two subsequent isotherms performed using water as an adsorbate are shown in figure 3.8.

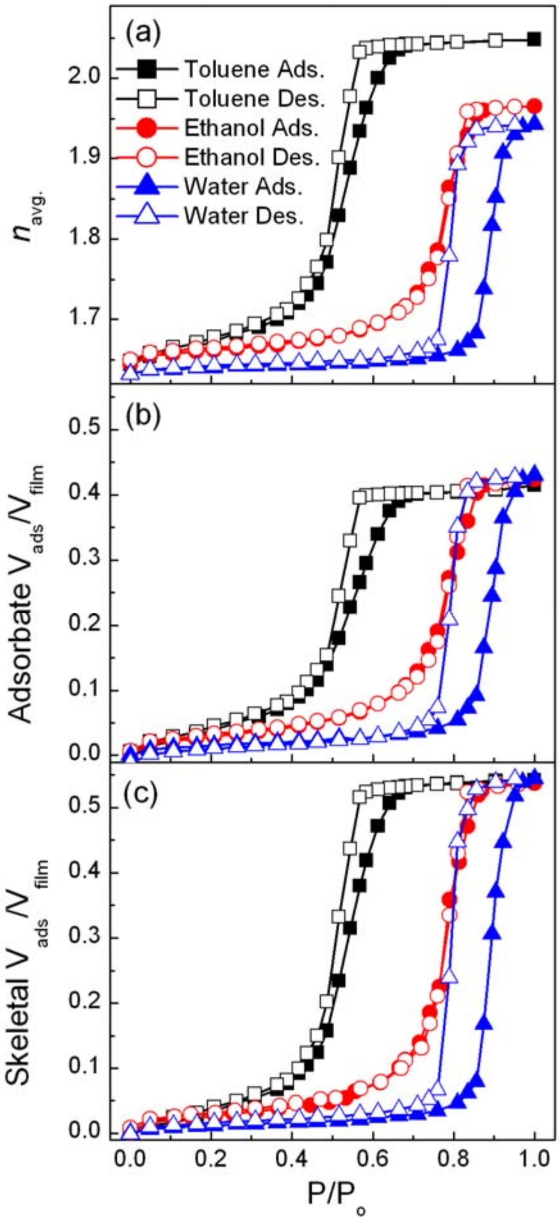

Figure 3.7. (a) Comparison of *n* versus the partial pressure of adsorbate for the adsorption (solid) and desorption (hollow) of toluene (■), ethanol (●), and water (▲) on mesoporous TiO_2. (b) Relative volume of adsorbate, derived using the adsorbate method. (c) Relative volume derived using the skeletal method.

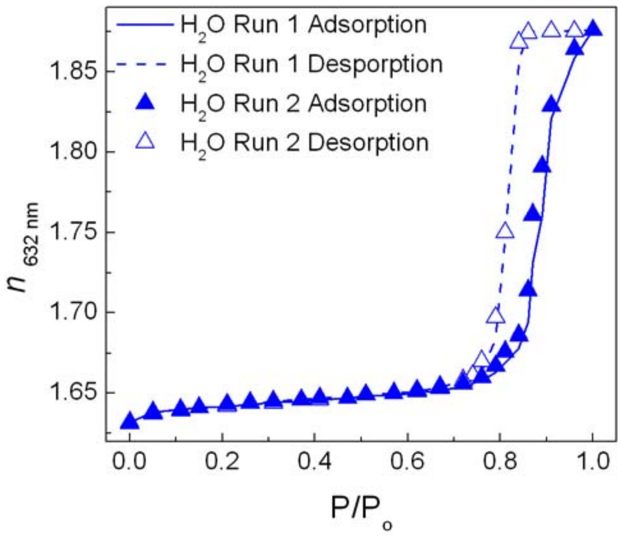

Figure 3.8. Two subsequent isotherms of H_2O adsorption and desorption on mesoporous TiO_2. Similarity between the two sets of data indicates that the structure of the film does not change significantly upon cycling.

Between samples the adsorption isotherms retained the same basic shape and features although there was some variation due to differences in the samples, as evidenced by the real refractive index of eight different films having a percent standard deviation of 5%. The three adsorbates result in very different isotherms (Figure 3.7a) which shift to larger values of P/P_o with increasing adsorbate polarity. All of the isotherms are of the type IV variety as classified by IUPAC.[39] This type of isotherm corresponds to multilayer adsorption with a hysteresis loop arising from capillary condensation in mesopores. In general, adsorption on a mesoporous material begins with monolayer and then multilayer formation across the film surface. Capillary condensation then occurs with larger and larger mesopores being filled as the partial pressure of adsorbate increases. In figure 3.7, before the onset of capillary condensation ($P/P_o < 0.4$ in toluene), the slope of the toluene isotherm is larger than ethanol or water, indicating that toluene is more readily adsorbed at lower partial pressures (Figure 3.7). Capillary condensation follows a similar pattern, with large changes in the adsorbed volume of toluene occurring well before that of ethanol or water. While these features track with adsorbate polarity, they are primarily due to the adsorbate properties and not adsorbate-TiO_2 interactions. However, analysis of the PSDs shows that isotherms performed using water are strongly shifted by interactions between the water and TiO_2 (vida infra).

3.3.4 Estimation of Surface Area and pore size distributions via EP.

Porosimetry techniques ranging from N_2 porosimetry to more recently developed techniques such as X-ray porosimetry (XRP) or small angle neutron scattering (SANS) rely on assumptions, such as the density of the adsorbate, to be made in converting the measured signal to the volume adsorbed.[26,40-42] Similarly the ellipsometry parameters Ψ and Δ are converted to n and then to a volume using a variety of techniques with different assumptions. Conversion of Ψ and Δ to n and thickness is relatively straightforward for non-adsorbing oxide thin films.[35] Here the Cauchy equation was implemented and resulted in excellent fits to Ψ and Δ. However, relating n to the volume of adsorbate is not as straightforward. Generally an effective medium approximation is used to relate the change in n to the relative volume of liquid adsorbed by the film. One set of assumptions, made in several studies[17,43,44], is that $n_{ads.}$ is constant and equal to the refractive index of the bulk adsorbate. All changes in n are attributed to the replacement of air (n=1) with $n_{ads.}$. The Lorentz-Lorenz (L-L) equation is used to find the volume adsorbed from the change in refractive index while also accounting for changes in thickness (eq. 4). Because this method assumes that $n_{ads.}$ is constant it will be referred to as the adsorbate method. As P/P_o is changed, the change in n, converted to the volume polarizability, is divided by the polarizability of the adsorbate resulting in the relative volume adsorbed.

$$V_{ads} / V_{film} = \frac{B_{p=x} t_{p=x} - B_{p=0} t_{p=0}}{B_{ads} t_{p=0}} \tag{4}$$

Where V_{ads} is the volume of adsorbate, $t_{p=x}$ is the film thickness at the P/P_o of interest, $t_{p=0}$ is the initial film thickness, $B_{p=x}$ is the volume polarizability at the P/P_o of interest, $B_{p=0}$ is the initial polarizability, and B_{ads} is the adsorbate polarizability. The B values are determined from the average n from 450 nm to 1000 nm, found by integrating the Cauchy equation and finding the mean value with, $B = (n^2 - 1)/(n^2 + 2)$. Note that eq. 4 provides a correction for the change in film thickness. The thickness of the TiO_2 films measured here would decrease by as much as 10 % during adsorption due to the large capillary forces exerted on the film by adsorption in mesopores. A representative plot showing the change in thickness during toluene adsorption is shown in Figure 3.9. Being able to account for this change in thickness is an important advantage of EP compared to other methods.

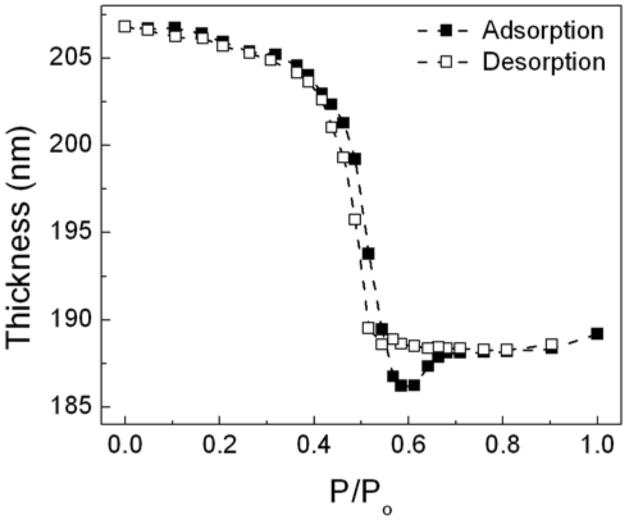

Figure 3.9. Change in film thickness with increasing P/P$_o$ of toluene. Capillary condensation exerts a force on the film causing it to shrink until the pore is completely filled and the pressure is somewhat relaxed causing thickness to increase slightly at higher P/P$_o$.

Under some conditions n_{ads} may change upon adsorption because of the effects of pore confinement. To address this shortcoming, a method, here referred to as the skeletal method, which does not require knowledge of n_{ads} was developed.[29] This method utilizes the Bruggeman effective medium approximation (BEMA) (eq. 5) which is a self consistent method for describing a material's n from the known n of its constituent parts. Here the BEMA has been applied assuming that any intermediate pore filling is described by a mixture of the optical constants of the film at $P/P_o = 0$ and at saturation.[24,29]

$$f_A \frac{n_A^2 - n^2}{n_A^2 + 2n^2} + (1 - f_A)\frac{n_B^2 - n^2}{n_B^2 + 2n^2} = 0 \tag{5}$$

Equation 4 is presented in terms of the real refractive index where n_{A} is the refractive index at $P/P_o = 0$, n_{B} is the refractive index at saturation, n is the mixed refractive index, and f_A is the fraction of film porosity that remains unfilled, which is set as a fit parameter. High correlation between thickness and f_A was observed so the thickness was fixed to values determined at each P/P_o using the Cauchy model. Using the value of f_A the volume of adsorbate relative to the volume of material was determined by multiplying the filled fraction by the porosity of the film. The film porosity was determined from a BEMA mixture of the skeletal refractive index, determined for an untemplated film $n_{632\ \mathrm{nm}} = 2.26$, and air. The advantage of this method is that n_{ads} is not used to determine the volume of adsorbate. However, it does assume that the skeletal refractive index is known, here the same as determined for a nonporous film, and that all of the porosity in the film is known, open, and fully accessible. This last assumption means that this method can not be used when nanoparticles are incorporated into the film because they may block some of the film porosity. Thus, if EP is to be used to analyze the Au-TiO_2 and Pt-TiO_2 nanocomposites, then, the assumption that n_{ads} is constant must be validated.

3.3.5 Effect of Adsorption on Adsorbate Refractive Index

To determine the deviation of n_{ads}, isotherms taken on the same sample for toluene, ethanol, and water were analyzed by the adsorbate and skeletal methods (Figure 3.7 b & c). The shape of the isotherms is generally the same between the two methods, though the adsorbate method reaches saturation at a volume fraction that is ~0.10 units lower than with the skeletal method. What is the reason for this discrepancy? One possibility is that the refractive index of the adsorbate is not the same as the bulk value. Decreasing n_{ads} by ~8 % brings the total volume determined by the adsorbate method in line with that for the skeletal method. While this appears to indicate that n_{ads} is being lowered by confinement effects, closer examination reveals that this is not the case. All three adsorbates require the same adjustment and all reach saturation at about the same volume fraction. This observation is not expected if n_{ads} is being altered by confinement effects. The refractive index of the more polar water adsorbate should change by more than the ethanol or toluene, since the surface/adsorbate interaction of water on TiO_2 is higher than that of toluene or ethanol, as evidenced by contact angle measurements on untemplated TiO_2 films (Table 3.1). This makes it relatively more difficult for water to associate on the TiO_2 surface. Thus, the fact that n_{ads} is altered by the same amount indicates that confinement effects are not dominant. We also wanted to rule out the possibility that the size difference of the adsorbate molecules could mask confinement effects. Water is a much smaller molecule than toluene, so that if there is a significant volume of micropores that are large enough to adsorb water, but not toluene, the actual volume of water adsorbed could be much higher than toluene. This phenomenon has been observed for microporous TiO_2 thin films for which significantly less toluene was adsorbed compared to water.[45] If the refractive index of the water is also reduced more than that of toluene the confinement and size effects could offset one another. To test this n-hexane, which has a smaller kinetic diameter than toluene, but is non-polar, was used as an adsorbate. The volume adsorbed was about the same for toluene and n-hexane, indicating that size based exclusion from micropores does not make a significant contribution to the optical response. The isotherm for n-hexane adsorption is given in figure 3.10

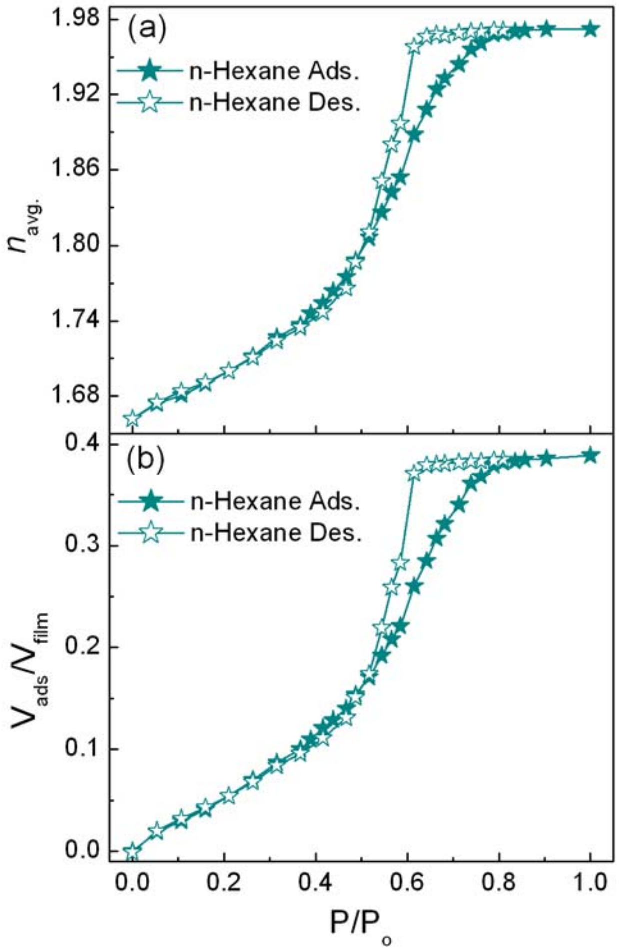

Figure 3.10. Average (a) *n* and (b) relative volume derived for the adsorption of n-hexane on mesoporous TiO_{2}. n-hexane and toluene both reach saturation at ~0.4 volume fraction.

These findings are corroborated by other studies which showed little or no effect stemming from confinement even though they were utilizing systems that should maximize the effect. In one study confinement effects were not observed for thin water layers sandwiched between hydrophobic mica[46], while in another case an extreme contrast in polarity was required to see confinement effects in thin films of cyclohexane compressed below ~3 nm.[47] Since only minimal confinement effects are observed in studies where the adsorbate and adsorbent have very different polarities (not the case here as evidenced by contact angle measurements (Table 3.1)), the assumption that n_{ads} is the same as the bulk liquid seems reasonable. Also, from an application standpoint, differences between the two methods for the determination of the BET surface area and PSDs are very small (Table 3.1 and 3.2). Thus, the restrictive skeletal method is not necessary to characterize these systems, so the adsorbate method is used for the analysis of the metal-TiO_2 nanocomposites. The origins of the different adsorbed volumes determined by the adsorbate and skeletal methods will be further discussed in terms of UV modification of the TiO_2 surface. When exposed to UV light TiO_2 catalytically removes carbon from the surface. Following this exposure the volume of adsorbate in the TiO_2 films increased, indicating that carbon contamination is obstructing some of the porosity. Thus the assumption made by the skeletal method that all of the porosity is accessible to the adsorbate appears to be invalid meaning that the porosity determined by that method is slightly overestimated.

Table 3.1. Pore Size Distribution

Adsorbate	Method	r_k Ads. (nm)	r_k Des. (nm)	θ_c (^{o})	$r_k \cos(\theta)$ Ads.	$r_k \cos(\theta)$ Des.
Toluene	Adsorbate	4.0 ± 0.7	3.6 ± 0.4	6 ± 3	4.0 ± 0.7	3.5 ± 0.4
Toluene	Skeletal	4.1 ± 0.7	3.6 ± 0.4	6 ± 3	4.1 ± 0.7	3.6 ± 0.4
Ethanol	Adsorbate	4.5 ± 1.4	4.2 ± 0.8	9 ± 5	4.4 ± 1.4	4.1 ± 0.8
Ethanol	Skeletal	4.5 ± 1.0	4.2 ± 0.9	9 ± 5	4.4 ± 1.0	4.1 ± 0.8
Water	Adsorbate	9.6 ± 2.4	4.3 ± 0.4	63 ± 4	4.3 ± 0.4	1.9 ± 0.2
Water	Skeletal	9.5 ± 1.8	4.3 ± 0.3	63 ± 4	4.3 ± 0.8	2.0 ± 0.1

Table3.2. Summary of BET analysis

Adsorbate	Method	V_m (cm^3/g)	c	σ (nm^2)	SA (m^2/g)
Toluene	Adsorbate	4.9	8.4	0.37	44
Toluene	Skeletal	4.8	5.6	0.37	43
Ethanol	Adsorbate	5.6	27.2	0.246	33
Ethanol	Skeletal	5.2	24.0	0.246	31
Water	Adsorbate	9.3	29.8	0.125	28
Water	Skeletal	7.4	22.5	0.125	22

The surface areas of mesoporous TiO_2 films were determined using eq. 2 (Table 3.2). The volume of adsorbate, ν, was determined by converting the relative volume into the volume of gas per gram of film using the adsorbates bulk liquid density, the ideal gas law, and the assumption that the mesoporous TiO_2 films had a density of ~2 g/cm^3, as estimated from porosity measurements. The BET surface area derived from the toluene isotherm shown in Figure 3.7 was 44 m^2/g, close to the value of 58 m^2/g determined by Wu[30] using traditional N_2 adsorption porosimetry. Since N_2 porosimetry requires much more material than is present on a thin film, multiple films must be scraped off of their substrate to obtain a sufficiently large sample. The surface area determined is likely to be overestimated because of additional breakage of the film into smaller, higher surface area fragments as a result of physical scraping. For EP, the surface areas derived using ethanol and water were 33 m^2/g and 28 m^2/g, respectively. The fact that these values are slightly lower than that observed for toluene is difficult to interpret because of the large errors often associated with BET surface area analysis. Specifically, for the mesoporous TiO_2 samples the c value which indicates the strength of attraction between adsorbate and adsorbent is small, indicating potentially large errors in v_m. In fact the relative standard deviation of the surface area for multiple films is ~25%. For all three adsorbates, the adsorbate and skeletal methods gave very similar values for surface area and the BET constant c (Table 3.2). This provides further evidence that deviations in the adsorbate refractive index from bulk values are not significant.

3.3.6 Determination of Pore Size Distribution

The Kelvin equation (eq. 1) was used to determine the mean pore size and pore size distribution (PSD) of the mesoporous TiO_2. The resulting PSDs are presented in Figure 3.11 for toluene (3.11 a), ethanol (3.11 b), and water (3.11 c), assuming that the contact angle of the adsorbate is 0º.

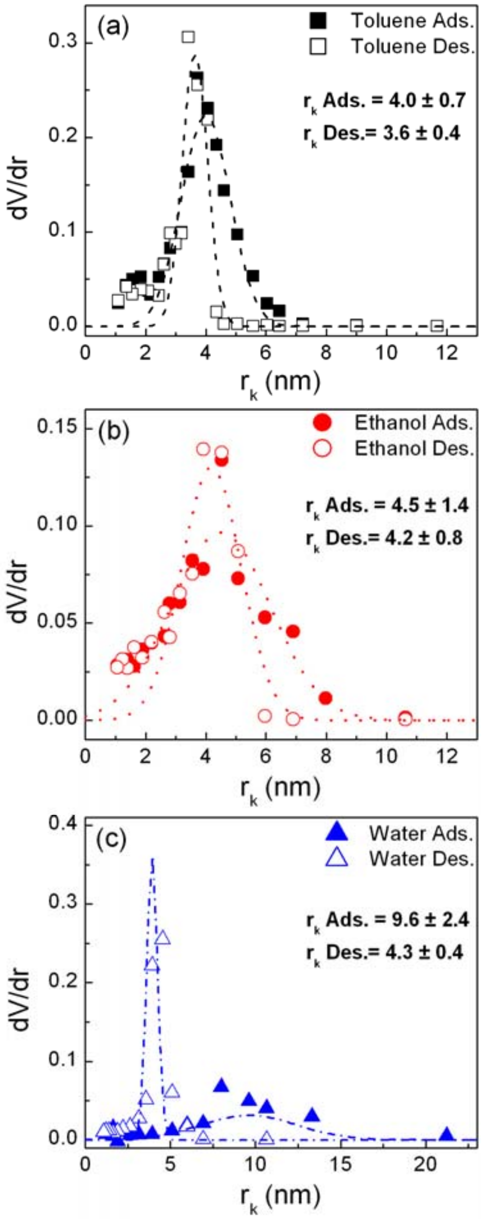

Figure 3.11. Pore size distributions derived using the Kelvin equation for cylindrical pores for (a) toluene (■), (b) ethanol (●), and (c) water (▲) adsorption (solid) and desorption (hollow) on mesoporous TiO_2. The lines represent best fit Gaussians through the displayed data points, here the contact angle is assumed to be 0°.

Adsorption of toluene and ethanol results in similar PSDs (Table 3.1). The toluene adsorption branch indicates that $r_{k,ads}$= 4.0 ± 0.7 nm. Note that the reported standard deviations for the pore size distributions are derived from Gaussian fits to the data so they indicate the spread of the pore sizes, not the measurement's precision. The PSD values are in good agreement with SEM pore diameter values of 10 ± 2 nm and ~9 nm as determined by Scherrer analysis of X-ray data.[13] The mean pore size determined by EP is expected to be slightly lower than that observed using SEM because the pore walls are not flat, instead they have a close packed geometry.[30] This tortuousity causes bottlenecks in the pores that decrease the effective pore size but are not resolved by SEM. This bottlenecking is a factor that causes $r_{k,des}$ to be consistently smaller than $r_{k,ads.}$[48,49] Additionally, the volume of adsorbate present on the walls prior to capillary condensation must be taken into account. This value can be estimated by measuring the thickness of the adsorbate layer on a nonporous sample of the skeletal material.[29] However, the mesoporous TiO_2 prepared by sol gel chemistry used in our experiments has some inherent porosity which lead to a contraction of the film below P/P_o= 0.20. To account for this adsorption, the optical constants and thickness determined at P/Po= 0.20 were held constant and used as the starting point for the isotherm. A layer consisting of the adsorbate refractive index was then placed on top of this layer with the layer thickness set as the only fit parameter. The thickness at the onset of capillary adsorption of toluene on TiO_2, 0.4 nm, brings the mean pore diameter to 8.8 ± 1.4 nm. The difficulties encountered with the untemplated sample as well as suspect results from similar experiments performed using ethanol and water necessitated the application of an alternative method. Another way to estimate the partial pressure dependent thickness of an adsorbate is the Halsey-Wheeler equation (eq. 6).[20,50,51]

$$t = \sigma\left(\frac{5}{-\ln(P/P_o)}\right)^{1/3} \tag{6}$$

$$\sigma = \frac{MW}{N_A A \rho_{liquid}} \tag{7}$$

This equation allows determination of the pre adsorbed layer thickness (t) from the thickness of a monolayer (σ) and the partial pressure (P/Po). The parameter σ can be estimated based on eq. 7 which assumes a hexagonally close packed monolayer where MW is the molecular weight of the adsorbate, N_A is Avogadro's number, A is the area of the adsorbate molecule, and ρ_{liquid} is the density of the liquid adsorbate. Obviously this method will be very sensitive to errors in the molecular area as well as variations in how the adsorbate is actually packing on the surface. Nevertheless, the method gives reasonable estimates of the preadsorbed layer thickness on the same order of magnitude as those calculated using ellipsometry. To determine the pore size distribution the t value at each P/Po was added to r_k and then fit by the same procedure as the uncorrected PSD analysis. For each adsorbate accounting for t using this method increases the measured radius by 1 nm and slightly broadens the distribution. For example the radius derived from the adsorption branch for toluene increased from 4.0 ± 0.7 nm to 5.0 ± 0.8 nm while that for water increased from 9.6 ± 2.4 nm to 10.6 ± 2.8 nm. Thus the Halsey-Wheeler equation gives a slightly larger pore diameter of 10.0 ± 1.6 nm compared to the value of 8.8 ± 1.4 nm found using ellipsometry to measure the thickness of adsorbate on an untemplated sample. Given the small difference between the two methods accuracy is difficult to asses. Certainly the Halsey-Wheeler correction matches almost exactly the SEM derived PSD of 10 ± 2 nm; however, as discussed previously the tortuosity of the pores is expected to reduce the effective diameter of the pore. Because of this ambiguity the remainder of the discussion will be focused only on comparing the derived Kelvin radius and not present data corrected by either method to reduce complications that might arise from errors in each. Effectively no less information is gleaned by doing this because changes in the film properties following UV irradiation or nanoparticle infusion are well illustrated by changes in r_k.

The PSD derived from the adsorption of water, $r_{k,ads}$= 9.6 ± 2.4 nm, is significantly shifted compared to the other adsorbates. This observation is expected because the water contact angle is much larger than that for ethanol or toluene (Table 3.2). Compensating for the contact angle shifts the mean water r_k value for the adsorption branch from $r_{k,ads}$= 9.6 ± 2.4 nm to $r_{k,ads}$= 4.3 ± 0.4 nm, a value more in line with the contact angle corrected measurements for toluene, $r_{k,ads}$=4.0 ± 0.7 nm, and ethanol, $r_{k,ads}$=4.5 ± 1.4 nm. However, the same contact angle adjustment performed on the water desorption branch results in a smaller than expected value, $r_{k,des}$= 1.9 ± 0.2 nm. In a similar study of EP experiments of water being adsorbed on Si a shift of similar magnitude was observed.[28] The authors surmised that the difference between r_k determined for adsorption and desorption was due to the adsorption curve reporting on pore size, whereas the desorption curve was reporting on bottlenecking and pore interconnects.[28] However, this does not explain the large difference observed for the water isotherms as the toluene and ethanol isotherms do not exhibit this behavior. These results indicate that the gap in the mean pore size between the adsorption and desorption branches of water is dominated by adsorbate-TiO_2 interactions.

The large shift in the PSD seen for water relative to ethanol and toluene indicates that the difficulty of water wetting the TiO_2 surface (larger contact angle in Table 3.1) delays adsorption to higher P/P_o values (Figure 3.7). Note also that the uptake of water into the TiO_2 occurs much more abruptly for water than toluene or ethanol, which is additional evidence that adsorption is being delayed by an energy barrier. This barrier arises from the difficulty of fully coating the wall with a monolayer of water. Once this layer is completed, a “plug” of water can condense into the pores because the presented surface is now the water monolayer instead of the TiO_2 surface. Upon desorption this energy barrier is not present as the TiO_2 has been already wetted and desorption is governed by the capillary forces described by the Kelvin equation.

3.3.7 UV Modification of the TiO_2 Surface

Further support for the assertion that water adsorption is delayed by the TiO_2 surface energy is provided by irradiating the TiO_2 film with UV light prior to EP experiments. Irradiation of TiO_2 with UV light below its band gap is known to induce the formation of hydroxyl defects on the surface, greatly increasing the hydrophilicity of TiO_2.[52] For example, the contact angle of water on untemplated TiO_2 decreases from 63° ± 4° to 10° ± 2° following one hour of irradiation from a 400 W Hg lamp. This effect is advantageous because the surface properties of the TiO_2 can be modulated with negligible effect on the size of the mesopores. For analysis of the isotherms this means that adsorbate property based effects can be separated from adsorbate-TiO_2 interactions. To illustrate this effect and to better describe the effect of adsorbate polarity on the pore size distribution isotherms using both toluene and water before and after sample irradiation for one hour under a 400 W Hg lamp will be compared (Figure 3.12).

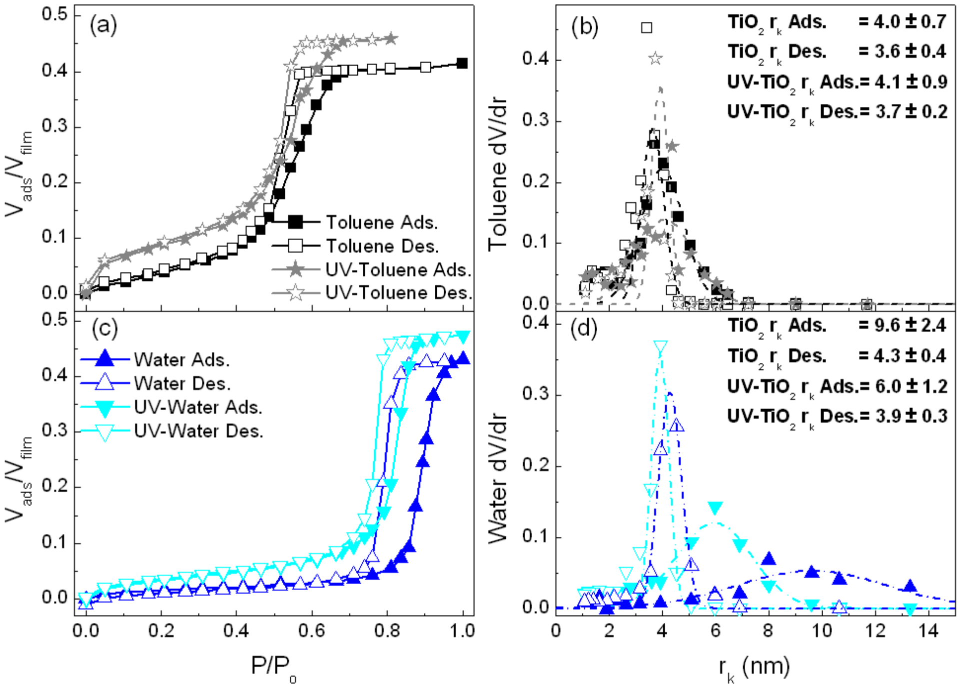

Figure 3.12. Adsorption (solid) and desorption (hollow) isotherms for (a) toluene (■,★), and (c) water (▲,▼) on a mesoporous TiO_2 film before and after UV irradiation. (b and d) The resulting pore size distribution assuming a contact angle of 0°.

The shape and position of the hysteresis loop of the toluene isotherms are nearly identical before and after UV irradiation (Figure 3.12 a), as are the resulting PSDs (Figure 3.12 b). This observation is expected, as the toluene contact angle on dense TiO_2 does not change by a significant amount, 6° ± 3° before irradiation and 10° ± 2° following UV irradiation. The only major difference in the toluene isotherms is that following irradiation *n* increases by a much larger amount between $P/P_o = 0$ and $P/P_o = 0.05$. Adsorption in this region is generally attributed either to adsorption in micropores or layered adsorption on the film surface prior to capillary condensation in mesopores. Since the toluene contact angle remains low and constant, an enhancement in the amount of multilayer adsorption of toluene at low partial pressures is unlikely. Thus, the jump in adsorption is attributed to a small increase in the accessible microporosity of the film following UV irradiation. TiO_2 irradiated by UV light is known to decompose organic material[53], and the change in volume adsorbed is attributed to the removal of surface contaminants, i.e. carbon, from the TiO_2 surface. Interestingly, isotherms of the same film taken on subsequent days again behaved as they did prior to irradiation. This indicates that the change in adsorbed volume arises from the removal of surface contamination that occurs in open air and not from the removal of residual surfactant template. The presence of blocked micropores is also likely to contribute to the lower adsorption volume calculated by the adsorbate method compared to the skeletal method. The skeletal model assumes that these pores are open, while the adsorbate method does not make a priori assumptions about porosity, so that in this case the adsorbate method gives a more complete picture of the pore structure.

In contrast to the relatively minor effect of UV irradiation on the toluene isotherms, the isotherms obtained for water adsorbate show dramatic changes (Figure 3.12 c). Prior to capillary condensation adsorption increases more rapidly after irradiation and capillary condensation occurs at lower P/P_o with a significantly reduced hysteresis loop. Similar to the toluene isotherms, the volume adsorbed also increases slightly. These differences lead to a dramatic shift in the derived PSD (Figure 3.12 d). The Kelvin radius for the adsorption branch, not corrected for contact angle, decreases from $r_{k,ads} = 9.6$ nm ± 2.4 nm to $r_{k,ads} = 6.0$ nm ± 1.2 nm. The reason for this change is that the TiO_2 surface has become more hydrophilic. $r_{k,ads}$ does not decrease all the way to the ~4 nm indicated by toluene and ethanol adsorption. This implies that the flux of UV light through the film was insufficient to decrease the contact angle of water to the 10° ± 2° observed for the untemplated films. The contact angle of water adsorbed in the mesopores can be estimated using the Kelvin equation by assuming that r_k= 4 nm. This analysis results in an estimated contact angle of ~66° prior to UV irradiation, a value in good agreement with measurements taken on an untemplated film of 63° ± 4°. After UV treatment a mean water contact angle of 48° is estimated from the Kelvin equation for the UV irradiated film, lower than the 66° estimated prior to UV treatment, but much higher than the 10° ± 2° found for untemplated

TiO_2 following irradiation again consistent with incomplete conversion of the mesoporous TiO_2.

Following UV irradiation of surfactant templated TiO_2, the Kelvin radius of the adsorption branch decreases by 3.6 nm while the Kelvin radius of the desorption branch decreases by only 0.4 nm. Thus, the adsorption branch is more sensitive to changes in the TiO_2 surface chemistry, while the desorption branch is dominated by capillary forces. This is consistent with the behavior of the unirradiated TiO_2 film during water adsorption for which the adsorption branch was significantly shifted compared to the desorption branch. Humidity induced hydroxyl defects were ruled out as the cause of the difference in $r_{k,ads}$ and $r_{k,des}$ because theoretical[54] and experimental[55] studies show that the adsorption of water on anatase TiO_2 is much more energetically favorable than dissociation. Also, repeated cycling between P/P_o= 0.70 and P/P_o= 1 did not result in changes to the isotherm, a shift to lower P/P_o would be expected if additional hydroxyl defects were induced by high humidity environment, promoting more favorable water adsorption.

3.3.8 Ellipsometric Porosimetry of Au- and Pt-TiO_2 Composite Films

Toluene isotherms before and after nanoparticle infusion were acquired to characterize the distribution of Pt and Au nanoparticles loaded into the mesoporous TiO_2. The Pt-TiO_2 composite was modeled in the same way as the mesoporous TiO_2 films. The Cauchy equation was used to determine *n* and thickness from 450 nm to 1000 nm and then this data was converted to a relative volume of adsorbate using the adsorbate method.

Unlike Au, the Pt plasmon adsorption is located in the ultraviolet portion of the spectrum, and the Pt nanoparticles did not absorb enough light to interfere with the assumption that k = 0 from 450 nm to 1000 nm. Representative isotherms are presented in Figure 3.13 a for a mesoporous TiO_2 film before and after Pt infusion.

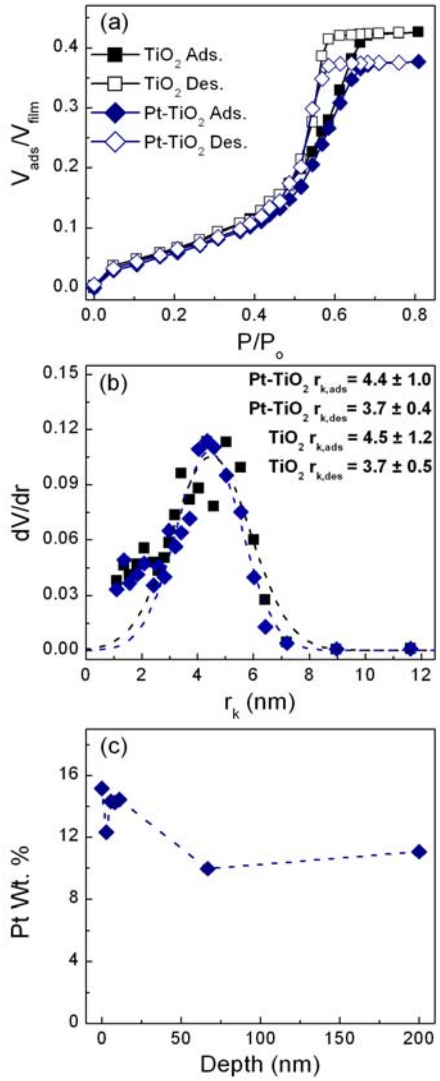

Figure 3.13. (a) Toluene adsorption (solid) and desorption (hollow) isotherms before (■) and after (♦) the infusion of 1.7 ± 0.4 nm Pt nanoparticles (~26 wt. %) into mesoporous TiO_2. (b) Pore size distribution derived from the adsorption of toluene (c) Plot of Pt wt. % versus sputtering depth as derived by XPS analysis of the Pt4f band.

The Pt-TiO_2 film was determined by EDS to contain 26 wt. % Pt. Prior to capillary condensation the volume of adsorbate increases at about the same rate before and after Pt infusion and both have BET surface areas that differ by less than 3 %. As capillary condensation begins less toluene is adsorbed into the Pt loaded film which becomes saturated at 0.04 volume fraction lower than prior to Pt infusion. The volume fraction of Pt particles is estimated from the EDS derived value of 26 wt. % to be ~3 vol. %, assuming spherical particles and bulk Pt density. Thus, the decrease in film volume is accounted for by the volume of the nanoparticles with little of the film's porosity being obstructed. The PSD remains basically unchanged following infusion with both isotherms having a mean Kelvin radius of 4.1 nm (Figure 3.13 b). This data indicates that the Pt nanoparticles are distributed evenly among the various sized pores and are not restricting the pores enough to change r_k. This finding is consistent with SEM images (Figure 3.6 b) that showed very few particles on the surface as well as XPS depth profiling analysis which shows that the Pt particles are evenly distributed throughout the thickness of the film (Figure 3.13 c). This sample is also interesting because, as seen in Figure 3.6 b, it is more disordered than the other films and contains a significant population of pores around 4 nm in diameter (Figure 3.13 b). This is notable because, according to the Kelvin equation, this size range is represented by partial pressures of toluene below ~ $P/P_o = 0.40$. In this region, the difference between the isotherms with and without Pt is small, implying that the 1.7 ± 0.4 nm Pt particles do not diffuse into pores smaller than 4 nm in diameter. Not until the pore size is more than double the mean TEM measured particle size does the adsorbed volume decrease indicating Pt loading. This size effect is further supported by the loading of Au particles for which 21 wt. % loading was achieved for 3.9 ± 0.7 nm diameter particles, while almost no loading/uptake is observed for 6.1 ± 1.5 nm diameter Au particles, whose size is greater than 50% of the mean pore size.

Converting Ψ and Δ into *n*, *k*, and thickness is considerably more difficult for films infused with Au than Pt. The clustering and alignment of Au nanoparticles within in the pores leads to anisotropy of the optical constants as free electron adsorption is enhanced perpendicular to the substrate[13]. Further complications arise because the Au plasmon in the visible portion of the spectrum is responsive to the environment of the nanoparticles and changes as the amount of adsorbate increases. Several different models were attempted to extract changes in volume and thickness from the SE data, but they suffered from high parameter correlation or unrealistic results. However, the PSD is determined using the relative change in volume and any signal proportional to the volume adsorbed should suffice. In another work, the ellipsometry parameter Δ was shown to be proportional to the volume of water adsorbed on SiO_2.[56] To determine if this proportionality held in this instance both Ψ and Δ, determined during toluene adsorption on mesoporous TiO_2, were plotted against the volume adsorbed for a variety of wavelengths at an angle of incidence of 70°. In doing this it was observed that the linearity of Ψ and Δ with volume was highly wavelength dependent and that often Ψ or

Δ would exhibit a different relationship to volume depending on the wavelength. Therefore this analysis should be considered largely empirical and the relationship between Ψ, Δ, and volume should be independently verified for different materials and circumstances. At 1000 nm both Ψ and Δ for the adsorption of toluene on templated TiO_2 had similar relationships with volume and exhibited excellent linearity through P/P_o=0.3 (Figure 3.14 a).

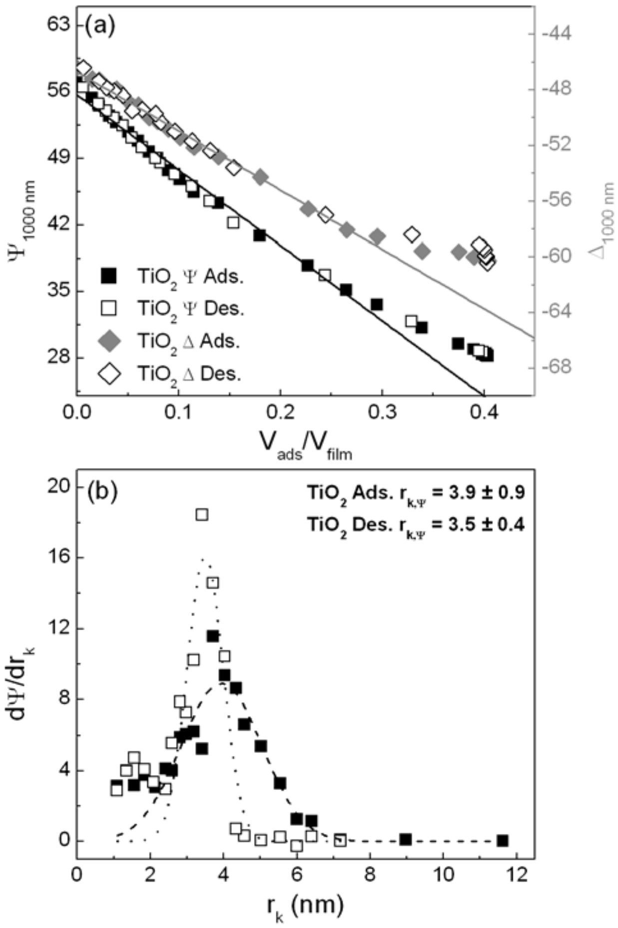

Figure 3.14. (a) Comparison of Ψ (■) and Δ (♦) versus the volume of adsorbate derived from n which was obtained using the Cauchy equation to fit ellipsometric data from 450 nm to 1000 nm. At 1000 nm both Ψ and Δ are proportional to the volume adsorbed up to V_{ads}/V_{film}= 0.3. This range is sufficient to obtain pore size distributions (b) that are almost identical to the adsorbate method.

This range was enough to derive an accurate PSD. A plot of $d\tilde{\Psi}dr_k$ vs. r_k revealed a mean pore size within 0.1 nm of that found using the adsorbate method for both the adsorption and desorption branch (Figure 3.14 b). Therefore Ψ at 1000 nm was used to monitor the adsorption of toluene on Au-TiO_2 (Figure 3.15). Obviously, this analysis relies on the assumption that the Au nanoparticles do not disrupt the relationship between Ψ and volume. The overall change in Ψ following Au infusion is very much attenuated compared to the mesoporous TiO_2 indicating the occlusion of a significant amount of pore volume (Figure 3.15 a). Additionally, r_k decreases by 0.3 and 0.4 nm for the adsorption and desorption branches respectively and the distribution of pores is significantly widened for the adsorption branch (Figure 3.15 b). Both these observations are consistent with the 3.9 ± 0.7 nm Au nanoparticles blocking significant amounts of the pore structure and lowering the effective size of the pores upon loading. XPS depth profiling experiments show that the concentration of Au nanoparticles is higher at the top of the film (Figure 3.15 c).

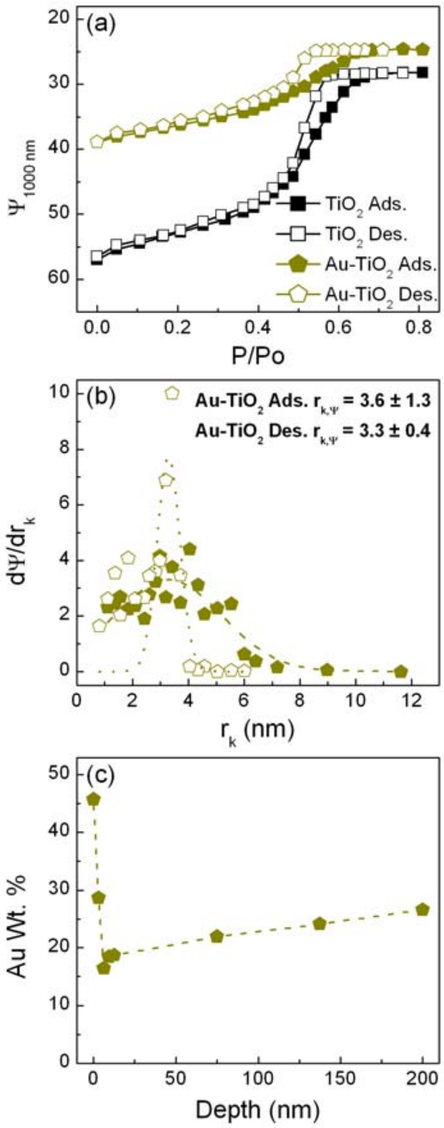

Figure 3.15. (a) Toluene adsorption (solid) and desorption (hollow) isotherms before (■) and after (⬟) the infusion of 3.9 ± 0.7 nm Au nanoparticles (~21 wt. %) into mesoporous TiO_2. (b) Pore size distribution derived from the adsorption of toluene (c) Plot of Au wt. % versus sputtering depth as derived by XPS analysis of the Au4f band.

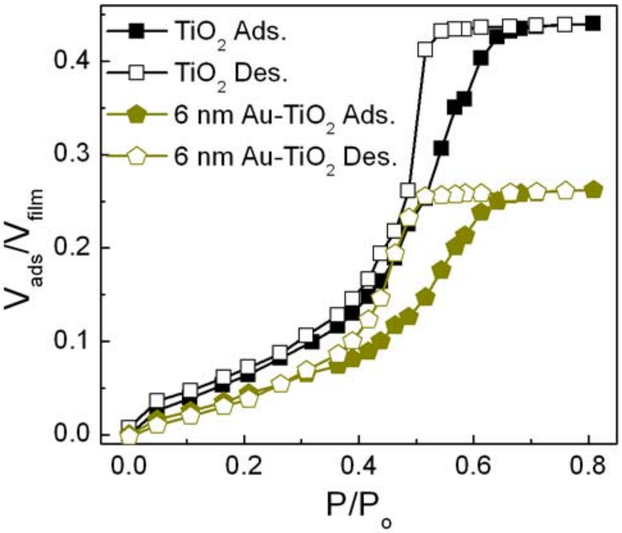

Figure 3.16. Toluene adsorption (solid) and desorption (hollow) isotherms before (■) and after (⬟) the attempted infusion of 6.1 ± 1.5 nm Au nanoparticles. The nanoparticles did not diffuse into the mesopores in large quantities instead they aggregated on the surface following heat treatment at 110°C.

This data, combined with the PSD data, indicates that the Au is small enough to diffuse into the pores, but is large enough to cause significant clogging in the pores which is not observed with the 1.7 ± 0.4 nm diameter Pt particles. Larger, 6.1 ± 1.5 nm diameter Au particles exhibited almost no diffusion into the pores, instead they agglomerated on the surface blocking 40 % of the pore volume (Figure 3.16). The volume adsorbed in Figure 3.16 was calculated using the adsorbate method with a Cauchy model proving a good fit to the SE data. Application of this method was possible because the micron sized Au islands scattered incident light and were not detected. The analysis is thus analogous to that performed on the Pt-TiO_2 composites. In aggregate this data indicates that for loading of metal nanoparticles into mesoporous TiO_2, particles with a mean diameter ~1/5, again not taking into account the organic capping ligands, of the pore diameter are easily able to diffuse throughout the film with minimal pore blockage while particles with a mean diameter ~1/2 of the pore diameter block pores and serve as a barrier to further loading. Once the mean particle diameter exceeds ~1/2 of the pore diameter almost no loading occurs. Following sintering, these larger particles agglomerate as they would on a smooth surface, no longer being restricted by the film porous structure.

3.4 CONCLUSION

Mesoporous TiO_2 thin films have been characterized by ellipsometric porosimetry and the mean pore sizes were 9 to 10 nm depending on the adsorbate and how the preadsorbed layer thickness was calculated. The BET surface area was the proper order of magnitude when compared to other samples indicating that the method can be applied to ellipsometric porosimetry even though in this case the low c values greatly increased the error. 26 wt. % of 1.7 ± 0.4 nm diameter Pt and 21 wt. % of 3.9 ± 0.7 nm diameter Au nanoparticles could diffuse into the films with the size of the nanoparticle having a substantial effect on nanoparticle distribution through the columnar mesopores. Confinement effects on the refractive index of the adsorbate, n_{ads} were negligible allowing for the use of the adsorbate method to convert n to volume adsorbed. Consequently, Pt infused TiO_2 films could be modeled applying the same methods used for TiO_2 films without nanoparticles. Since this method was not possible for Au-TiO_2 composites, given complications from anisotropy and a significant visible surface plasmon resonance, the PSD was determined directly from the ellipsometric parameters Ψ and Δ. EP data combined with SEM and XPS were used to determine the optimal size ratios for nanoparticle diffusion into mesoporous TiO_2 films to achieve high loadings, without limitation from significant pore blockage.

3.5 REFERENCES

(1) Auten, B. J.; Lang, H.; Chandler, B. D. *Appl. Catal., B* **2008**, *81*, 225-235.

(2) Thimsen, E.; Rastgar, N.; Biswas, P. *J. Phys. Chem. C* **2008**, *112*, 4134-4140.

(3) Kavan, L.; Prochazka, J.; Spitler, T. M.; Kalbac, M.; Zukalova, M.; Drezen, T.; Gratzel, M. *J. Electrochem. Soc.* **2003**, *150*, A1000-A1007.

(4) Chou, T. P.; Zhang, Q.; Russo, B.; Fryxell, G. E.; Cao, G. *J. Phys. Chem. C* **2007**, *111*, 6296-6302.

(5) Long, C. G.; Gilbertson, J. D.; Vijayaraghavan, G.; Stevenson, K. J.; Pursell, C. J.; Chandler, B. D. *J. Am. Chem. Soc.* **2008**, *130*, 10103-10115.

(6) Deki, S.; Ko, H. Y. Y.; Fujita, T.; Akamatsu, K.; Mizuhata, M.; Kajinami, A. *Eur. Phys. J. D* **2001**, *16*, 325-328.

(7) Zhao, G.; Kozuka, H.; Yoko, T. *Sol. Energy Mater. Sol. Cells* **1997**, *46*, 219-231.

(8) Sasaki, T.; Koshizaki, N.; Yoon, J.-W.; Yamada, S.; Koinuma, M.; Noguchi, M.; Matsumoto, Y. *Electrochemistry (Tokyo, Jpn.)* **2004**, *72*, 443-445.

(9) Okumura, M.; Nakamura, S.; Tsubota, S.; Nakamura, T.; Azuma, M.; Haruta, M. *Catal. Lett.* **1998**, *51*, 53-58.

(10) Allmond, C. E.; Oleshko, V. P.; Howe, J. M.; Fitz-Gerald, J. M. *Appl. Phys. A: Mater. Sci. Process.* **2006**, *82*, 675-678.

(11) Gupta, G.; Shah, P. S.; Zhang, X.; Saunders, A. E.; Korgel, B. A.; Johnston, K. P. *Chem. Mater.* **2005**, *17*, 6728-6738.

(12) Rioux, R. M.; Song, H.; Hoefelmeyer, J. D.; Yang, P.; Somorjai, G. A. *J. Phys. Chem. B* **2005**, *109*, 2192-2202.

(13) Patel, M. N.; Williams, R. D.; May, R. A.; Uchida, H.; Stevenson, K. J.; Johnston, K. P. *Chem. Mater.* **2008**, *20*, 6029-6040.

(14) Gupta, G.; Patel, M. N.; Ferrer, D.; Heitsch, A. T.; Korgel, B. A.; Jose-Yacaman, M.; Johnston, K. P. *Chem. Mater.* **2008**, *20*, 5005-5015.

(15) Zhang, Q.; Xu, T.; Butterfield, D.; Misner, M. J.; Ryu, D. Y.; Emrick, T.; Russell, T. P. *Nano Lett.* **2005**, *5*, 357-361.

(16) Gondran, C. F. H.; Michelson, D. K. *J. Vac. Sci. Technol., A* **2006**, *24*, 1185-1190.

(17) Baklanov, M. R.; Mogilnikov, K. P.; Polovinkin, V. G.; Dultsev, F. N. *J. Vac. Sci. Technol., B* **2000**, *18*, 1385-1391.

(18) Glaves, C. L.; Frye, G. C.; Smith, D. M.; Brinker, C. J.; Datye, A.; Ricco, A. J.; Martin, S. J. *Langmuir* **1989**, *5*, 459-66.

(19) Perez, G. P.; Yelton, W. G.; Cernosek, R. W.; Simonson, R. J.; Crooks, R. M. *Anal. Chem.* **2003**, *75*, 3625-3630.

(20) Borras, A.; Yanguas-Gil, A.; Barranco, A.; Cotrino, J.; Gonzalez-Elipe, A. R. *Phys. Rev. B: Condens. Matter Mater. Phys.* **2007**, *76*, 235303/1-235303/8.

(21) Alvarez-Herrero, A.; Ramos, G.; Del Monte, F.; Bernabeu, E.; Levy, D. *Thin Solid Films* **2004**, *455-456*, 356-360.

(22) Castro, Y.; Julian, B.; Boissiere, C.; Viana, B.; Amenitsch, H.; Grosso, D.; Sanchez, C. *Nanotechnology* **2007**, *18*, 055705/1-055705/7.

(23) Castro, Y.; Julian-Lopez, B.; Boissiere, C.; Viana, B.; Grosso, D.; Sanchez, C. *Microporous Mesoporous Mater.* **2007**, *103*, 273-279.

(24) Wongmanerod, C.; Zangooie, S.; Arwin, H. *Appl. Surf. Sci.* **2001**, *172*, 117-125.

(25) Jousseaume, V.; Rolland, G.; Babonneau, D.; Simon, J. P. *Appl. Surf. Sci.* **2007**, *254*, 473-479.

(26) Vogt, B. D.; Pai, R. A.; Lee, H.-J.; Hedden, R. C.; Soles, C. L.; Wu, W.-L.; Lin, E. K.; Bauer, B. J.; Watkins, J. J. *Chem. Mater.* **2005**, *17*, 1398-1408.

(27) Eslava, S.; Baklanov, M. R.; Kirschhock, C. E. A.; Iacopi, F.; Aldea, S.; Maex, K.; Martens, J. A. *Langmuir* **2007**, *23*, 12811-12816.

(28) Bass, J. D.; Grosso, D.; Boissiere, C.; Belamie, E.; Coradin, T.; Sanchez, C. *Chem. Mater.* **2007**, *19*, 4349-4356.

(29) Boissiere, C.; Grosso, D.; Lepoutre, S.; Nicole, L.; Bruneau, A. B.; Sanchez, C. *Langmuir* **2005**, *21*, 12362-12371.

(30) Wu, C.-W.; Ohsuna, T.; Kuwabara, M.; Kuroda, K. *J. Am. Chem. Soc.* **2006**, *128*, 4544-4545.

(31) Wikander, K.; Petit, C.; Holmberg, K.; Pileni, M.-P. *Langmuir* **2006**, *22*, 4863-4868.

(32) Brust, M.; Fink, J.; Bethell, D.; Schiffrin, D. J.; Kiely, C. *J. Chem. Soc., Chem. Commun.* **1995**, 1655-6.

(33) Brust, M.; Walker, M.; Bethell, D.; Schiffrin, D. J.; Whyman, R. *J. Chem. Soc., Chem. Commun.* **1994**, 801-2.

(34) Fink, J.; Kiely, C. J.; Bethell, D.; Schiffrin, D. J. *Chem. Mater.* **1998**, *10*, 922-926.

(35) Tompkins, H. G.; McGahan, W. A. *Spectroscopic Ellipsometry and Reflectometry*; Wiley-Interscience, 1999.

(36) Haynes, J. M. *Materials and Structures* **1973**, *6*, 209-213.

(37) *CRC Handbook of Chemistry and Physics*; 88 ed.; Lide, D. R., Ed., 2008.

(38) Brunauer, S.; Emmett, P. H.; Teller, E. *J. Am. Chem. Soc.* **1938**, *60*, 309-19.

(39) Sing, K. S. W.; Everett, D. H.; Haul, R. A. W.; Moscou, L.; Pierotti, R. A.; Rouquerol, J.; Siemieniewska, T. *Pure Appl. Chem.* **1985**, *57*, 603-19.

(40) Klotz, M.; Rouessac, V.; Rebiscoul, D.; Ayral, A.; van der Lee, A. *Thin Solid Films* **2005**, *495*, 214-218.

(41) Lee, H.-J.; Soles, C. L.; Kang, S.; Ro, H. W.; Lin, E. K.; Wu, W.-l. *AIP Conf. Proc.* **2007**, *931*, 209-215.

(42) Ravikovitch, P. I.; Vishnyakov, A.; Neimark, A. V.; Carrott, M. M. L. R.; Russo, P. A.; Carrott, P. J. *Langmuir* **2006**, *22*, 513-516.

(43) Baklanov, M. R.; Vasil'eva, L. L.; Gavrilova, T. A.; Dul'tsev, F. N.; Mogil'nikov, K. P.; Nenasheva, L. A. *Thin Solid Films* **1989**, *171*, 43-52.

(44) Revol, P.; Perret, D.; Bertin, F.; Fusalba, F.; Rouessac, V.; Chabli, A.; Passemard, G.; Ayral, A. *J. Porous Mater.* **2005**, *12*, 113-121.

(45) Borras, A.; Sanchez-Valencia, J. R.; Garrido-Molinero, J.; Barranco, A.; Gonzalez-Elipe, A. R. *Microporous Mesoporous Mater.* **2009**, *118*, 314-324.

(46) Kekicheff, P.; Spalla, O. *Langmuir* **1994**, *10*, 1584-91.

(47) Heuberger, M.; Zach, M.; Spencer, N. D. *Science* **2001**, *292*, 905-908.

(48) Kruk, M.; Jaroniec, M.; Sayari, A. *Langmuir* **1997**, *13*, 6267-6273.

(49) Groen, J. C.; Peffer, L. A. A.; Perez-Ramirez, J. *Microporous Mesoporous Materials* **2003**, *60*, 1-17.

(50) Gregg, S. J.; Sing, K. S. W. *Adsorption, Surface Area and Porosity. 2nd Ed*, 1982.

(51) Ogura, S.; MacLeod, H. A. *Thin Solid Films* **1976**, *34*, 371-5.

(52) Liu, K.; Zhang, M.; Zhou, W.; Li, L.; Wang, J.; Fu, H. *Nanotechnology* **2005**, *16*, 3006-3011.

(53) Mor, G. K.; Varghese, O. K.; Paulose, M.; Shankar, K.; Grimes, C. A. *Sol. Energy Mater. Sol. Cells* **2006**, *90*, 2011-2075.

(54) Stefanovich, E. V.; Truong, T. N. *Chem. Phys. Lett.* **1999**, *299*, 623-629.

(55) Henderson, M. A. *Langmuir* **1996**, *12*, 5093-5098.

(56) Zangooie, S.; Bjorklund, R.; Arwin, H. *J. Electrochem. Soc.* **1997**, *144*, 4027-4035.

CHAPTER 4

Hybrid QCM and Ellipsometric Porosimetry of Mesoporous TiO_2 and TiC‡

4.1 INTRODUCTION

As nanoscale structures transition from the laboratory to applications including catalysis, electronics, solar power generation, and anti-reflective coatings, it is indispensable to develop methods for characterizing their unique properties across very long length scales. Traditional nanocharacterization techniques like atomic force microscopy (AFM) and scanning electron microscopy (SEM) are impractical for studying large areas because of their limited spot size. Whereas macroscale techniques such as optical microscopy or traditional adsorption porosimetry suffer from either too low a resolution to adequately characterize the nanostructure of the material or too low a sensitivity to detect changes in the low masses often inherent in such materials. Ellipsometric porosimetry (EP, described in Chapter 3) is very useful for the characterization of porous thin films and has found industrial use for characterizing porous low *k* dielectrics for semiconductor applications.[1] In EP various partial pressures of an adsorbate are introduced

---

‡ Portions of this chapter were published in Flaherty, D.W.; May, R. A.; Berglund, S.P.; Stevenson, K.J.; Mullins, C. B.; *Chem. Mater.* **2009**.

to a sample and then an ellipsometer is used to, hopefully, derive the refractive index and thickness of the sample. Ellipsometry has many advantages for detecting adsorption in thin films including fast acquisition times, adjustable spot size (nominally on the order of 1 mm^2 but it can be focused down) with the ability to map many square centimeters of a wafer surface; additionally, ellipsometry can be performed on any specularly reflecting substrate and is nondestructive.[2] One limitation of ellipsometry is that for optically complex (light absorbing, scattering, or anisotropic) samples conversion of the measured parameters Ψ and Δ to a reliable n, k and thickness is tenuous at best and impossible at worst. Also, taking the measured refractive index and converting it to the volume adsorbed involves assumptions about the refractive index of the adsorbate or the material and either assumption may be unreliable. In addition, effective medium approximations, used to convert n to volume, can give very different results with no clear indicator of which result is the most accurate. We have taken two steps to address these issues. First, we have coupled measurements of optical properties using ellipsometry with measurements of the mass uptake using the quartz crystal microbalance (QCM) technique. QCM is a gravimetric technique that monitors the dampening in frequency of the vibrations of a quartz crystal upon the addition of adsorbate and is sensitive on the nanogram scale. It provides another, more direct measure of mass uptake.[3] Second, in order to address the issue of optically complex samples more advanced polarization measurements are needed. Termed generalized ellipsometry, this technique can measure the complete Mueller matrix of the sample. The Mueller matrix is then used to determine the optical constants of anisotropic or depolarizing samples such as the TiC and TiO_2 discussed in this chapter.

Reactive ballistic deposition (RBD) has been utilized to deposit TiC and TiO_2 films directly on QCM crystals, providing control of the film's morphology, surface area and porous architecture.[4-6] In this ballistic or "*hit and stick*" deposition schemes, porous films of high surface area are prepared by deposition at oblique angles.[7] Topographically elevated points, created stochastically, preferentially intercept incoming atoms while shadowing lower regions.[8] This *self-shadowing* growth process results in nanostructured films with porosity and morphology determined by the angle of deposition.[9,10] In the RBD scheme, the metal is deposited in a reactive gas, greatly extending the number of materials that can be synthesized including metal oxides[5,11] and carbides.[6] For example, we have deposited polycrystalline TiC using physical vapor deposition of titanium metal in a gaseous ethylene ambient at 35 °C. Unlike other TiC deposition schemes, the optical constants, morphology, surface area, porosity, and pore size distribution can be controlled. Transition metal carbides (TMCs) have attracted significant interest for a number of applications due to intrinsic material properties such as excellent thermal and chemical stability, high hardness, wear and corrosion resistance, and electrical conductivity.[12,13] Hybrid QCM and ellipsometric porosimetry, utilizing an isotropic approximation for TiC, is used to determine the porosity, pore size distribution, and refractive index dependence of TiC on deposition angle. Generalized ellipsometry is then used to determine how the three principle refractive indices of TiO_2 change with the adsorption of toluene. Generalized ellipsometry improves upon the QCM/EP performed on TiC by accounting for the film ansiotropy and through the direct conversion of the refractive index to the volume of toluene adsorbed. The reason that TiO_2 is utilized here is that conversion to volume was not possible with TiC because it absorbs light across the instruments' wavelength range (200 nm to 1000 nm). Since TiO_2 is transparent in the visible to near IR, it can be analyzed using optical models with fewer parameters and the subsequent changes in n can be directly converted to the volume adsorbed using the Lorentz-Lorenz equation. The anisotropy of the TiO_2 samples is very sensitive to the adsorption of toluene with the fast axis, n_2, showing the greatest sensitivity to toluene.

4.2 EXPERIMENTAL

4.2.1 Synthesis of TiC Films

Titanium carbide films were deposited using the reactive ballistic deposition scheme.[6] Briefly, the films were synthesized in a high vacuum chamber equipped with electron beam evaporators (Omicron EFM3), an *x-y-z* sample manipulator mounted upon a rotary seal, two quartz crystal microbalances (RQCM, Inficon/Maxtek Inc.), a residual gas analyzer

(Stanford Research Systems, RGA 200), and a custom built rotatable sample holder for the QCM crystals. The chamber base pressure was typically ~ 7 × 10^{-9} mbar. The electron beam evaporator was used to deposit metallic titanium onto Si(100) substrates or QCM crystals held at 35 °C in an ethylene atmosphere of ~ 2.5 × 10^{-7} mbar. Following deposition, the TiC films were passivated in low pressure (6 × 10^{-5} mbar) oxygen atmosphere before removal from the vacuum chamber.

4.2.2 Synthesis of TiO_2 Films

TiO_2 films were deposited in a high vacuum chamber directly onto 10 MHz AT cut Ti coated QCM crystals with an electron beam evaporator (Omicron EFM3). Depositions were carried out at 35 °C with a base pressure of ~ 7 × 10^{-9} mbar in an oxygen atmosphere of ~ 2 × 10^{-7} mbar. The deposition angle was varied using a custom built rotary QCM holder and the mass deposited during deposition was monitored with a RQCM purchased from Inficon/Maxtek.

4.2.3 Spectroscopic Ellipsometry of TiC

For TiC films spectroscopic ellipsometry (SE) measurements at 60°, 65°, and 70° with wavelengths ranging from 200 – 1000 nm were acquired on a J. A. Woolam M-2000 variable angle spectroscopic ellipsometer. The acquired ellipsometric parameters Ψ and Δ were transformed into the thickness of the deposited TiC films as well as to the real, n, and imaginary, k, components of the complex refractive index using an optical model consisting of two layers, the substrate and the TiC film. RBD deposited films posses structural anisotropy which is difficult to account for with standard ellipsometry.[14,15] To simplify the model for this system all SE measurements were taken with the sample oriented such that the deposition direction is parallel to the incident light beam and the data was fit using an isotropic model consisting of three Lorentzian oscillators. This sample orientation minimizes contributions from film anisotropy which was previously shown on several materials grown at glancing angles.[14,15] Each sample was fit for the film thickness in addition to the amplitude and broadening of these oscillators. Representative fit parameters and fits to ellipsometry data are shown in Figure 4.1.

(a) TiC 13°, e_1= 1.2 t= 117 nm

A	E	B
7.734	1.19	**6.599**
1.036	4.05	**2.027**
2.880	**7.32**	**10**

(d) TiC 50°, e_1= 1.2 t= 159 nm

A	E	B
2.832	1.19	**4.674**
0.546	4.05	**1.000**
2.963	**7.32**	**10**

(g) TiC 60°, e_1= 1.2 t= 178 nm

A	E	B
2.040	1.19	**2.674**
0.483	4.05	**1.109**
2.736	**7.32**	**8.897**

(j) TiC 70°, e_1= 1.2 t= 240 nm

A	E	B
1.334	1.19	**3.947**
0.268	4.05	**0.778**
1.690	**7.32**	**8.121**

(m) TiC 80°, e_1= 1.4 t= 438 nm

A	E	B
2.501	0.5	**2.355**
0.157	4.05	**1.043**
0.653	**7.32**	**10**

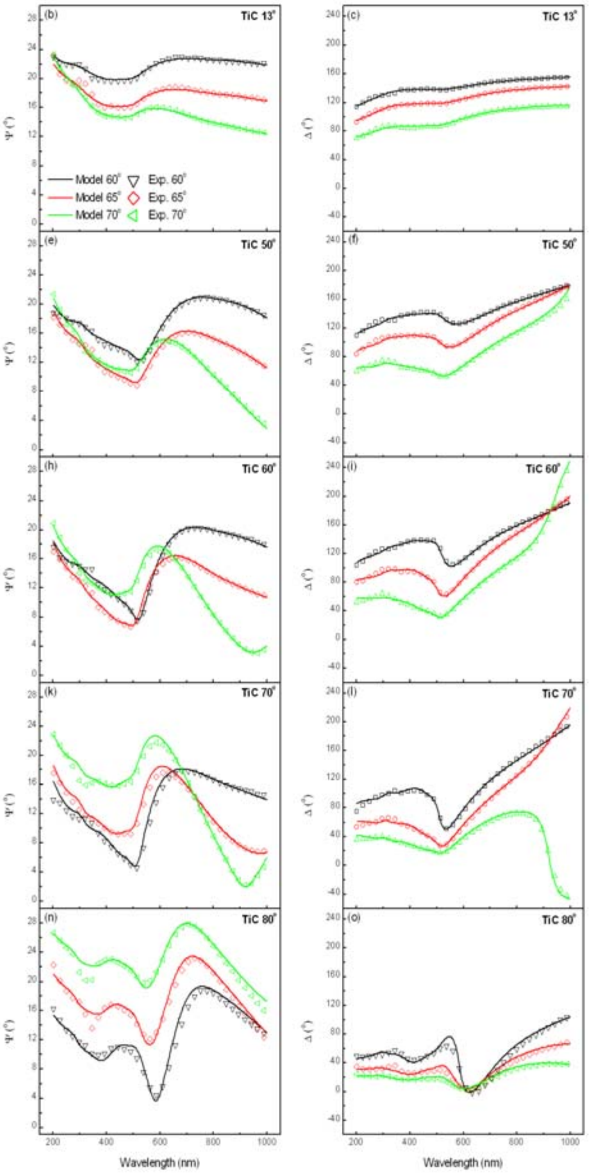

Figure 4.1. Tables of fit parameters (a,d,g,j,m) for three Lorentzian oscillators used to model TiC deposited at 13, 50, 60, 70 and 80° along with corresponding plots of model fits (solid lines) to the ellipsometry parameters (hollow symbols) *Ψ* (b,e,h,k,n) and *Δ* (c,f,i,l,o) taken at three different angles of incidence. The fit parameters *E* and e_1 were held constant during fitting.

4.2.4 Generalized Ellipsometry of TiO_2

Ellipsometry measurements were acquired using a J.A. Woollam M-2000 variable angle spectroscopic ellipsometer. The optical properties of the angle-templated TiO_2 films are dependent on the sample orientation. When the probe beam is incident perpendicular to the deposition plane (perpendicular to the plane of the column tilt) the response of parameters sensitive to anisotropy is maximized, making this the most advantageous position for measuring the Mueller matrix. The Mueller matrix is a 4x4 matrix which is often used to describe biaxial materials such as the RBD deposited TiO_2 presented here.[15,16] The M-2000 employed for these experiments is capable of measuring the first three rows normalized to the first element of the matrix; this is enough to determine the three principal refractive indices. In the perpendicular orientation, scans were taken at angles of incidence of 50° and 60° to avoid interference from the sample holder. This data was modeled from 500 nm to 1000 nm using a biaxial layer, with each principal axis described by a two-parameter Cauchy equation. The Cauchy equation, $n = A + B/\lambda^2$, is frequently utilized to describe normal dispersion in transparent samples. Some samples contained oxygen defects leading to adsorption in the visible wavelength region, so they were annealed in ambient to remove these defects. The film thickness and Euler angle φ (reports on sample orientation) were also set as fit parameters bringing the total number of parameters to 8. The Euler angle θ (related to the column tilt angle) was not set as a fit parameter because of high correlation with the Cauchy parameters, especially those describing n_1; it was set to the column tilt angle as determined by SEM.

4.2.5 Porosimetry Setup

The porosimetry apparatus was modified from that described in Chapter 3. Porosimetry measurements were carried out in a semi-cylindrical quartz flow cell in which the partial pressure of toluene was controlled (P/P_o ± 0.1%) by mixing of a stream of high-purity dry N_2 with a stream of toluene-saturated N_2 using high-precision Inficon digital flow controllers (model P8A). Adsorption and desorption isotherms of toluene on QCM–supported films were acquired by simultaneous measurements of the mass change of adsorbate and the SE parameters with respect to toluene partial pressure. Prior to the porosimetry runs, the films were degassed under flowing N_2 at ambient temperature until the QCM response was stabilized (~ 20 minutes), then the dry N_2 stream was heated to 70 °C for ~ 30 minutes until the resonant frequency of the QCM, f_R, stabilized again. The film was identified to be in equilibrium with the pre-determined partial pressure of toluene by monitoring the change in f_R over time. Changes in f_R measured by the QCM were converted to mass using the Sauerbrey equation. The Sauerbrey equation is valid for rigid, evenly distributed deposits in air or vacuum within ~ 5 % of the crystal resonant frequency, conditions which were met in this study.[17] Changes in the ellipsometric values were more difficult to interpret and will be discussed in the results section.

4.2.6 X-ray Diffraction Measurements

X-ray diffraction (XRD) measurements were acquired in a glancing-incidence detector scan geometry using a Bruker-Nonius D8 advanced diffractometer. The Cu Kα radiation source was operated at 40 kV and 40 mA while a nickel foil filter was used to screen out Cu Kβ radiation. All measurements were carried out in the $\theta/2\theta$ mode with an incident angle of radiation of 1°. The 2θ scan data were collected using a scintillation detector at 0.01° intervals over the range 20 – 80° and a scan rate of 12° min^{-1}. Diffraction features were compared to the powder diffraction files (PDF) widely available for each structure: TiC (PDF # 71-0298), Ti (PDF # 44-1294), Si (PDF # 75-0589), SiC (PDF # 73-2083), and SiO_2 (PDF #70-2539). Additionally, diffraction patterns were compared to those of graphite and other carbon composites as well as titanium oxides.

4.2.7 Scanning Electron Microscopy Measurements

Scanning electron microscopy (SEM) images were obtained using a LEO 1530 electron microscope. A primary electron beam energy of 20 kV and aperture of 30 μm were utilized for capturing images of the titanium carbide films deposited on Si(100) substrates. Profile SEM images were acquired by cleaving a substrate with a deposited film, and examining the freshly exposed edge.

4.2.8 X-ray Photoelectron Spectroscopy Measurements

X-ray photoelectron spectroscopy (XPS) data was acquired using the Kratos AXIS Ultra DLD model spectrometer using Mg Kα radiation. Argon ion sputtering (3 kV, 60 μA·cm^{-2}) at 45° was used to clean the sample by removing the adventitious carbon and native oxide which formed when transferring TiC samples to the XPS system. XPS spectra were acquired for the Ti 2p, C 1s and O 1s peaks both before and after sputtering the sample. Concentrations of Ti, C and O were calculated by multiplying the integrated peak areas, obtained after subtracting a Shirley background,[18] for each individual element by their respective sensitivity factor (2.001, 0.278, and 0.780) as supplied by the manufacturer.

4.3 RESULTS

4.3.1 Film Morphology and Composition

Figure 4.2 displays SEM images illustrating the profile and top views of the as-deposited TiC films grown by depositing the same mass (500 monolayer equivalents of Ti) at 35 ºC in an ethylene background pressure of 2.5×10^{-7} mbar with deposition angles of 13º, 50º, 60º, 70º, 80º and 85º. From these images It is clear that the morphology of the deposited films is sensitive to the deposition angle during film growth.[4-6,9-11,19-31] As the deposition angle is gradually increased from 13° (near perpendicular to surface normal) to 85° (near parallel to the surface), the film morphology evolves from a relatively dense material into a continuous, reticular structure and finally into arrays of discrete columns with characteristic diameters greater than 50 nm. At deposition angles of 70° and higher, nanometer scale voids are resolved by SEM in profile and top-down views.

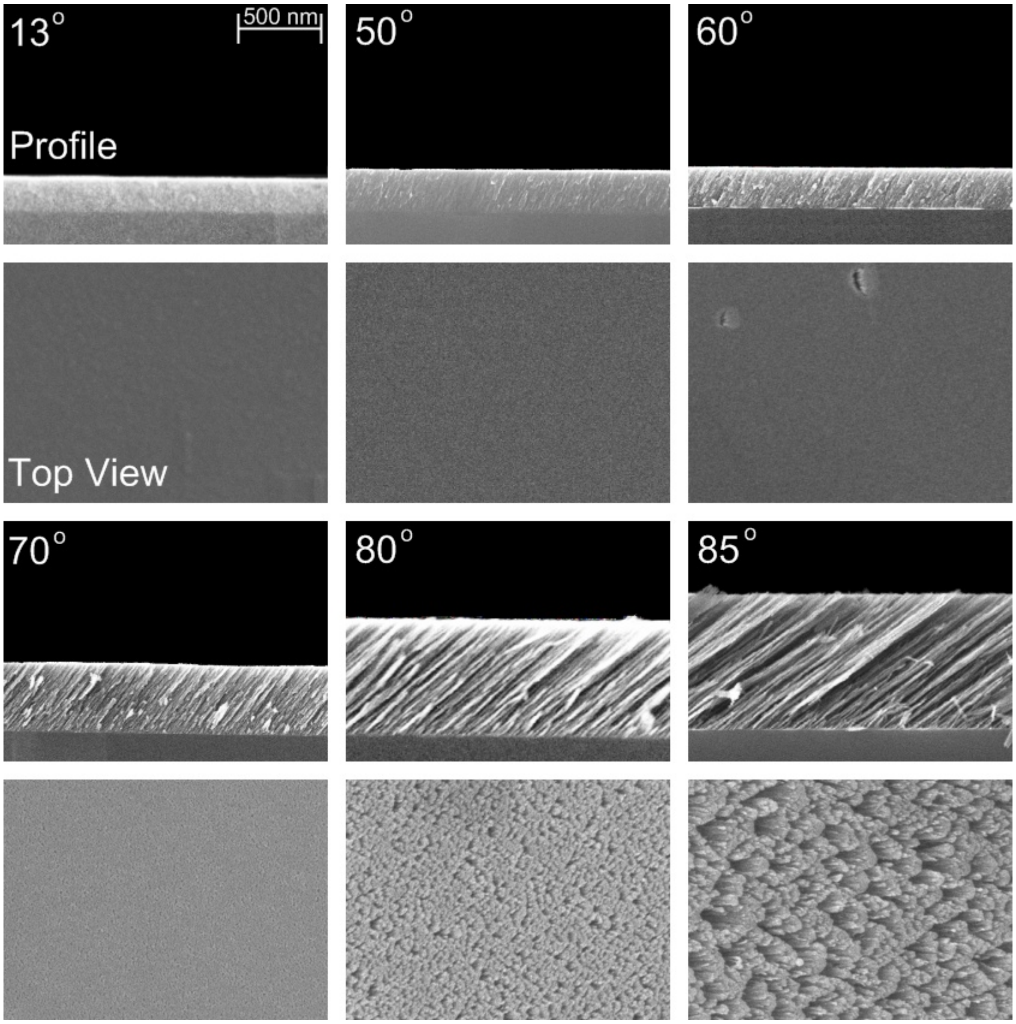

Figure 4.2. SEM images of TiC films grown by depositing 500 monolayers of titanium in an ethylene background at 2.5 × 10^{-7} mbar onto Si(100). Films were deposited at angles ranging from 13º to 85º at 35 ºC.

These changes are also reflected in the optical constants derived by SE for the same mass of TiC deposited at angles ranging from 13º to 80º within the quartz cell under dry N_2 flow, Figure 4.3. The real, *n*, and imaginary, *k*, refractive indices of the films decrease as the deposition angle increases, concomitant with an increase in the volume fraction of voids. To a first approximation this occurs because of a volume averaged blending of the refractive indices of TiC, $n \sim 3.2$, and N_2, $n \sim 1.0$. This is the essence of effective medium approximations through which the refractive index of a material can be determined from the refractive indices of its constituent parts. For example, values of *n* and *k* for TiC 13° (throughout the remainder of this chapter TiC *XY*° indicates a TiC film deposited at an angle of *XY*°) were combined with a void layer ($n = 1$, $k = 0$) using the Bruggeman effective medium approximation (BEMA)[32] to measure the porosity controlled by the deposition angle; the same approximation was performed for each film. The BEMA method relates a composite material's refractive index to the known refractive indices of its individual components thus yielding the volume fraction of each constituent.[32] This approach provided results within a few percent of those determined using the QCM measured film mass and SE derived film thickness. The angular dependence of the porosity (calculated from the mass and thickness data acquired by QCM and SE, respectively) of TiC films deposited by RBD is shown in Figure 4.4. The results closely follow the predictive model developed by Poxson et al.[33]

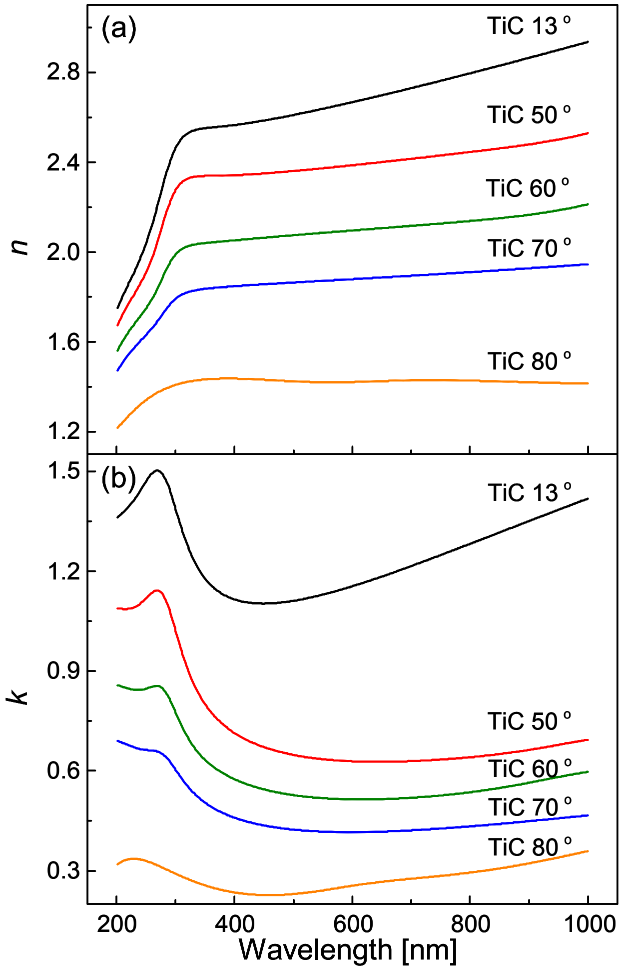

Figure 4.3. Plots of (a) real, *n*, and (b) imaginary, *k*, portions of the complex refractive index derived using an isotropic approximation. Both *n* and *k* decrease with an increasing deposition angle due to the increasing film porosity.

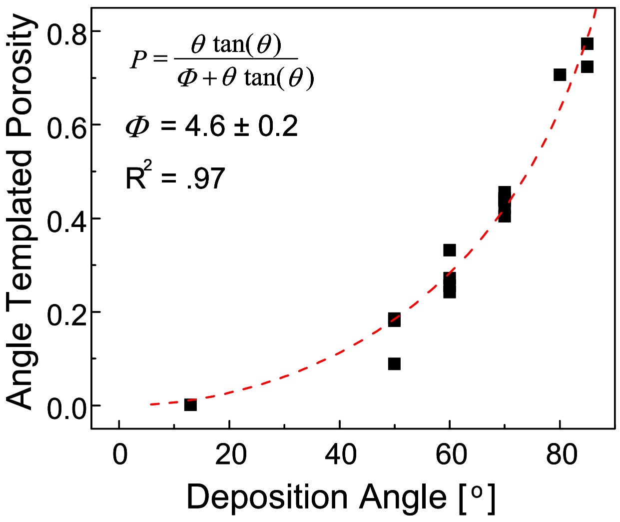

Figure 4.4. Plot of the angle templated porosity determined at various deposition angles using the film mass measured via QCM during deposition and the film thickness derived from SE measurements. The angular dependence of the porosity of films deposited by related glancing-angle deposition techniques has been modeled by Poxson et al. utilizing geometric arguments concerning the nucleation and growth of films formed from self-organized arrays of nanocolumns.[33]

X-ray diffraction measurements indicate that the films, as-deposited at 35 ºC, are crystalline. Figure 4.5 shows XRD patterns acquired from TiC films grown by deposition at angles ranging from 13º to 85°. This analysis indicates that the mean crystallite grain size, determined by Scherrer analysis, within each columnar or reticulated TiC film ranges from 9.9 nm to 6.9 nm, with the average size decreasing with increasing deposition angle and film porosity. The diffraction pattern exhibits a number of diffraction features from TiC indicated by blue arrows, corresponding to the (111), (200), (220), (311) and (222) crystal planes. Features originating from the Si(100) substrate and its thermal oxide, SiO_2, are apparent within the range of 45 – 58° and are designated with a red triangle. No diffraction features indicative of metallic titanium, graphite, or other forms of carbon were observed for TiC films deposited by RBD. Although the TiC films adsorb large quantities of oxygen during passivation and exposure to air, no features corresponding to titanium oxide phases were observed. Since exposure to oxygen occurs at room temperature, the interaction of oxygen with the TiC film forms an amorphous oxycarbide overlayer as confirmed by XPS spectra, Figure 4.6.

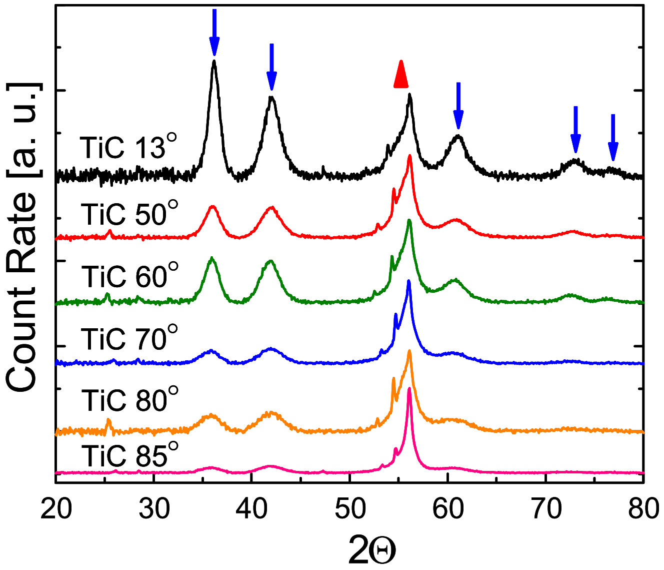

Figure 4.5. X-ray diffraction patterns for the TiC films deposited on Si(100) substrates at 35 °C with deposition angles ranging from 13° to 85°. TiC diffraction peaks, marked with a blue arrow, occur at 2θ values of 36, 42, 61, 73 and 77° and correspond to the (111), (200), (220), (311) and (222) crystal planes, respectively. The diffraction features indicated with a red triangle correspond to the Si(100) substrate and its native oxide, SiO_2.

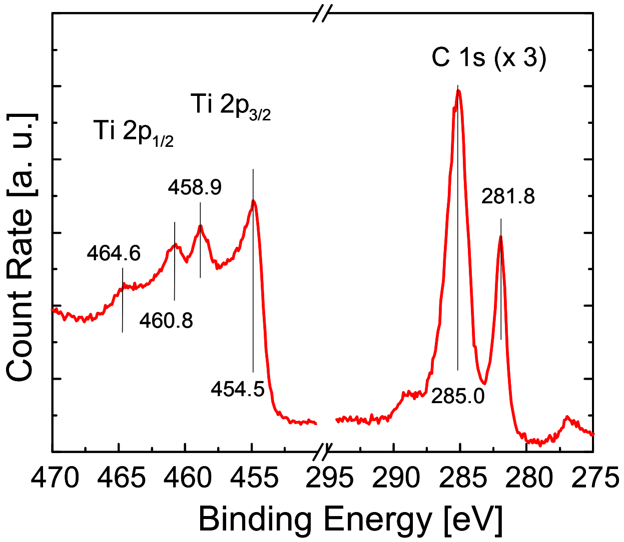

Figure 4.6. X-ray photoelectron spectrum of the TiC 13° film acquired immediately after introduction into the XPS system (the surface was not cleaned by Argon ion sputtering). It is clear from the peak positions within the Ti 2p photoelectron spectrum that titanium exists in metallic (454.5 and 460.8 eV) and oxidized (458.9 and 464.6 eV) states. Oxygen was also observed on the film's surface by measuring the O 1s feature (not shown). Additionally, the C 1s spectrum reveals that both graphitic-amorphous carbon (285.0 eV) and carbidic carbon (281.8 eV) are present. The estimated atomic composition of the surface was 21 % titanium, 48 % carbon, and 31 % oxygen.

4.3.2 Toluene Isotherms on TiC

Toluene adsorption isotherms were obtained via QCM/EP for films deposited at angles ranging from 13° to 80° and are presented in Figure 4.7. As seen in Figure 4.7, the volume fraction of adsorbed toluene and the partial pressure at which the adsorption-desorption hysteresis occurs increase with increasing deposition angle, indicating that both the total capacity for toluene adsorption and the mean pore diameter increase with deposition angle.

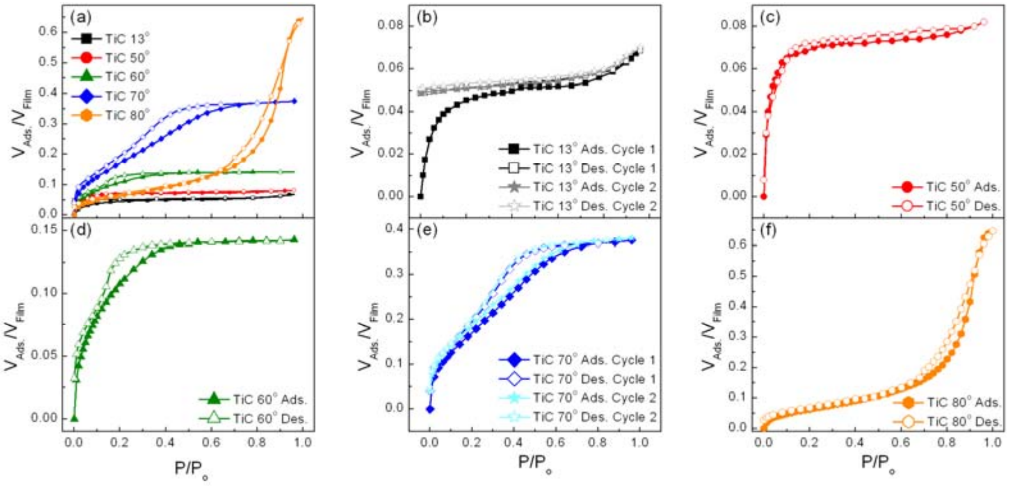

Figure 4.7. Plots of the volume fraction of adsorbate versus the film volume determined for toluene isotherms on TiC films deposited at various angles. (a) Overlay of isotherms for the samples of all angles indicating the relative magnitude of adsorption. Individual isotherms with solid symbols corresponding to the adsorption branch and hollow symbols to the desorption branch of the each isotherm for (b) 13°(■), (c) 50°(●), (d) 60°(▲), (e) 70°(♦), and (f) 80° (⬣) TiC films. Another subsequent isotherm was performed on all samples but all except the 13° and 70° have been omitted for clarity.

The sample deposited at 13° (Figure 4.7 (b)) was expected to be nonporous in which case the film would exhibit a Type II adsorption isotherm, concave adsorption relative to the x-axis followed by increased adsorption at high partial pressures due to multilayer formation, consistent with adsorption on nonporous surfaces.[34,35] However, the isotherm demonstrates Type I behavior, characterized by relatively large adsorption at low partial pressures followed by a region of constant adsorption at moderate partial pressures.[35] Type I isotherms typically arise from adsorption onto a microporous (pores < 2 nm in diameter) surface, though they can also arise from very strong attraction between the adsorbate and the surface, leading to very early monolayer formation. Here, the Type I isotherm arises because of the presence of micropores as the toluene adsorption at P/P_o = 0.1 is ~ 100 times greater for TiC 13° compared to the bare QCM or TiO_2 13°, both of which are non-porous. The greater adsorption capacity of the TiC 13° film must arise due to toluene adsorption within micropores. This means that the BET C value of 108 (when taken by itself would indicate high adsorption energy for toluene) is artificially inflated by the presence of the micropores.[35] Strong interaction between the film and toluene is also not expected based on our previous work on TiO_2 (recall that the TiC surface is almost completely oxidized) which indicated low C values for toluene adsorption on TiO_2.[36,37] The isotherm also exhibits a significant hysteresis at low partial pressures which is attributed to trapping of adsorbate molecules in micropores.[35] A subsequent adsorption-desorption cycle on TiC 13°, shown in Figure 4.7 (b), demonstrated a lack of adsorption at low partial pressures and exhibited a shape similar to a Type II isotherm with much lower mass adsorption.[35] Additionally, the calculated C value approached a value of one which is consistent with adsorption on a nonporous substrate with very weak adsorbate-adsorbent attraction. The irreversible isotherms evident on TiC 13° contrast sharply with measurements made on samples grown at higher deposition angles. Subsequent adsorption-desorption cycles on samples deposited at angles from 50º to 85° are nearly identical with the initial cycle, except for a small amount of irreversible adsorption in the micropore region, $P/P_o < 0.05$. For clarity of presentation only the first and second adsorption-desorption cycles for the TiC film deposited at 70° are presented in Figure 4.7 (e) which are representative of the repeatability of the other isotherms. In summary, adsorption data for TiC deposited at 13° is consistent with irreversible toluene adsorption inside very narrow micropores during the first adsorption cycle, after which the second cycle indicates very weak interaction between toluene and the external surface.

Isotherms of toluene adsorption on TiC deposited at 50° (Figure 4.7 (c)) are also consistent with Type I isotherms. These isotherms indicate a diminished low pressure hysteresis in comparison to the 13º film, as well as an increase in the total volume fraction of toluene adsorbed. These changes suggest that the 50º deposition angle templates slightly larger micropores which do not trap toluene as readily as those within the 13º films. Deposition at 60° results in isotherms that exhibit significant adsorption at low pressure;

however, these films now include a hysteresis loop extending from P/P_o ranging from 0.1 to 0.4, Figure 4.7 (d). Repeatable hysteresis loops at these higher partial pressures are associated with capillary condensation in mesopores, which are defined as pores between 2 – 50 nm in diameter.[35] The volume fraction adsorbed continues to increase as the deposition angle increases to 70° and 80°, as shown in Figure 4.7 (e) and (f). Additionally, the hysteresis loop of these films broadens and shifts to higher partial pressures, consistent with an increase in the mean pore diameter with increasing deposition angle. The shape of the hysteresis loops become increasingly elongated resembling that of a Type H3 hysteresis which suggests adsorption between plate like particles.[35] This observation is consistent with the SEM images shown in Figure 4.2 indicating that at deposition angles of 60° and greater the film is comprised of closely spaced nanocolumns with roughly elliptical cross-sections. As observed in SEM, increases in the deposition angle from 60° to 85° lead to greater separation between the nanocolumns which are reflected in the corresponding toluene isotherms.

4.3.3 Pore Size Distribution of TiC

The Kelvin equation, $r_\kappa = \dfrac{-2\gamma V_m \cos(\theta)}{RT\ln\left(P/P_0\right)}$, was employed to quantitatively evaluate the mesopore size distribution (PSD). In the case of toluene adsorption $\gamma = 0.0284$ N·m^{-1}, $V_m = 1.06 \times 10^{-4}$ m^3·mol^{-1}, $\theta = 0$, $R = 8.314$ J·mol^{-1}·K^{-1} and $T = 290$ K. Figure 4.8 presents the PSD derived from the desorption branch of the isotherms performed on the 60, 70 and 80º samples. The limitations of the Kelvin equation are widely known, especially with pores in the 2 – 10 nm size range. In previous work we have found very good agreement between the pore diameter determined by the Kelvin equation and SEM and XRD measurements for porous TiO_2 films.[36] However, because of the potential for ambiguity results are discussed in terms of the Kelvin radius and not the pore size. These measurements show the dramatic dependence of the TiC film morphology on the deposition angle. The Kelvin radius, r_K, increases from 1.2 ± 0.1 nm for the 60º deposition to 1.8 ± 0.3 nm for the 70º deposition and to 9.4 ± 9.0 nm for the 80º deposition. Fine control of the pore structure of these films is important for a variety of the application of TiC or other metal carbides. At these size ranges quantum effects may dominate with small changes in the size of columns potentially having great effect on material properties.[38] Additionally, for applications in catalysis where high surface area TMCs are frequently employed, post-synthesis deposition and distribution of nanoparticles inside the porous network will be strongly dependent on pore size.[36] Further, direct control of the pore sizes of carbides for the production of electrochemical capacitors will certainly affect the porous architecture of the resulting carbons.[39]

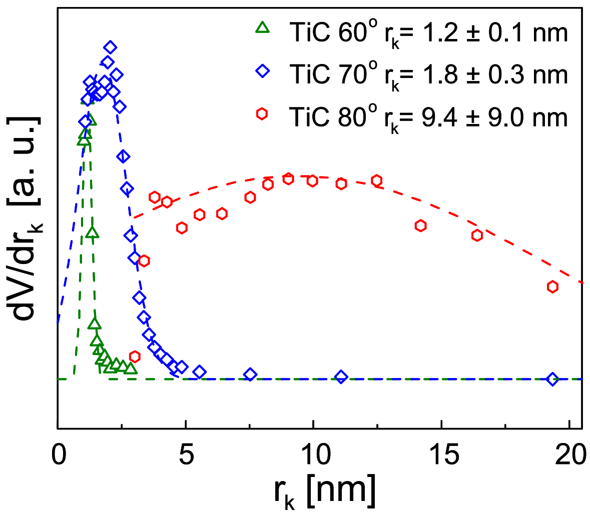

Figure 4.8. Mesopore size distribution as determined from the desorption branch of toluene adsorption isotherms on TiC films deposited at 60° (△), 70° (◊), and 80° (⬡).

4.3.4 Surface Area Analysis of TiC

The Brunauer-Emmett-Teller (BET) method is perhaps the most popular technique for determining the specific surface area (SSA) of high surface area media; however, the BET equation is generally considered inaccurate for samples with weak interaction between the adsorbate and surface or significant microporosity. Specifically, if the completion of the adsorbate monolayer can not be distinguished from the development of the multilayer (indicated by low *C* values) or if the monolayer coincides with micropore adsorption, then the BET monolayer capacity can not be determined accurately. Lack of a well defined monolayer capacity introduces significant uncertainty into SSA values. These limitations mean that the BET method is not suitable for application to the isotherms determined in this study. On the other hand, application of the BET method is still instructive for comparison with more traditional studies, and for determining the BET *C* values, which can indicate the presence of microporosity. For this purpose, SSA and *C* values for the films have been estimated using the BET method (applied over the range $P/P_o = 0.05 – 0.35$) and are displayed in Table 4.1. The calculated BET surface areas increase with increasing deposition angle from 14 $m^2 \cdot g^{-1}$ to 240 $m^2 \cdot g^{-1}$, an increase that displays a high degree of linearity ($R^2 > 0.99$) from 50° to 80°. This contrasts with a previous investigation of TiC films deposited using RBD. In the prior study, cyclohexane was adsorbed on the films at 140 K under ultrahigh vacuum to quantify the adsorption capacity which was employed to calculate the specific surface area using a known standard. The surface area reached a maximum of 840 $m^2 \cdot g^{-1}$ at a deposition angle of 65º and deposition temperature of 77 ºC.[6] In the preceding study, deposition at an angle of 65º and temperature of 27 ºC (more comparable to conditions used here) resulted in a specific surface area of ~ 700 $m^2 \cdot g^{-1}$.[6] Clearly, this value is much larger than the maximum value of 240 $m^2 \cdot g^{-1}$ determined by BET analysis of toluene adsorption presented here. Further, the BET method indicates that the film deposited at an angle of 80° has the highest surface area, whereas previous work demonstrated that the maximum value should occur between 60° and 70°.

Differences in the surface area measurements between the two studies are easily resolved by employing an alternative analysis of the isotherms, presented here. The α_s method, developed by Sing and coworkers, is an empirical technique that can be confidently applied to a broad array of isotherms as long as a reference isotherm on a chemically similar nonporous material has been obtained.[35] To monitor adsorption mechanisms on the porous TiC samples, a reference isotherm was generated by depositing a TiO_2 13° film using a similar RBD method (TiC 13° films were unsuitable due to the large hysteresis at low pressures).[5] The reference isotherm and the calculated α_s plots are shown in Figure 4.9.

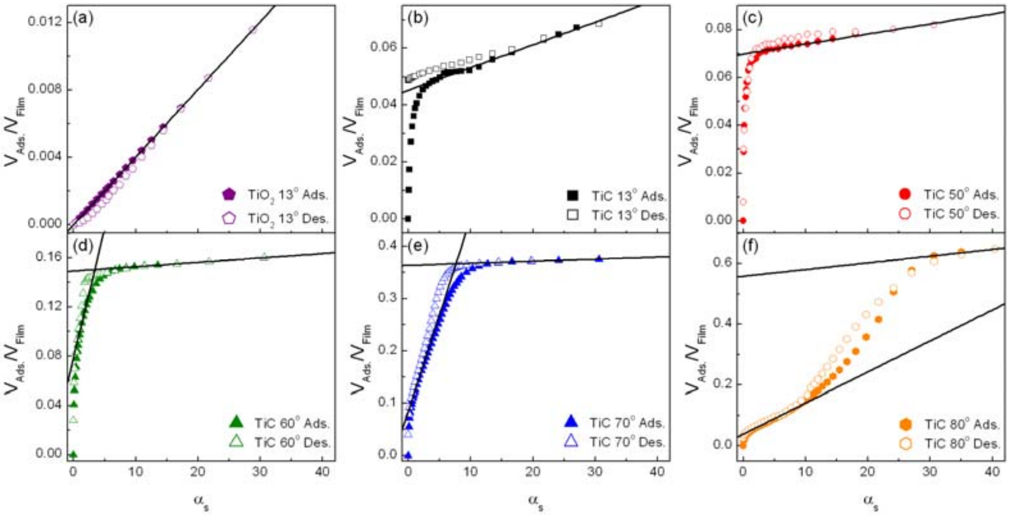

Figure 4.9. The α_s plots determined employing a reference isotherm obtained using toluene on a chemically similar TiO$_2$ 13° film deposited by the same method as the TiC 13° film.

Table 4.1. BET and α_s Analysis of Deposition Angle-Templated TiC Samples

Dep. Angle (°)	BET S.A. ($m^2 \cdot g^{-1}$)	*C*	Micropore Volume	Mesopore Volume	α_s S.A. ($m^2 \cdot g^{-1}$)
13	14	108	0.05	0	10
50	30 ± 10	180 ± 70	0.07	0	10
60	100 ± 30	32 ± 8	0.08	0.07	410
70	180 ± 50	21 ± 4	0.09	0.27	710
80	240 ± 30	23 ± 6	0.04	0.52	240

Values for the surface area as well as micropore and mesopore volumes calculated by the α_s method are displayed in Table 4.1. As seen in Table 4.1, the volume ratio of mesopores to micropores increases with deposition angle from ~1:1 for the 60° film to ~13:1 for the 80° film. Due to a low C value (characteristic of Type III isotherms and indicating an unreliable value for the monolayer capacity) the surface area of the TiO_2 reference sample could not be determined by BET methods. Therefore, the relative surface areas were converted to absolute surface areas using the BET value obtained for the 80º sample. The 80º isotherms were close to ideal Type IV isotherms with low micropore volumes and exhibited very linear ($R^2 > 0.999$) BET plots from $P/P_o = 0.05$ to $P/P_o = 0.50$, suggesting that it closely adheres to the BET model. The α_s surface area values are considered external surface areas because they do not include contributions from micropores. Values of the external SSA for TiC films calculated by the α_s method are displayed in Table 4.1. The maximum SSA for the deposited TiC films was 710 $m^2 \cdot g^{-1}$ for TiC 70°. This value closely corresponds to the value of ~ 700 $m^2 \cdot g^{-1}$ observed for TiC films deposited at an angle of 65° and 27 °C in the previous study.[6] Additionally, SSA values for TiC 60° and TiC 80° are in general agreement with values from the previous study. In contrast, the TiC 13° and TiC 50° films have much smaller surface areas than the mesoporous samples. This is expected since the porosity, and thus most of the templated surface area, of these films is due to the presence of micropores that are expressly excluded from α_s analysis which only takes into account external surface area.

4.3.5 Ellipsometric and QCM Porosimetry of nonporous samples

Nonporous TiO_2 films are an ideal substrate for comparing EP and QCMP. Porous samples have complications such as irreversible adsorption and optical anisotropy which make obtaining reproducibility and deriving the volume adsorbed difficult. In contrast, nonporous TiO_2 is completely reversible and can be modeled with an isotropic Cauchy layer consisting of three fit parameters (A, B, and thickness). From QCM measurements the amount adsorbed is calculated using the Sauerbrey equation to convert the QCM frequency shift to mass per unit area (ng/cm^2). To determine the mass adsorbed using EP the optical constants of the substrate were determined at $P/P_o = 0$. Then, another Cauchy layer, representing the adsorbed toluene, is fit for thickness. As P/P_o increases the measured toluene layer thickness increases and can be easily converted to ng/cm^2 by multiplying the thickness by the bulk density of toluene. Results shown in Figure 4.10 are for four isotherms taken continuously on the same nonporous TiO_2 sample which had been annealed to 300 °C, the error bars are one standard deviation. Agreement between the two curves is excellent with similarly shaped type II isotherms typical of adsorption on nonporous surfaces with relatively weak attraction between the adsorbate and the surface. Agreement between the EP and QCMP results, in addition to the standard shape of the isotherms, validates the accuracy of both techniques, and indicates their excellent reproducibility as seen in the small standard deviation of both techniques. Another important result is that agreement between the two techniques validates the assumption that the film density does not vary significantly from the bulk. The bulk density of toluene was used for converting the ellipsometry results to mass adsorbed, both explicitly and implicitly through assuming the bulk toluene *n*, while density was not utilized to determine the adsorbed mass from the QCM data. Therefore, agreement between the two curves means that the density and refractive index of adsorbed toluene is the same as the bulk values. The persistence of bulk behavior also agrees with our previous work with EP which showed that that toluene adsorbed in TiO_2 with 10 nm columnar pores also maintains bulk properties.

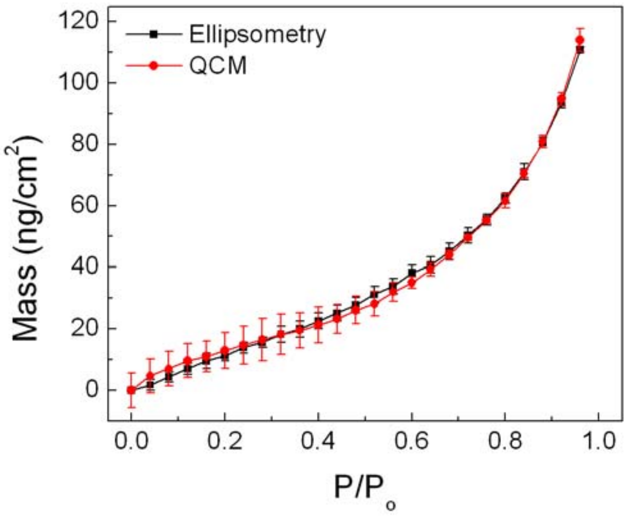

Figure 4.10. Comparison of the mass adsorbed measured using Ellipsometry and QCM porosimetry for toluene adsorption on dense TiO_2.

4.3.6 Ellipsometric and QCM Porosimetry of TiC

Ellipsometric porosimetry (EP) utilizes ellipsometry to monitor changes in the refractive index and thickness of a sample as it is exposed to increasing concentrations of an adsorbate. However, neither quartz crystal microbalance porosimetry (QCMP) or ellipsometric porosimetry (EP) directly measure the mass of adsorbate on a porous sample. For QCMP the measured quantity is the dampening of the resonant frequency of the quartz oscillator during adsorption. Generally the conversion of Δf_R to mass is relatively straightforward via the Sauerbrey equation.[17] The EP data was much more difficult to interpret due to large absorption of light by the TiC samples across the measured spectral range and a high degree of optical anisotropy for films deposited at angles greater than 50°. Toluene does not absorb light in the 300 – 1000 nm range, so initial attempts were made to keep the k values determined at $P/P_o = 0$ constant (by holding the amplitude and broadening of the optical model's Lorentzian oscillators constant) and only fit for changes in n and thickness by adding a Cauchy dispersion equation to the series of Lorentzian oscillators describing the TiC.[32] This approach did not result in acceptable fits to the ellipsometry data for any of the deposition angles and was abandoned. Therefore, n, k and thickness (a total of eight fit parameters) were allowed to change during fitting of the SE data from 300 – 1000 nm. This method resulted in good fits to the SE data but caused concerns over parameter correlation and raised the question of why k would change at all.

We speculate that the measured change in k is an anomaly of the fitting procedure and not an expression of vapochromic properties of the TiC samples.

Despite these difficulties, a method utilizing the Bruggeman effective medium approximation was successfully employed to compare the EP and QCMP data, as shown in Figure 4.11. In this implementation, it was assumed that the EP data at a given partial pressure could be described by a mixture of the complex refractive index at $P/P_o = 0$ and the complex refractive index determined just after pore saturation ($P/P_o = 0.30$ for TiC 50° and $P/P_o = 0.64$ for TiC 70°). The thickness of the film and the proportional contribution of the unsaturated and saturated films to the refractive index were the only two fit parameters. The resulting fraction gives the amount of accessible porosity that has been filled by adsorbate, as shown by Sanchez et al.,[40] and can be compared to the QCMP data acquired at the same time.

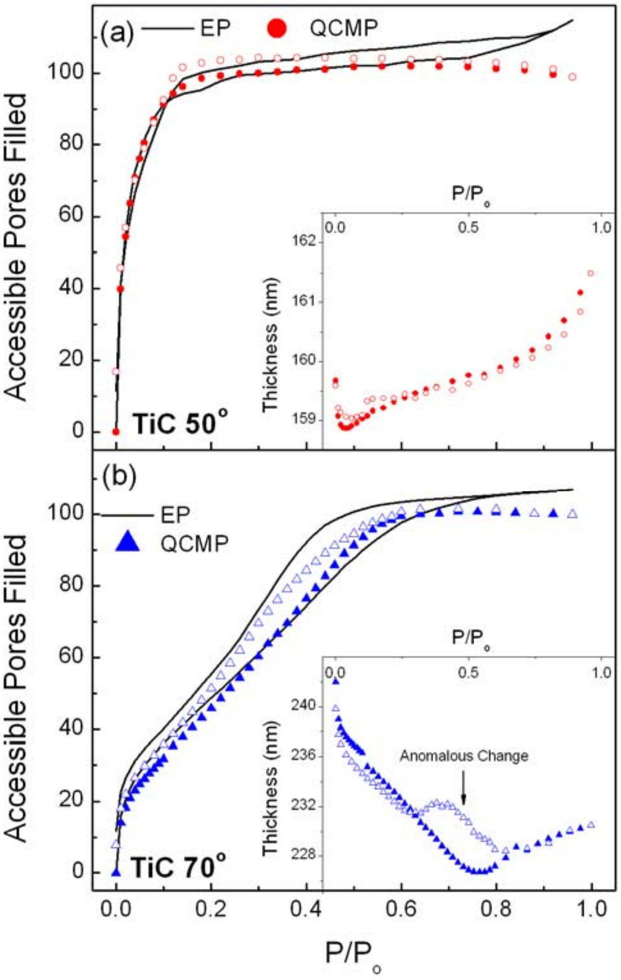

Figure 4.11. Comparison of the fraction of accessible pores filled by the toluene adsorbate versus partial pressure determined by EP (symbols) and QCMP (lines) for TiC deposited at angles of (a) 50° and (b) 70°. Insets depict the thickness change determined by EP, note that on the desorption branch in (b) depicts an anomalous thickness increase observed for all isotherms with hysteresis loops.

For the TiC 50° sample, Figure 4.11 (a), agreement between the two methods is excellent, differing by an average of only 1 % before saturation at $P/P_o = 0.30$. At higher partial pressures the values diverge, especially above $P/P_o = 0.80$. This divergence was observed in every film for which a saturated plateau was observed (i.e., TiC 13°, TiC 50°, TiC 60°, and TiC 70°). This region corresponds to multilayer formation on the surface of the TiC. The QCM detects these multilayers as a mass change and the isotherm curves upwards at higher partial pressures consistent with multilayer formation. In contrast, the EP isotherm remains constant or decreases slightly after saturation. Recall that this isotherm is determined only by accounting for changes in the complex refractive index and not the measured thickness values. Once the open porosity ($n_{nitrogen} = 1$) of the film has been replaced by toluene ($n_{toluene} = 1.49$) there is no additional change in the refractive index of the sample with further increases in P/P_o. The small changes in refractive index as the toluene forms multilayers on the surface are negligible compared to the refractive index of the film. However, this does not mean that the additional adsorption is undetectable. Note the inset to Figure 4.11 (a), the measured thickness increases at higher partial pressures and has a shape that is similar to that seen in the QCMP data. Thus, ellipsometry is capable of detecting the multilayer adsorption, via shifts in Δ, but it is seen as a thickness change and not a change in the complex refractive index. This subtle difference in detection is important when analyzing EP data, especially concerning α_s plots which rely on the shape of the isotherm to determine parameters such as pore volume and surface area.

Analysis of the ellipsometrically derived thickness changes reveals other interesting phenomenon as well. The thickness of the 50° sample decreases slightly at low toluene partial pressures due to capillary condensation within this film. This observation is in contrast to the thickness of the TiC 13° and TiO_2 13° films which increase monotonically throughout the entire pressure range due to multilayer formation on the film surface. Recall that the increased reversibility of toluene adsorption on TiC 50°, in comparison to TiC 13°, was attributed to enlarged micropores templated by the 50° deposition angle which do not trap toluene as readily as the smaller micropores within the 13° film. Condensation inside these larger micropores can form a meniscus, the associated capillary forces which cause the decrease in film thickness seen in the inset of Figure 4.11 (a). Capillary adsorption in large micropores has been observed and is further evidence that deposition at 50° results in larger micropores than deposition at 13°.[35]

EP and QCMP isotherms taken on TiC 70° are indicative of isotherms obtained at other angles. As the partial pressure of toluene is increased, agreement between the adsorption branches as measured by EP and QCMP for TiC 70° (Figure 4.11 (b)) is good, although it diverges in the multilayer adsorption region due to the factors discussed above. As expected, the overall thickness of the entire film decreases as mesopores are filled and the resulting capillary forces increase leading to a ~ 10 % decrease in film thickness.

Following the completion of capillary condensation, the film thickness increases due to a combination of relaxation of the capillary forces and multilayer formation at high partial pressures, $P/P_o > 0.75$. As the partial pressure of toluene is decreased during the desorption branch, the EP data diverges by as much as 8 % from the QCMP data. This divergence is accompanied by an unexpected increase in the thickness measured by EP (Figure 4.11 (b) inset). At $P/P_o < 0.60$, the hysteresis loop closes and the agreement between EP and QCMP improves considerably. Similar anomalies in the SE derived thickness were observed in the hysteresis loop region of all Type IV isotherms taken in this study and under certain fitting conditions in a previous study of TiO_2.[36] Thin film stress effects are known to impact the response of QCMs;[41] therefore, one possibility for this difference is that stress associated with capillary forces due to the toluene condensation within the films' pores affected the f_R of the QCM, producing anomalous QCMP results. To determine if stress was a factor, similar TiC films were deposited at 50, 60 and 70° on BT cut quartz crystals. BT cut crystals have a stress response that is approximately equal in magnitude to AT cut crystals but opposite in sign. Therefore, differences between isotherms of identical films deposited on each crystal type can be used to determine the contribution of stress to the frequency response.[41] Isotherms conducted on TiC 50°, TiC 60° and TiC 70° deposited on AT and BT cut quartz were within experimental error of film deposition (Figure 4.12), so adsorbate induced stress in the QCM crystal is not a significant contributing factor, although subtle effects would not be detected due to variations in the deposited films. Thus, the difference in the QCMP and EP isotherms is most likely due to errors associated with the analysis of the ellipsometry data. The difference can be ascribed to high parameter correlation between the thickness and BEMA fraction parameters though the resulting fits were independent of seed values and it is odd that correlation issues would only arise in a specific portion of the isotherm. One possibility is that the ellipsometry parameters are more sensitive to stress than the QCM crystals, although further study is necessary to conclusively determine the origins of these EP anomalies.

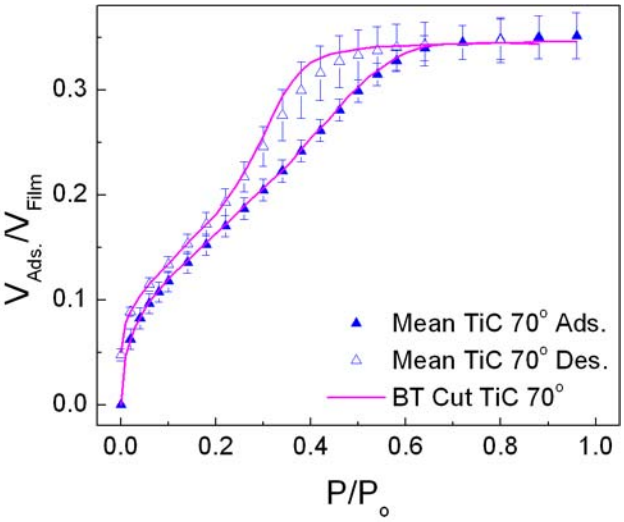

Figure 4.12. Comparison of isotherms performed on TiC 70° with an isotherm performed using a BT cut crystal, the error bars are one standard deviation. There is some disagreement between the cuts especially in the hysteresis region; however, any difference could not be separated from variations in the films, meaning that any contribution form crystal stress would be very small if present at all.

4.3.7 Porosimetry of RBD TiO_2

4.3.7.1 Film morphology and optical properties

SEM images of RBD deposited TiO_2, Figure 4.13, clearly indicate similar angle dependent morphology to TiC. The film structure evolves from a continuous structure at near normal incidence (Figure 4.13 (a)) to films with increasingly defined columnar structure from 55° to 85° (Figure 4.13 (b)-(e)). Interestingly the pore size of these samples exhibits less angle dependence than the TiC as evidenced by the SEM images and isotherms shown in Figure 4.15. One explanation for the difference in these two data sets is that surface diffusion of TiO_2 is more facile than TiC.

The optical and structural properties of RBD deposited films are intimately related. Anisotropy arises from the contrast between the refractive index of the columns and their surroundings. This structure imparts biaxial optical properties with orthorhombic symmetry. The three principal axis are defined in Figure 4.13 (b). The axis labeled one proceeds along the column direction while axis two is perpendicular to the columns and axis three is perpendicular to the deposition plane (coming out of the images in Figure 4.13). These axes do not align with the laboratory axis and must be rotated using the Euler angles φ, θ and ψ. For these samples φ was known approximately based on the sample orientation, but was set as a fit parameter for all samples at $P/P_o = 0$ to account for uncertainty in its position, varying by a few degrees. The parameter θ is dependent on the column tilt angle. This value could not be set as a fit parameter as it was highly correlated to other fit parameters, having an especially significant effect on the birefringence observed between n_1 and n_3. Therefore, θ was fixed to column tilt angle values obtained from cross-sectional SEM images. Many other studies on RBD deposited films have indicated good agreement between fitted values of θ and those measured by SEM.[14,42] Optical constants derived for TiO_2 deposited at 65° and 85° and annealed to 300 °C are presented in figure 4.14 (a). The annealing process was necessary to eliminate absorption due to oxygen deficiencies in samples deposited at < 65°. These optical constants were measured in a dry nitrogen environment to remove interference from ambient adsorbates such as water. For both samples, and indeed for all angle-templated films, the refractive indices follow the expected trend of $n_3 > n_1 > n_2$ and are in general agreement with optical constants derived on similarly deposited films.[16] The real refractive index of all three principal axes is strongly correlated with porosity, decreasing at about the same rate for all three (Figure 4.14 (b)).

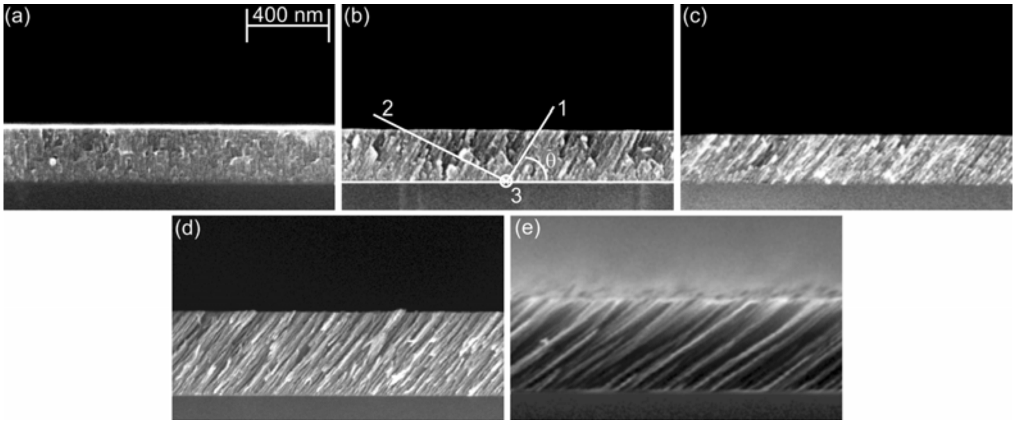

Figure 4.13. SEM images of TiO_2 deposited via RBD at angle of (a) 13º (b) 50º (c) 60º (d) 70º and (e) 80º. The three principal axes are drawn in image (b) and are orthorhombic with an angle θ corresponding to the column tilt angle.

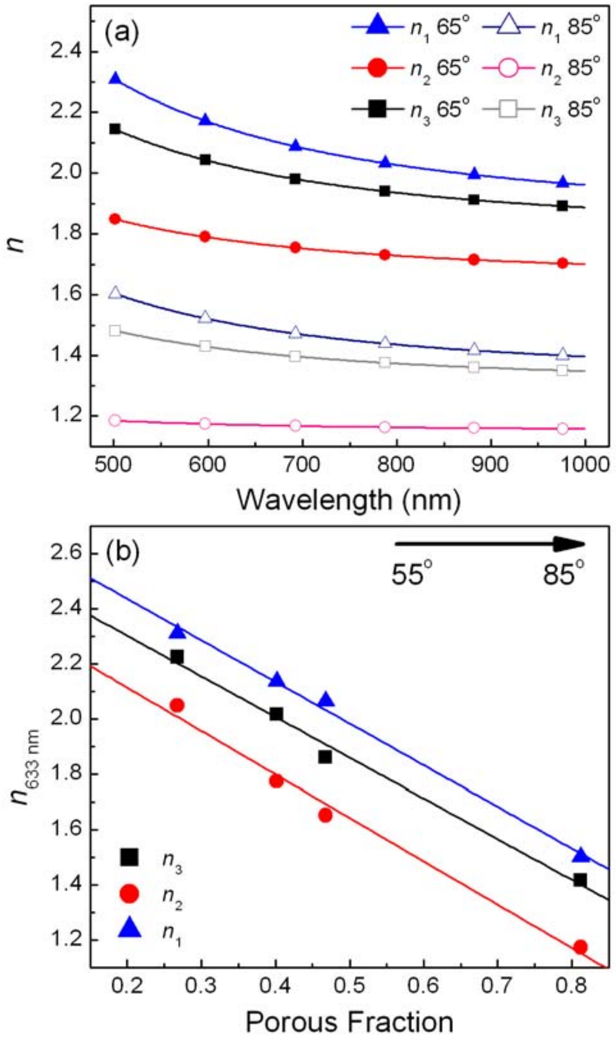

Figure 4.14. (a) Optical constants derived for RBD deposited TiO_2 at 65° and 85° after being annealed at 300 ºC. (b) The refractive index has a linear dependence on porosity decreasing at approximately the same rate for all three principal refractive indices.

4.3.7.2 QCMP of Porous TiO_2

The porosity of deposited TiO_2 films increases with deposition angle from around 30 % porosity at 55° to 80 % at 85° (Figure 4.14 (b)). The total volume of toluene adsorbed also increases with angle to a maximum of 30 % of the film volume ($V_{Ads.}/V_{film}$= 0.30) for samples deposited at 75° (Figure 4.15 (a)). The 85° film does not follow this trend reaching a maximum at 16%. Samples deposited at this large angle are more analogous to freestanding arrays of columns rather than the porous films deposited at smaller angles. These structures may not lend themselves to capillary condensation. Additionally, the isotherm was ceased at P/Po= 0.98 to avoid complications from condensation in the sample chamber which occur at $P/P_o = 1$. This means that the largest mesopores, which make up a significant portion of the 85º films porosity would not be filled. The lack of a hysteresis loop is further evidence that significant capillary condensation did not occur in the 85° sample. The hysteresis loops of the lower angles are elongated, Type H3, and are consistent with broad pore size distributions with significant overlap between angles. This is in sharp contrast to isotherms in Figure 4.7 for RBD deposited TiC films. Those isotherms demonstrated more abrupt changes following desorption, forming a Type H2 hysteresis loop, and also had a much greater dependence of pore size on the deposition angle.

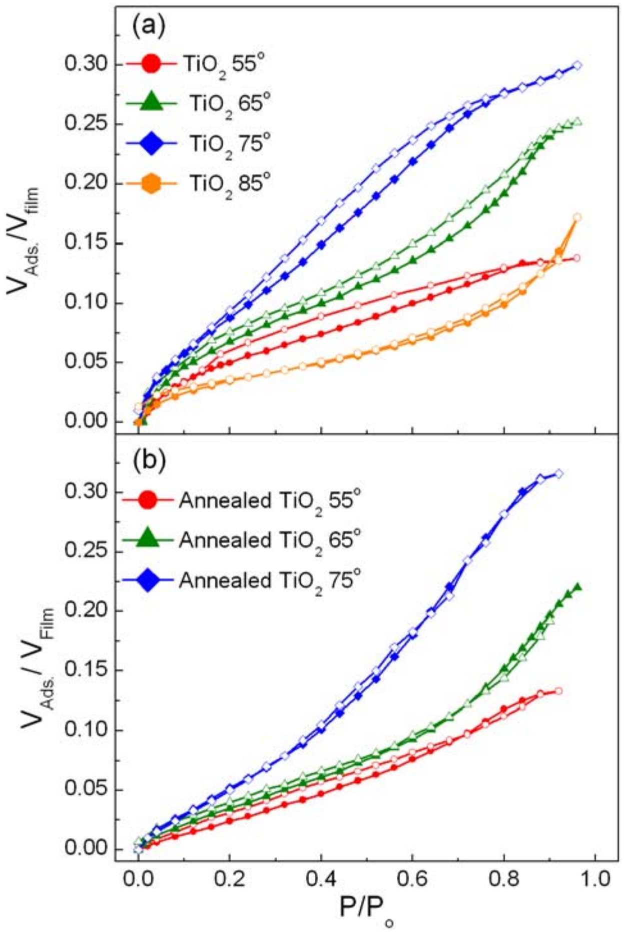

Figure 4.15 Toluene adsorption isotherms measured via QCM before (a) and after (b) annealing at 300 °C. TiO_2 85° was not strongly adhered, so it did not survive the annealing process.

Annealing to 300 °C (Figure 4.15 (b)) does very little to change the total volume adsorbed; however, it does significantly reduce the size of the hysteresis loop as seen in both the QCM and EP results. SEM images before and after annealing also show minimal changes in the film morphology. The question then becomes, what happened to the hysteresis loops? In a previous study of RBD deposited TiO_2, we showed using transmission electron microscopy (TEM) that individual columns consist of a fine structure that becomes smooth following annealing[5]. Therefore, the hysteresis loops observed before annealing may arise from porosity inherent to the individual columns. Upon annealing, this porosity is lost, removing the hysteresis loop. Even though the hysteresis occurs at partial pressures which correlate to pores much larger than would be present on these columns, the contribution is still possible. All that is required is a steric or energetic hindrance to prevent toluene adsorption in these pores and to shift the adsorption to higher partial pressures. We have previously observed a significant shift in the onset of water adsorption in mesoporous TiO_2 within ~10 nm cylindrical pores due to hydrophobic effects.[36]

4.3.7.3 Biaxial Isotherms determined by EP

Changes in the refractive index of the various TiO_2 samples versus the partial pressure of toluene was monitored by measuring the first three rows of the 4x4 Mueller matrix normalized to the first element at angles of incidence of 50° and 60°. These measurements provide enough information to determine the Cauchy parameters A and B for the three principal refractive indices from 500 nm to 1000 nm in addition to the film thickness. In general, the film refractive index should increase and the anisotropy decrease as the nitrogen surrounding the columns, $n_{633\text{ nm}}= 1$, is replaced by toluene, $n_{633\text{ nm}}= 1.49$. The decrease in anisotropy can be visualized directly from the off block diagonal Mueller matrix elements which are zero for isotropic samples. For example M13, plotted for unannealed TiO_2 75° in Figure 4.16 (a) starts out greater than zero, indicating anisotropy. As the partial pressure of toluene is increased the refractive index contrast of the film decreases and M13 converges toward zero, indicating a decrease in anisotropy.

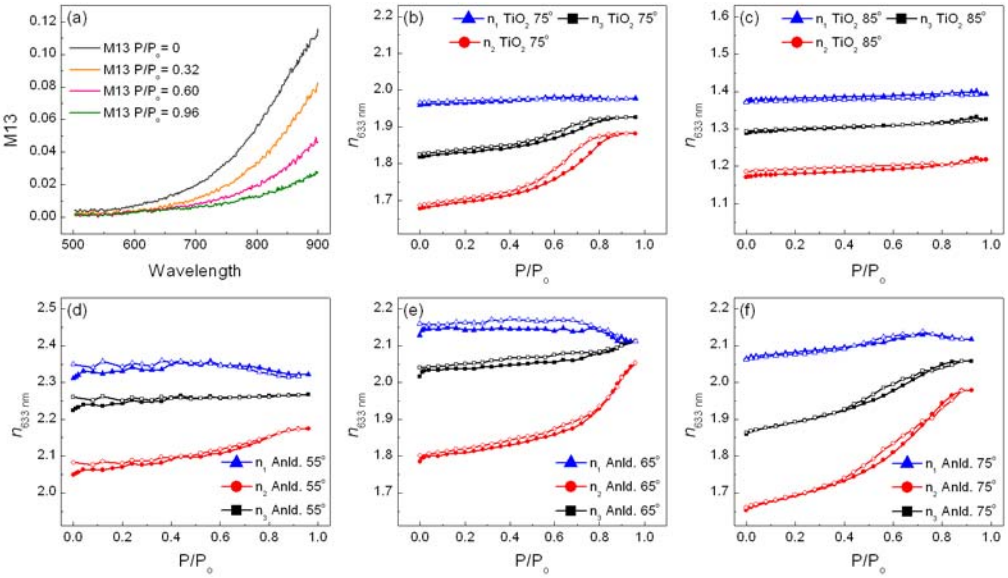

Figure 4.16 (a) Off diagonal element M13 reports on the degree of anisotropy and steadily decreases as more toluene is adsorbed (measured on TiO_2 75°). Isotherms showing *n* at 633 nm for (b) 75° and (c) 85° before annealing and (d) 55°, (e) 65°, and (f) 75° following annealing indicate good agreement with QCM data, n_2 is most sensitive to toluene adsorption.

Notice that for many of the samples (Figure 4.16), n_1 decreases at high partial pressures, converging towards n_3 and then moving with n_3 after convergence. The reason for this is related to the convergence of parameters such as M13, Figure 4.16 (a), toward zero. As the film birefringence becomes smaller, the Mueller matrix elements such as M13 approach zero and the relative 'importance' of the anisotropy is diminished, meaning that the amount of collected data can no longer support the number of fit parameters, leading to the non-physical behavior observed for n_1. Despite this issue, the shapes of the SE derived isotherms are in good agreement with QCM based isotherms shown in Figure 4.15, indicating that the extracting optical constants are correctly reporting on toluene adsorption. The EP data also confirms several features of the QCM isotherms such as the large hysteresis loop in the unannealed TiO_2 75° film (Figure 4.16 (b)), the lack of adsorption in the TiO_2 85° (Figure 4.16 (c)) film and the near disappearance of hysteresis loops in annealed samples deposited at 55, 65 and 75° degrees (Figure 4.16 (d)-(f)).

4.4 CONCLUSION

The quartz crystal microbalance/ellipsometric porosimetry technique has been demonstrated on both TiC and TiO_2 samples deposited via reactive ballistic deposition. Crystalline titanium carbide was formed at unprecedented temperature, 35 °C, as illustrated using X-ray diffraction and X-ray photoelectron spectroscopy measurements. QCM/EP measurements quantitatively show that control and variation of a single parameter, deposition angle, allows for direct tailoring of the films' optical constants, porosity, surface area, and pore size distribution. The specific surface area of the TiC samples varied from 10 $m^2 \cdot g^{-1}$ to 710 $m^2 \cdot g^{-1}$ for films deposited between 13 – 80º. Films grown with a deposition angle of 60º had an average Kelvin radius of 1.2 nm while a deposition angle of 70º resulted in an average Kelvin radius of 1.8 nm. The three principal refractive indices of biaxial TiO_2 were determined with the expected trend of $n_1 > n_3 > n_2$ and the refractive index was found to be linearly dependent on porosity. Adsorption isotherms indicate that n_2 is most sensitive to toluene adsorption and has a shape nearly identical to that determined using QCM.

4.5 REFERENCES

(1) Baklanov, M. R.; Mogilnikov, K. P.; Polovinkin, V. G.; Dultsev, F. N. *Journal of Vacuum Science & Technology B* **2000**, *18*, 1385-1391.

(2) Tompkins, H. G.; Irene, E. A.; Editors *Handbook of Ellipsometry*, 2005.

(3) Borras, A.; Sanchez-Valencia, J. R.; Garrido-Molinero, J.; Barranco, A.; Gonzalez-Elipe, A. R. *Microporous and Mesoporous Materials* **2009**, *118*, 314-324.

(4) Dohnálek, Z.; Kimmel, G. A.; Ayotte, P.; Smith, R. S.; Kay, B. D. *J. Chem. Phys.* **2003**, *118*, 364-372.

(5) Flaherty, D. W.; Dohnalek, Z.; Dohnalkova, A.; Arey, B. W.; McCready, D. E.; Ponnusamy, N.; Mullins, C. B.; Kay, B. D. *J. Phys. Chem. C* **2007**, *111*, 4765-4773.

(6) Flaherty, D. W.; Hahn, N. T.; Ferrer, D.; Engstrom, T. R.; Tanaka, P. L.; Mullins, C. B. *J. Phys. Chem. C* **2009**, *113*, 12742-12752.

(7) Barabási, A.-L.; Stanley, H. E. *Fractal Concepts in Surface Growth*; Cambridge University Press: Cambridge, Great Britain, 1995.

(8) Abelmann, L.; Lodder, C. *Thin Solid Films* **1997**, *305*, 1-21.

(9) Kim, J.; Dohnálek, Z.; Kay, B. D. *Surf. Sci.* **2005**, *586*, 137-145.

(10) Robbie, K.; Sit, J. C.; Brett, M. J. *J. Vac. Sci. Technol., B* **1998**, *16*, 1115-1122.

(11) Dohnálek, Z.; Kimmel, G. A.; McCready, D. E.; Young, J. S.; Dohnalkova, A.; Smith, R. S.; Kay, B. D. *J. Phys. Chem. B* **2002**, *106*, 3526-3529.

(12) *The Chemistry of Transition Metal Carbides and Nitrides*; Oyama, S. T., Ed.; Blackie Academic and Professional: London, 1996.

(13) Pierson, H. O. *Handbook of Refractory Carbides and Nitrides: Properties, Characteristics, Processing and Applications*; Noyes Publications: Westwood, N. J., 1996.

(14) Schmidt, D.; Booso, B.; Hofmann, T.; Schubert, E.; Sarangan, A.; Schubert, M. *Optics Letters* **2009**, *34*, 992-994.

(15) Schmidt, D.; Booso, B.; Hofmann, T.; Schubert, E.; Sarangan, A.; Schubert, M. *Applied Physics Letters* **2009**, *94*, 3.

(16) Hodgkinson, I.; Wu, Q. H.; Collett, S. *Applied optics* **2001**, *40*, 452-7.

(17) Sauerbrey, G. *Zeitschrift fur Physik* **1959**, *155*, 206-222.

(18) Shirley, D. A. *Physical Review B* **1972**, *5*, 4709-4714.

(19) Kimmel, G. A.; Dohnálek, Z.; Stevenson, K. P.; Smith, R. S.; Kay, B. D. *J. Chem. Phys.* **2001**, *114*, 5295-5303.

(20) Kimmel, G. A.; Stevenson, K. P.; Dohnálek, Z.; Smith, R. S.; Kay, B. D. *J. Chem. Phys.* **2001**, *114*, 5284-5294.

(21) Robbie, K.; Brett, M. J.; Lakhtakia, A. *Nature* **1996**, *384*, 616.

(22) Robbie, K.; Friedrich, L. J.; Dew, S. K.; Smy, T.; Brett, M. J. *J. Vac. Sci. Technol., A* **1995**, *13*, 1032-1035.

(23) Sit, J. C.; Vick, D.; Robbie, K.; Brett, M. J. *J. Mater. Res.* **1999**, *14*, 1197.

(24) Smy, T.; Vick, D.; Brett, M. J.; Dew, S. K.; Wu, A. T.; Sit, J. C.; Harris, K. D. *J. Vac. Sci. Technol. A* **2000**, *18*, 2507-2512.

(25) Liu, F.; Umlor, M. T.; Shen, L.; Weston, J.; Eads, W.; Barnard, J. A.; Mankey, G. J. *J. App. Phys.* **1999**, *85*, 5486.

(26) Colgan, M. J.; Djurfors, B.; Ivery, D. J.; Brett, M. J. *Thin Solid Films* **2004**, *466*, 92-96.

(27) Harris, K. D.; McBride, J. R.; Nietering, K. E.; Brett, M. J. *Sensor Materials* **2001**, *13*, 225.

(28) Motohiro, T.; Taga, Y. *Appl. Opt.* **1989**, *28*, 2466-2482.

(29) Messier, R.; Venugopal, V. C.; Sunal, P. D. *J. Vac. Sci. Technol., A* **2000**, *18*, 1538.

(30) Seto, M. W.; Robbie, K.; Vick, D.; Brett, M. J.; Kuhn, L. *J. Vac. Sci. Technol., B* **1999**, *17*, 2172.

(31) Stevenson, K. P.; Kimmel, G. A.; Dohnálek, Z.; Smith, R. S.; Kay, B. D. *Science* **1999**, *283*, 1505-1507.

(32) Tompkins, H. G.; McGahan, W. A. *Spectroscopic Ellipsometry and Reflectometry*; Wiley-Interscience: New York, 1999.

(33) Poxson, D. J.; Mont, F. W.; Schubert, M. F.; Kim, J. K.; Schubert, E. F. *Applied Physics Letters* **2008**, *93*, 3.

(34) Sing, K. S. W.; Everett, D. H.; Haul, R. A. W.; Moscou, L.; Pierotti, R. A.; Rouquerol, J.; Siemieniewska, T. *Pure and Applied Chemistry* **1985**, *57*, 603-619.

(35) Rouquerol, F.; Rouquerol, J.; Sing, K. *Adsorption by Powders and Porous Solids: Principles, Methodology, and Applications*; Academic Press: San Diego, 1999.

(36) May, R. A.; Patel, M. N.; Johnston, K. P.; Stevenson, K. J. *Langmuir* **2009**, *25*, 4498-4509.

(37) Patel, M. N.; Williams, R. D.; May, R. A.; Uchida, H.; Stevenson, K. J.; Johnston, K. P. *Chemistry of Materials* **2008**, *20*, 6029-6040.

(38) May, R. A.; Kondrachova, L.; Hahn, B. P.; Stevenson, K. J. *Journal of Physical Chemistry C* **2007**, *111*, 18251-18257.

(39) Simon, P.; Gogotsi, Y. *Nature Materials* **2008**, *7*, 845-854.

(40) Boissiere, C.; Grosso, D.; Lepoutre, S.; Nicole, L.; Bruneau, A. B.; Sanchez, C. *Langmuir* **2005**, *21*, 12362-12371.

(41) EerNisse, E. P. *Journal of Applied Physics* **1973**, *44*, 4482-4485.

(42) Schmidt, D.; Booso, B.; Hofmann, T.; Schubert, E.; Sarangan, A.; Schubert, M. *Applied Physics Letters* **2009**, *94*, 011914/1-011914/3.

CHAPTER 5

Future Directions in the Development of Hybrid Porosimetry

5.1 INTRODUCTION

To date we have utilized ellipsometry for the characterization of metal oxides (Chapter 2), used multiple adsorbates to characterize TiO_2 infused with metal nanoparticles (Chapter 3), and combined advanced generalized ellipsometry with the quartz crystal microbalance (QCM) to explore biaxial anisotropy in TiC and TiO_2 films deposited via reactive ballistic deposition (RBD). The future of this technique involves improvements to the existing apparatus, extension of measurement capabilities, and the development of new mesoporous systems. The most immediate and direct impact on the technique is the pending redesign of the porosimetry cell which will improve both the S/N and accuracy of QCM and EP. The next step is to improve the information density of each experiment through further integration with complementary techniques. For example, the integration of a rotating stage makes studying the azimuthal orientation dependence of anisotropic films possible. Another advanced and potentially groundbreaking addition is the integration of heat conduction calorimetry (HCC). HCC would enable the simultaneous measurement of the heat of adsorption alongside the mass and optical properties measured by QCM and SE, respectively. Apart from porosimetry the QCM should be integrated with our already existing wet ellipsometry cell. We have used this wet ellipsometry cell to study Li^+ and H^+ intercalation into WO_3, MoO_3, polyaniline and IrO_2 thin films. The QCM metal coating can be used as an electrode to monitor electrochemical processes, a technique known as electrochemical quartz crystal microbalance (EQCM). Integration of EQCM would create an excellent system for studying electrodeposition mechanisms or electrochemical dealloying.

Hand in hand with experimental improvements is the development of new materials systems. For example, we have been working on RBD deposition of columnar vanadium oxide samples. Various stoichiometries of vanadium oxide have been long studied as promising Li^+ intercalation hosts. RBD gives us fine control over the porosity and pore size and would make for an interesting study of mass transport within the material. QCM/EP could be used to characterize the mesostructure and *in situ* ellipsometry combined with EQCM experiments could be utilized to monitor the material's response to the intercalation event. Moving beyond simple columnar structures RBD can be used to construct even more advanced structures, such as layered films composed of varying column directions or arrays of cork screw shaped features. Electrochemical dealloying is another interesting film preparation technique that results in mesoporous metal surfaces with interesting catalytic properties. Separate from this, the development of simple model systems are desirable to test assumptions made both in ellipsometric porosimetry and, more generally, isotherm analysis. Highly ordered, optically transparent, isotropic samples on a QCM crystal would be an excellent system for testing these assumptions. Making these arrays has been attempted using annodization of Ti and Al. Initial results have been promising, though thus far the pore size has been larger than desired (> 50 nm).

5.2 INSTRUMENTATION IMPROVEMENTS

5.2.1 Redesign of Porosimetry Cell with 360° Stage

Currently, the cell used for porosimetry measurements consists of a hemispherical quartz window covering a small holder for mounting QCM crystals with a 0.201 cm diameter metal coating. This configuration has several disadvantages. For example, while the hemispherical quartz window allows us to take ellipsometry measurements at multiple angles of incidence it also broadens the reflected light beam. This means that total intensity at the detector is reduced (cut approximately in half), leading to S/N problems in some samples and necessitating more scan averaging. To correct this issue the redesigned cell (Figure 5.1) contains three sets of fused Si windows that are perpendicular to the incident light, minimizing signal loss. Having three sets of windows allows for measurements at angle of incidence of 45°, 60°, and 75°. We have found that greater number of angles has no advantage for achieving unique model fits to the experimental data.

Further improvements to S/N are achieved by utilizing new crystals which are 1” in diameter with a 0.5” diameter front electrode. Thanks to this larger electrode the entire probe beam will be reflected from the surface without the need to mask off the bare quartz. Masks are required with the 0.201” diameter crystals because of the risk of probing the bare quartz. The crystal will also be mounted between two o-rings, via compression at the crystal edge. Moving to this holder configuration eliminates the need to correct for liquid adsorption on the backside of the crystal, greatly increasing QCM accuracy for samples with low porosity. The freestanding nature of the current QCM configuration also makes alignment difficult and signal drift has frequently been observed due to shifting of the substrate; the more rigid mounting of the QCM eliminates both of these issues.

Complete characterization of anisotropic samples requires a sample stage that can rotate 360° (Figure 5.1) so that, in the course of a single isotherm, the full optical response of a biaxial sample can be mapped. The current configuration requires separate isotherms be taken for each orientation (we used parallel and perpendicular). The ability to simultaneously fit many different azimuthal orientations will allow full determination of n, k, thickness, and the Euler angles φ and θ. A rotatable electrical connection has been integrated into the cell, providing a simple interface to the QCM crystal without complications from wiring.

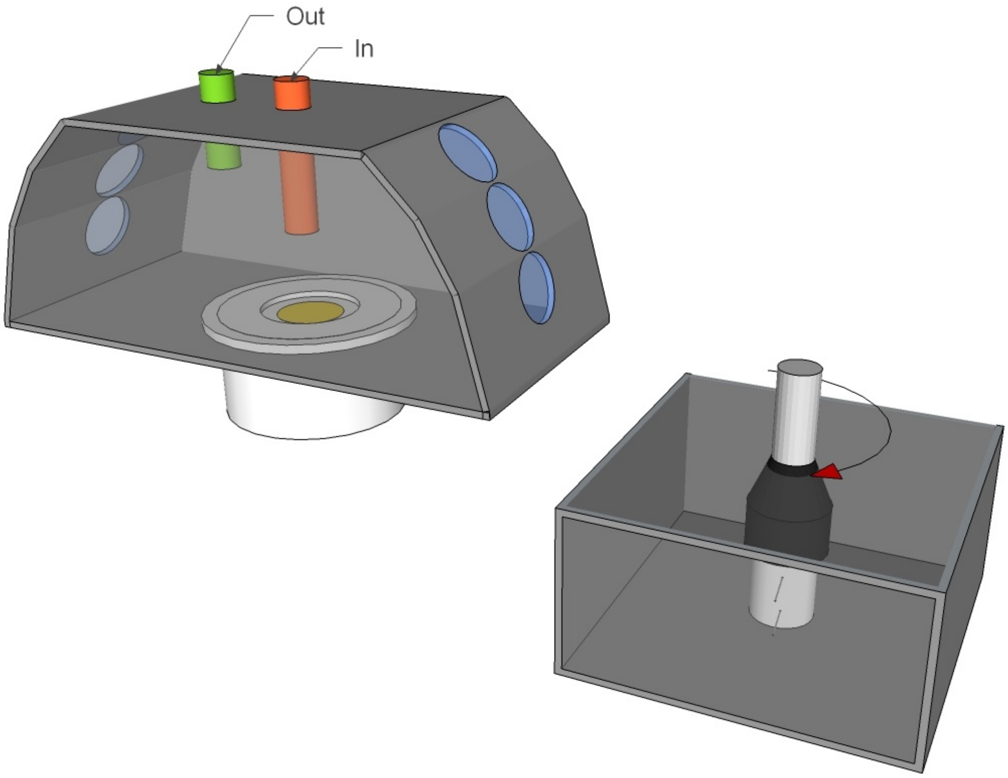

Figure 5.1. Schematic of a new design for the porosimetry cell which will improve the reproducibility of existing measurements, reduce acquisition time, and add new capabilities such as in situ sample rotation.

5.2.2 Integration of Heat Conduction Calorimetry

The integration of heat conduction calorimetry (HCC) with the quartz crystal microbalance has been demonstrated by Smith et al.[1]. A thermopile is placed between the quartz resonator and a heatsink. As heat flows from the crystal to the heatsink a voltage is generated in the thermopile which can be read into a computer. The sample deposited atop the QCM crystal is dosed with adsorbate, analogous to the QCM/EP technique. QCM/HCC has been demonstrated on several test systems, for example, to determine the heat of adsorption of H_2 on Pd at various H/Pd ratios. The most obvious obstacle to integrating HCC with the QCM/EP is maintaining thermal isolation while allowing the probe beam to come into contact with the sample. One way to achieve this would be to insulate and water jacket the entire apparatus excepting optical windows. If necessary these windows could be vacuum isolated, though outfitting the port with a thick dielectric lens would probably suffice. The addition of calorimetry to the QCM/EP would be very useful for interpreting isotherms. For example it would allow us to separate physisorption from chemisorption; especially useful for determining the nature of irreversible adsorption at low partial pressures. Moving beyond porosimetry the combination of HCC and QCM with infrared measurements would be very valuable for determining catalytic mechanisms, in particular if the exhaust gases were analyzed with mass spectrometry.

5.2.3 Addition of Wet Optical Cell with EQCM

We have used *in situ* spectroscopic ellipsometry to determine changes in *n*, *k*, and thickness for WO_3 and $Mo_{0.6}W_{0.4}O_3$ thin films during electrochemically induced Li^+ intercalations (Figure 5.2).[2] The extracted optical constants were used to explain changes in the diffraction efficiency (DE) of diffraction gratings composed of the same material during Li^+ intercalation. This cell could easily be modified to incorporate the electrochemical quartz crystal microbalance (EQCM). This technique takes a standard QCM crystal and uses the metal coated surface as the working electrode in an electrochemical experiment. In a hybrid experiment ellipsometry could be used to determine the film thickness and estimate composition (by measuring changes in *n* and *k*) while the EQCM could be used to determine the mass deposited per unit charge. The addition of ellipsometry would help to verify deposition mechanisms determined via EQCM, particularly in cases where adsorption and desorption are concurrent events. Another application of this hybrid approach is to use the QCM to determine the film stress during Li^+ intercalation (utilizing AT and BT cut quartz as discussed in Chapter 4) while measuring changes in film thickness via ellipsometry.

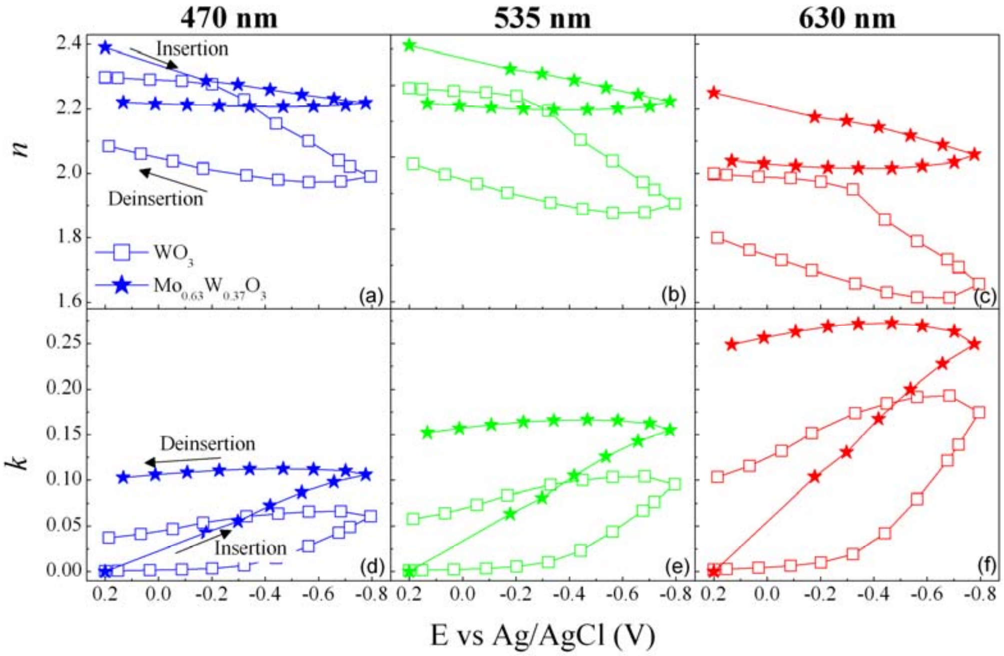

Figure 5.2. Plots of real, *n*, and imaginary, *k*, components of the refractive index as a function of applied potential during the first cycle of Li^+ insertion/deinsertion into WO_3 and $Mo_{0.6}W_{0.4}O_3$ thin films via cyclic voltammetry determined from spectroscopic ellipsometry measurements. Data in plots (a) and (d) were determined at 470 nm (blue) and in plots (b) and (e) at 535 nm (green), while data in plots (c) and (f) were determined at 630 nm (red).

5.3 NEW MATERIALS AND SYNTHESIS TECHNIQUES

5.3.1 Vanadium Oxide Deposited by RBD

RBD is a versatile technique which gives us control over both film structure (by varying the deposition angle) and composition (through variation of ambient conditions). The latest material which we have been trying to deposit is vanadium oxide. The various oxides of vanadium have long been studied as cathode materials for lithium ion batteries[4] and introducing nanostructure into the electrode improves upon the materials kinetics, durability, and capacity. As discussed previously, RBD can be used to deposit columnar structures with porosity and pore size controlled by the deposition angle. When the deposition angle is increased the size of individual columns increases which in turn increases the diffusion length, thus altering the kinetic performance of the material. The structure of these samples can be characterized using QCM/EP and the material performance studied using EQCM/ellipsometry. Additionally, more complicated coil[3] structures can be deposited by rotating the substrate during deposition. These coils are anisotropic but have different optical properties compared to columnar structures and do not have a pseudo-isotropic point (making comparisons of each structure's optical response interesting on its own). Independent of structure the oxygen stoichiometry can be varied by changing the deposition rate, partial pressure of oxygen and post deposition annealing. Thus the interplay between structure and composition can be explored.

5.3.2 Electrochemical Dealloying

Mesoporous noble metal thin films can be made through dealloying. In this process, the least noble of a metal alloy is electrochemically oxidized, dissolving into solution. The more noble metal remains, forming a mesoporous network that can be further customized by thermal annealing. EQCM/ellipsometry would be an excellent tool to confirm the dissolution mechanism and monitor additional surface modifications such as the addition of a third metal or self assembled monolayer. The catalytic properties of the material could then be explored using test reactions such as CO oxidation while the resulting structure could be characterized by QCM/EP.

5.3.3 Well Ordered Isotropic Materials

There remains much uncertainty surrounding assumptions made for both ellipsometric porosimetry and isotherm interpretation. For example, in Chapter 3, multiple adsorbates with different polarities were necessary to verify that the optical constants did not change upon adsorption in the mesopores. Unfortunately this method is time consuming and provides only indirect confirmation. In fact, this issue was the original motivation behind developing the QCM/EP technique, with the goal to identify conditions under which adsorbate properties deviate from bulk values. However, it has been difficult to fabricate a well ordered, isotropic, porous, transparent (k=0), array on the QCM crystal. The templated sol-gel TiO_2 described in Chapter 3 must be annealed at 400 °C to remove the surfactant template. At these temperatures the Au substrate layer diffuses into the film causing the film to roughen and break. One solution is to switch from a Au QCM electrode to a Pt electrode. Upon annealing Pt does not have these same issues with diffusing into the film; however, purchasing Pt coated QCM crystals is expensive so we are currently working on ways to engineer our own.

Another way to create well ordered, tailorable, arrays is annodization of Al or Ti. Annodization is carried out by placing a refractory metal in an oxide etchant. Applying a voltage to this system encourages oxide growth and the competition between oxide dissolution and formation results in a hexagonally packed array of vertically aligned pores. There are many important parameters which need to be optimized to reach the desired pore size and film thickness; these include voltage, temperature, solvent, and etchant. Films of Al and Ti were deposited using e-beam deposition to a thickness of 1-2 μm at a rate of 3-4 nm/s. This fast rate minimized oxide formation during deposition and both sets of films were found to have optical constants similar to literature values of the bulk metal. Al was anodized at 2 °C in 0.3 M oxalic acid at voltages 15 V, 20 V, 25 V, 30 V, and 40 V.[5] At 15 V oxide formation did not take place, while at 20 V oxide formed at a rate of ~ 10 nm/min increasing to ~20 nm/min at 30 V. These films were then etched in an aqueous solution of 4 wt. % CrO_3 and 10 vol. % H_3P0_4 to remove the outer oxide layer which contains narrower pores. 1 μm x 1 μm AFM images of Al anodized at 25 V, 30 V, and 40 V are presented in Figure 5.3. The pores increase in size with the increasing voltage though the diameter, 50 nm to 100 nm, was much larger than expected.

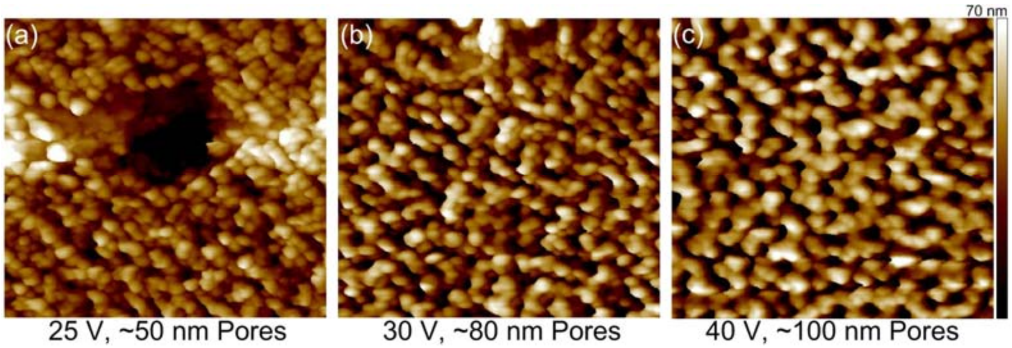

Figure 5.3 1 μm x 1 μm AFM images of ~1 μm thick Al on glass anodized in 0.3 M oxalic acid at 2 °C with voltages of (a) 25 V (b) 30 V and (c) 40 V followed by a 1 hour etch in 4 wt. % CrO_3 and 10 vol. % H_3PO_4.

Ti was anodized in ethylene glycol containing 0.38 wt. % ammonium fluoride and 1.79 wt. % water at 20 °C.[6] This etching solution resulted in more ordered films with smaller pores on Ti compared to the oxalic acid. In this procedure, films were anodized once for ~ 1 hour to build up an oxide layer. This layer was then removed with scotch tape leaving behind a Ti surface which was then anodized again. This two step annodization process obviates the need for a post anodization etch because the initial anodization templates the surface. This procedure also resulted in fairly well ordered arrays of pores, unfortunately they were still larger than desired (> 50 nm). Additionally, after several days some of the samples would flake off of the substrate. This seemed to be an effect of inadequate cooling, especially at higher voltages. Moving to 10 °C reduced this problem; future work should work on optimizing this temperature to achieve long term film stability. Initial results with anodization have been promising, though the breadth of the parameters makes optimization difficult. Instead of using thin films the process should be first optimized on Ti foil and then transitioned down to the thin film level.

5.4 CONCLUSION

Ellipsometry is a technique that can be easily hybridized with numerous techniques because it is fast, measures changes in polarization not intensity, and records multiple parameters in a single measurement. Integration with the quartz crystal microbalance has been extremely useful because it both verifies the ellipsometry data and opens up new area of analysis. Further improvements to the experimental apparatus will allow even more questions to be answered from comparison of optical data and the frequency change of the quartz crystal, i.e. how the refractive index of adsorbates changes upon adsorption in pores, or how adsorption alters the skeletal network of a porous film. The integration of electrochemistry or calorimetry would be a relatively straightforward way to gain even more information on materials systems of interest. Incorporation of electrochemistry would be especially useful for studying the dealloying process or for monitoring the Li^+ intercalation process in mesoporous vanadium oxide. Finally highly ordered model surfaces need to be perfected for the development of better adsorption models and verification of the volumes derived from the ellipsometric porosimetry technique.

5.5 REFERENCES

(1) Smith, A. L.; Shirazi, H. M. Thermochimica Acta 2005, 432, 202-211.

(2) Kondrachova, L. V.; May, R. A.; Cone, C. W.; Vanden Bout, D. A.; Stevenson, K. J. Langmuir 2009, 25, 2508-2518.

(3) Schmidt, D.; Kjerstad, A. C.; Hofmann, T.; Skomski, R.; Schubert, E.; Schubert, M. Journal of Applied Physics 2009, 105, 113508/1-113508/7.

(4) Bazito, F. F. C.; Torresi, R. M. Journal of the Brazilian Chemical Society 2006, 17, 627-642.

(5) Lazarowich, R. J.; Taborek, P.; Yoo, B. Y.; Myung, N. V. Journal of Applied Physics 2007, 101, 104909/1-104909/7.

(6) Shin, Y.; Lee, S. Nano Letters 2008, 8, 3171-3173.

Bibliography

Abelmann, L.; Lodder, C. *Thin Solid Films* **1997**, *305*, 1-21.

Abramooff, M. D.; Magelhaes, P. J.; Ram, S. J. **2004**, *11*, 36-42.

Alberius, P. C. A.; Frindell, K. L.; Hayward, R. C.; Kramer, E. J.; Stucky, G. D.; Chmelka, B. F. *Chem. Mater.* **2002**, *14*, 3284.

Allmond, C. E.; Oleshko, V. P.; Howe, J. M.; Fitz-Gerald, J. M. *Appl. Phys. A: Mater. Sci. Process.* **2006**, *82*, 675-678.

Alvarez-Herrero, A.; Ramos, G.; Del Monte, F.; Bernabeu, E.; Levy, D. *Thin Solid Films* **2004**, *455-456*, 356-360.

Auten, B. J.; Lang, H.; Chandler, B. D. *Appl. Catal., B* **2008**, *81*, 225-235.

Baeck, S. H.; Jaramillo, T.; Stucky, G. D.; McFarland, E. W. *Nano Lett.* **2002**, *2*, 831-834.

Baklanov, M. R.; Mogilnikov, K. P.; Polovinkin, V. G.; Dultsev, F. N. *J. Vac. Sci. Technol., B* **2000**, *18*, 1385-1391.

Baklanov, M. R.; Vasil'eva, L. L.; Gavrilova, T. A.; Dul'tsev, F. N.; Mogil'nikov, K. P.; Nenasheva, L. A. *Thin Solid Films* **1989**, *171*, 43-52.

Barabási, A.-L.; Stanley, H. E. *Fractal Concepts in Surface Growth*; Cambridge University Press: Cambridge, Great Britain, 1995.

Bass, J. D.; Grosso, D.; Boissiere, C.; Belamie, E.; Coradin, T.; Sanchez, C. *Chem. Mater.* **2007** *19*, 4349-4356.

Bazito, F. F. C.; Torresi, R. M. *Journal of the Brazilian Chemical Society* **2006**, *17*, 627-642.

Boissiere, C.; Grosso, D.; Lepoutre, S.; Nicole, L.; Bruneau, A. B.; Sanchez, C. *Langmuir* **2005**, *21*, 12362-12371.

Borras, A.; Sanchez-Valencia, J. R.; Garrido-Molinero, J.; Barranco, A.; Gonzalez-Elipe, A. R. *Microporous Mesoporous Mater.* **2009**, *118*, 314-324.

Borras, A.; Yanguas-Gil, A.; Barranco, A.; Cotrino, J.; Gonzalez-Elipe, A. R. *Phys. Rev. B: Condens. Matter Mater. Phys.* **2007**, *76*, 235303/1-235303/8.

Brunauer, S.; Emmett, P. H.; Teller, E. *Journal of the American Chemical Society* **1938**, *60*, 309-19.

Brust, M.; Fink, J.; Bethell, D.; Schiffrin, D. J.; Kiely, C. *J. Chem. Soc., Chem. Commun.* **1995**, 1655-6.

Brust, M.; Walker, M.; Bethell, D.; Schiffrin, D. J.; Whyman, R. *J. Chem. Soc., Chem. Commun.* **1994**, 801-2.

Castro, Y.; Julian, B.; Boissiere, C.; Viana, B.; Amenitsch, H.; Grosso, D.; Sanchez, C. *Nanotechnology* **2007**, *18*, 055705/1-055705/7.

Castro, Y.; Julian-Lopez, B.; Boissiere, C.; Viana, B.; Grosso, D.; Sanchez, C. *Microporous Mesoporous Mater.* **2007**, *103*, 273-279.
Chou, T. P.; Zhang, Q.; Russo, B.; Fryxell, G. E.; Cao, G. *J. Phys. Chem. C* **2007**, *111*, 6296-6302.

Claussen, B. H. *Journal of the Electrochemical Society* **1964**, *111*, 646-52.

Colgan, M. J.; Djurfors, B.; Ivery, D. J.; Brett, M. J. *Thin Solid Films* **2004**, *466*, 92-96.

Cortes, A.; Gomez, H.; Marotti, R. E.; Riveros, G.; Dalchiele, E. A. *Solar Energy Materials and Solar Cells* **2004**, *82*, 21-34.

Cullity, B. D. *Elements of X-Ray Diffraction. 2nd Ed*, 1978.

Deki, S.; Ko, H. Y. Y.; Fujita, T.; Akamatsu, K.; Mizuhata, M.; Kajinami, A. *Eur. Phys. J. D* **2001**, *16*, 325-328.

Desmet, D. J.; Ord, J. L. *J. Electrochem. Soc. : Electrochemical Science and Technology* **1983**, *130*, 280-284.

Dittrich, T.; Duzhko, V.; Koch, F.; Kytin, V.; Rappich, J. *Phys. Rev. B: Condens. Matter Mater. Phys.* **2002**, *65*, 155319/1-155319/5.

Dobson, M. M.; Tilley, R. J. D. *Acta Crystallographica, Section B: Structural Science* **1988**, *B44*, 474-80.

Dohnálek, Z.; Kimmel, G. A.; Ayotte, P.; Smith, R. S.; Kay, B. D. *J. Chem. Phys.* **2003**, *118*, 364-372.

Dohnálek, Z.; Kimmel, G. A.; McCready, D. E.; Young, J. S.; Dohnalkova, A.; Smith, R. S.; Kay, B. D. *J. Phys. Chem. B* **2002**, *106*, 3526-3529.

EerNisse, E. P. *Journal of Applied Physics* **1973**, *44*, 4482-4485.

Eslava, S.; Baklanov, M. R.; Kirschhock, C. E. A.; Iacopi, F.; Aldea, S.; Maex, K.; Martens, J. A. *Langmuir* **2007**, *23*, 12811-12816.

Faughnan, B. W.; Crandall, R. S. *Appl. Phys. Lett.* **1977**, *31*, 834-836.

Figlarz, M. *Progress in Solid State Chemistry* **1989**, *19*, 1-46.

Fink, J.; Kiely, C. J.; Bethell, D.; Schiffrin, D. J. *Chem. Mater.* **1998**, *10*, 922-926.

Flaherty, D. W.; Dohnalek, Z.; Dohnalkova, A.; Arey, B. W.; McCready, D. E.; Ponnusamy, N.; Mullins, C. B.; Kay, B. D. *J. Phys. Chem. C* **2007**, *111*, 4765-4773.

Flaherty, D. W.; Hahn, N. T.; Ferrer, D.; Engstrom, T. R.; Tanaka, P. L.; Mullins, C. B. *J. Phys. Chem. C* **2009**, *113*, 12742-12752.
Gesheva, K.; Szekeres, A.; Ivanova, T. *Solar Energy Materials & Solar Cells* **2003**, *76*, 563-576.

Glaves, C. L.; Frye, G. C.; Smith, D. M.; Brinker, C. J.; Datye, A.; Ricco, A. J.; Martin, S. J. *Langmuir* **1989**, *5*, 459-66.
Gondran, C. F. H.; Michelson, D. K. *J. Vac. Sci. Technol., A* **2006**, *24*, 1185-1190.

Granqvist, C. G. *Handbook of Inorganic Electrochromic Materials*; Elsevier, 1995.

Gregg, S. J.; Sing, K. S. W. *Adsorption, Surface Area and Porosity. 2nd Ed*, 1982.

Groen, J. C.; Peffer, L. A. A.; Perez-Ramirez, J. *Microporous Mesoporous Materials* **2003**, *60*, 1-17.

Gupta, G.; Patel, M. N.; Ferrer, D.; Heitsch, A. T.; Korgel, B. A.; Jose-Yacaman, M.; Johnston, K. P. *Chem. Mater.* **2008**, *20*, 5005-5015.

Gupta, G.; Shah, P. S.; Zhang, X.; Saunders, A. E.; Korgel, B. A.; Johnston, K. P. *Chemistry of Materials* **2005**, *17*, 6728-6738.

Harris, K. D.; McBride, J. R.; Nietering, K. E.; Brett, M. J. *Sensor Materials* **2001**, *13*, 225.

Haynes, J. M. *Materials and Structures* **1973**, *6*, 209-213.

He, T.; Yao, J. *Progress in Materials Science* **2006**, *51*, 810-879.

Henderson, M. A. *Langmuir* **1996**, *12*, 5093-5098.

Heuberger, M.; Zach, M.; Spencer, N. D. *Science* **2001**, *292*, 905-908.

Hodgkinson, I.; Wu, Q. H.; Collett, S. *Applied optics* **2001**, *40*, 452-7.

Hoffmann, M. R.; Martin, S. T.; Choi, W.; Bahnemann, D. W. *Chem. Rev.* **1995**, *95*, 69.

Itoh, M.; Hayakawa, K.; Oishi, S. *Journal of Physics: Condensed Matter* **2001**, *13*, 6853-6864.

Jellison, G. E.; Modine, F. A. *Appl. Phys. Lett.* **1996**, *69*, 371-373.

Jousseaume, V.; Rolland, G.; Babonneau, D.; Simon, J. P. *Appl. Surf. Sci.* **2007**, *254*, 473-479.

Julien, C. M. *Materials Science & Engineering, R: Reports* **2003**, *R40*, 47-102.

Kakiuchida, H.; Shimodaira, N.; Sekiya, E. H.; Saito, K.; Ikushima, A. J. *Appl. Phys. Lett.* **2005**, *86*, 1-3.

Kavan, L.; Prochazka, J.; Spitler, T. M.; Kalbac, M.; Zukalova, M.; Drezen, T.; Gratzel, M. *J. Electrochem. Soc.* **2003**, *150*, A1000-A1007.

Kekicheff, P.; Spalla, O. *Langmuir* **1994**, *10*, 1584-91.

Khawaja, E. E.; Durrani, S. M. A.; Daous, M. A. *J. Phys.: Condens. Matter* **1997**, *9*, 9381-9392.

Kim, J.; Dohnálek, Z.; Kay, B. D. *Surf. Sci.* **2005**, *586*, 137-145.

Kim, S.-S.; Choi, S.-Y.; Park, C.-G.; Jin, H.-W. *Thin Solid Films* **1999**, *347*, 155-160.

Kimizuka, N.; Akahane, T.; Matsumoto, S.; Yukino, K. *Inorganic Chemistry* **1976**, *15*, 3178-9.

Kimmel, G. A.; Dohnálek, Z.; Stevenson, K. P.; Smith, R. S.; Kay, B. D. *J. Chem. Phys.* **2001**, *114*, 5295-5303.

Kimmel, G. A.; Stevenson, K. P.; Dohnálek, Z.; Smith, R. S.; Kay, B. D. *J. Chem. Phys.* **2001**, *114*, 5284-5294.

Klotz, M.; Rouessac, V.; Rebiscoul, D.; Ayral, A.; van der Lee, A. *Thin Solid Films* **2005**, *495*, 214-218.
Klug, H. P.; Alexander, L. E. *X-Ray Diffraction Procedures for Polycrystalline and Amorphous Materials. 2nd ed*, 1974.

Kondrachova, L.; Hahn, B. P.; Vijayaraghavan, G.; Williams, R. D.; Stevenson, K. J. *Langmuir* **2006**, *22*, 10490-10498.

Kondrachova, L. V.; May, R. A.; Cone, C. W.; Vanden Bout, D. A.; Stevenson, K. J. *Langmuir* **2009**, *25*, 2508-2518.

Kruk, M.; Jaroniec, M.; Sayari, A. *Langmuir* **1997**, *13*, 6267-6273.

Lazarowich, R. J.; Taborek, P.; Yoo, B. Y.; Myung, N. V. *Journal of Applied Physics* **2007**, *101*, 104909/1-104909/7.

Lee, H.-J.; Soles, C. L.; Kang, S.; Ro, H. W.; Lin, E. K.; Wu, W.-l. *AIP Conf. Proc.* **2007**, *931*, 209-215.

Li, S.; Germanenko, I. N.; El-Shall, M. S. *Journal of Cluster Science* **1999**, *10*, 533-547.

CRC Handbook of Chemistry and Physics; 88 ed.; Lide, D. R., Ed., 2008.

Liu, F.; Umlor, M. T.; Shen, L.; Weston, J.; Eads, W.; Barnard, J. A.; Mankey, G. J. *J. App. Phys.* **1999**, *85*, 5486.

Liu, K.; Zhang, M.; Zhou, W.; Li, L.; Wang, J.; Fu, H. *Nanotechnology* **2005**, *16*, 3006-3011.

Long, C. G.; Gilbertson, J. D.; Vijayaraghavan, G.; Stevenson, K. J.; Pursell, C. J.; Chandler, B. D. *J. Am. Chem. Soc.* **2008**, *130*, 10103-10115.

Losurdo, M.; Barreca, D.; Bruno, G.; Tondello, E. *Thin Solid Films* **2001**, *384*, 58-64.

Losurdo, M.; Barreca, D.; Capezzuto, P.; Bruno, G.; Tondello, E. *Surface and Coatings Technology* **2002**, *151-152*, 2-8.

Losurdo, M.; Bruno, G. *Applied Physics Letters* **2000**, *77*, 1129-1131.

May, R. A.; Kondrachova, L.; Hahn, B. P.; Stevenson, K. J. *Journal of Physical Chemistry C* **2007**, *111*, 18251-18257.

May, R. A.; Patel, M. N.; Johnston, K. P.; Stevenson, K. J. *Langmuir* **2009**, *25*, 4498-4509.

McEvoy, T. M.; Stevenson, K. J. *Langmuir* **2005**, *21*, 3521-3528.

McEvoy, T. M.; Stevenson, K. J. *Langmuir* **2005**, *21*, 3529-3538.

McEvoy, T. M.; Stevenson, K. J.; Hupp, J. T.; Dang, X. *Langmuir* **2003**, *19*, 4316-4326.

Mergel, D. *397* **2001**, 216.

Messier, R.; Venugopal, V. C.; Sunal, P. D. *J. Vac. Sci. Technol., A* **2000**, *18*, 1538.

Monk, P. M. S.; Ali, T.; Partridge, R. D. *Solid State Ionics* **1995**, *80*, 75-85.

Monk, P. M. S.; Bleazard, S.; Akhtar, S. P.; Boutevin, J. *Phys. Chem. Chem. Phys.* **2000**, *2*, 4415-4419.

Mor, G. K.; Varghese, O. K.; Paulose, M.; Shankar, K.; Grimes, C. A. *Sol. Energy Mater. Sol. Cells* **2006**, *90*, 2011-2075.

Motohiro, T.; Taga, Y. *Appl. Opt.* **1989**, *28*, 2466-2482.

Mukherjee, N.; Paulose, M.; Varghese, O. K.; Mor, G. K.; Grimes, C. A. *Journal of Materials Research* **2003**, *18*, 2296-2299.

Ogura, S.; MacLeod, H. A. *Thin Solid Films* **1976**, *34*, 371-5.

Okumura, M.; Nakamura, S.; Tsubota, S.; Nakamura, T.; Azuma, M.; Haruta, M. *Catal. Lett.* **1998**, *51*, 53-58.

The Chemistry of Transition Metal Carbides and Nitrides; Oyama, S. T., Ed.; Blackie Academic and Professional: London, 1996.

Pankove, J. I. *Optical Processing in Semiconductors*; Dover Publications, 1971.

Patel, M. N.; Williams, R. D.; May, R. A.; Uchida, H.; Stevenson, K. J.; Johnston, K. P. *Chem. Mater.* **2008**, *20*, 6029-6040.

Perez, G. P.; Yelton, W. G.; Cernosek, R. W.; Simonson, R. J.; Crooks, R. M. *Anal. Chem.* **2003**, *75*, 3625-3630.

Pierson, H. O. *Handbook of Refractory Carbides and Nitrides: Properties, Characteristics, Processing and Applications*; Noyes Publications: Westwood, N. J., 1996.

Poxson, D. J.; Mont, F. W.; Schubert, M. F.; Kim, J. K.; Schubert, E. F. *Applied Physics Letters* **2008**, *93*, 3.

Ravikovitch, P. I.; Vishnyakov, A.; Neimark, A. V.; Carrott, M. M. L. R.; Russo, P. A.; Carrott, P. J. *Langmuir* **2006**, *22*, 513-516.

Revol, P.; Perret, D.; Bertin, F.; Fusalba, F.; Rouessac, V.; Chabli, A.; Passemard, G.; Ayral, A. *J. Porous Mater.* **2005**, *12*, 113-121.

Rioux, R. M.; Song, H.; Hoefelmeyer, J. D.; Yang, P.; Somorjai, G. A. *J. Phys. Chem. B* **2005**, *109*, 2192-2202.

Robbie, K.; Brett, M. J.; Lakhtakia, A. *Nature* **1996**, *384*, 616.

Robbie, K.; Friedrich, L. J.; Dew, S. K.; Smy, T.; Brett, M. J. *J. Vac. Sci. Technol., A* **1995**, *13*, 1032-1035.

Robbie, K.; Sit, J. C.; Brett, M. J. *J. Vac. Sci. Technol., B* **1998**, *16*, 1115-1122.

Roth, R. S.; Waring, J. L. *J. Res. Natl. Bur. Std., A* **1966**, *70*, 281-803.

Rouquerol, F.; Rouquerol, J.; Sing, K. *Adsorption by Powders and Porous Solids: Principles, Methodology, and Applications*; Academic Press: San Diego, 1999.

Salje, E.; Gehlig, R.; Viswanathan, K. *Journal of Solid State Chemistry* **1978**, *25*, 239-50.

Sanchez, C.; Boissiere, C.; Grosso, D.; Laberty, C.; Nicole, L. *Chemistry of Materials* **2008**, *20*, 682-737.

Sasaki, T.; Koshizaki, N.; Yoon, J.-W.; Yamada, S.; Koinuma, M.; Noguchi, M.; Matsumoto, Y. *Electrochemistry (Tokyo, Jpn.)* **2004**, *72*, 443-445.

Sauerbrey, G. *Zeitschrift fuer Physik* **1959**, *155*, 206-22.

Sauerbrey, G. *Zeitschrift fur Physik* **1959**, *155*, 206-222.

Schmidt, D.; Booso, B.; Hofmann, T.; Schubert, E.; Sarangan, A.; Schubert, M. *Optics Letters* **2009**, *34*, 992-994.

Schmidt, D.; Booso, B.; Hofmann, T.; Schubert, E.; Sarangan, A.; Schubert, M. *Applied Physics Letters* **2009**, *94*, 3.

Schmidt, D.; Kjerstad, A. C.; Hofmann, T.; Skomski, R.; Schubert, E.; Schubert, M. *Journal of Applied Physics* **2009**, *105*, 113508/1-113508/7.

Schubert, M. *Annalen der Physik (Weinheim, Germany)* **2006**, *15*, 480-497.
Seto, M. W.; Robbie, K.; Vick, D.; Brett, M. J.; Kuhn, L. *J. Vac. Sci. Technol., B* **1999**, *17*, 2172.

Shin, Y.; Lee, S. *Nano Letters* **2008**, *8*, 3171-3173.

Shirley, D. A. *Physical Review B* **1972**, *5*, 4709-4714.

Simon, P.; Gogotsi, Y. *Nature Materials* **2008**, *7*, 845-854.

Sing, K. S. W.; Everett, D. H.; Haul, R. A. W.; Moscou, L.; Pierotti, R. A.; Rouquerol, J.; Siemieniewska, T. *Pure and Applied Chemistry* **1985**, *57*, 603-19.

Sing, K. S. W.; Everett, D. H.; Haul, R. A. W.; Moscou, L.; Pierotti, R. A.; Rouquerol, J.; Siemieniewska, T. *Pure and Applied Chemistry* **1985**, *57*, 603-619.

Sit, J. C.; Vick, D.; Robbie, K.; Brett, M. J. *J. Mater. Res.* **1999**, *14*, 1197.

Smarsly, B.; Grosso, D.; Brezesinski, T.; Pinna, N.; Boissiere, C.; Antonietti, M.; Sanchez, C. *Chem. Mater.* **2004**, *16*.

Smith, A. L. *Polymer Preprints (American Chemical Society, Division of Polymer Chemistry)* **2004**, *45*, 199-200.

Smith, A. L.; Mulligan, R. B.; Shirazi, H. M. *Journal of Polymer Science, Part B: Polymer Physics* **2004**, *42*, 3893-3906.

Smith, A. L.; Shirazi, H. M. *Thermochimica Acta* **2005**, *432*, 202-211.

Smith, A. L.; Shirazi, H. M.; Smith, F. C. *Catalysis Letters* **2005**, *104*, 199-204.

Smy, T.; Vick, D.; Brett, M. J.; Dew, S. K.; Wu, A. T.; Sit, J. C.; Harris, K. D. *J. Vac. Sci. Technol. A* **2000**, *18*, 2507-2512.

Stefanovich, E. V.; Truong, T. N. *Chem. Phys. Lett.* **1999**, *299*, 623-629.

Stevenson, K. P.; Kimmel, G. A.; Dohnálek, Z.; Smith, R. S.; Kay, B. D. *Science* **1999**, *283*, 1505-1507.

Synowicki, R. A. *Thin Solid Films* **1998**, *313-314*, 394-397.

Tauc, J. In *Amorphous and Liquid Semiconductors*; Tauc, J., Ed.; Plenum Press: 1974, p 159-220.

Taurino, A.; Catalano, M.; Rella, R.; Sicilliano, P.; Wlodarski, W. *Journal of Applied Physics* **2003**, *93*, 3816-3822.

Tazawa, M.; Jin, P.; Tanemura, S. *Applied Optics* **1998**, *37*, 1858-1861.

Thimsen, E.; Rastgar, N.; Biswas, P. *Journal of Physical Chemistry C* **2008**, *112*, 4134-4140.

Thomas, J. M.; Hernandez-Garrido, J. C.; Raja, R.; Bell, R. G. *Physical Chemistry Chemical Physics* **2009**, *11*, 2799-2825.

Tompkins, H. G.; Irene, E. A.; Editors *Handbook of Ellipsometry*, 2005.
Tompkins, H. G.; McGahan, W. A. *Spectroscopic Ellipsometry and Reflectometry*; Wiley-Interscience, 1999.

Vogt, B. D.; Pai, R. A.; Lee, H.-J.; Hedden, R. C.; Soles, C. L.; Wu, W.-L.; Lin, E. K.; Bauer, B. J.; Watkins, J. J. *Chem. Mater.* **2005**, *17*, 1398-1408.

Vomiero, A.; Della Mea, G.; Ferroni, M.; Martinelli, G.; Roncarati, G.; Guidi, V.; Comini, E.; Sberveglieri, G. *Materials Science & Engineering, B: Solid-State Materials for Advanced Technology* **2003**, *B101*, 216-221.

Wang, N.; Lin, H.; Li, J.; Tang, X.; Chi, B. *Thin Solid Films* **2006**, *496*.

Wang, Y.; Takahashi, K.; Lee, K.; Cao, G. *Advanced Functional Materials* **2006**, *16*, 1133-1144.

Wikander, K.; Petit, C.; Holmberg, K.; Pileni, M.-P. *Langmuir* **2006**, *22*, 4863-4868.

Wongmanerod, C.; Zangooie, S.; Arwin, H. *Appl. Surf. Sci.* **2001**, *172*, 117-125.

Woodward, P. M.; Sleight, A. W.; Vogt, T. *Journal of Physics and Chemistry of Solids* **1995**, *56*, 1305-15.

Wooten, F. *Optical Properties of Solids*; Academic Press, 1972.

Wu, C. W.; Ohsuna, T.; Kuwabara, M.; Kuroda, K. *J. Am. Chem. Soc.* **2006**, *128*.

Yoffe, A. D. *Advances in Physics* **1993**, *42*, 173-266.

Yu, J. C.; Wang, X.; Fu, X. *Chem. Mater.* **2004**, *16*.

Yu, J. C.; Zhang, L.; Yu, J. *Chem. Mater.* **2002**, *14*, 4647.

Yu, J. C.; Zhang, L.; Yu, J. *Chem. Mater.* **2003**, *15*, 2280.

Zangooie, S.; Bjorklund, R.; Arwin, H. *J. Electrochem. Soc.* **1997**, *144*, 4027-4035.

Zhang, Q.; Xu, T.; Butterfield, D.; Misner, M. J.; Ryu, D. Y.; Emrick, T.; Russell, T. P. *Nano Lett.* **2005**, *5*, 357-361.

Zhao, G.; Kozuka, H.; Yoko, T. *Sol. Energy Mater. Sol. Cells* **1997**, *46*, 219-231.

Vita

Robert Alan May, the son of Franklin Thomas May and Fay Ann Miller, was born in Houston Texas on February 15, 1982. He graduated from Reicher Catholic High School in Waco, TX in May 2000 and completed a Bachelor of Arts in Chemistry and a Bachelor of Arts in Economics at Trinity University in San Antonio, TX in May 2004. In September 2005 Alan entered the University of Texas at Austin to pursue his Doctorate in Analytical Chemistry under the guidance of Prof. Keith J. Stevenson.

Permanent address: 616 Fitzpatrick Waco, TX 78741
This dissertation was typed by the author